

For Reference

NOT TO BE TAKEN FROM THIS ROOM

For Reference

NOT TO BE TAKEN FROM THIS ROOM

Ex LIBRIS
UNIVERSITATIS
ALBERTAENSIS





Digitized by the Internet Archive
in 2019 with funding from
University of Alberta Libraries

<https://archive.org/details/Gurd1966>

The
196
#3

THE UNIVERSITY OF ALBERTA

CALIBRATION OF A BROAD RANGE MAGNETIC
SPECTROGRAPH-SPECTROMETER

by

David Preston Gurd

A THESIS

SUBMITTED TO THE FACULTY OF GRADUATE STUDIES
IN PARTIAL FULFILMENT OF THE REQUIREMENTS FOR THE DEGREE
OF MASTER OF SCIENCE

DEPARTMENT OF PHYSICS
EDMONTON, ALBERTA

April, 1966

UNIVERSITY OF ALBERTA
FACULTY OF GRADUATE STUDIES

The undersigned certify that they have read, and recommend to the Faculty of Graduate Studies for acceptance, a thesis entitled CALIBRATION OF A BROAD RANGE MAGNETIC SPECTROGRAPH-SPECTROMETER, submitted by David Preston Gurd in partial fulfilment of the requirements for the degree of Master of Science.

INTRODUCTION

The University of Alberta 50 cm. spectrograph-spectrometer of the Browne-Buechner-Enge type has been calibrated over the effective proton energy range 2.5 - 10 MeV, and certain of its characteristics measured.

The experiments described in this thesis were done over a period of about 4 months only, and by no means do they reflect the total amount of time which has gone into the preparation of the spectromagnet for use. Before the author became involved in the project, the nuclear magnetic resonance system described in Chapter 3 had been designed and built by Dr. W. C. Olsen, and used to make the first field homogeneity tests on the spectromagnet. The target chamber and the detector holder were also already in existence. The work which remained to be done before these experiments could be carried out included redesigning the rotating base to allow the spectrometer to be mounted in the horizontal position, designing the adjustable pads on which the magnet rests; modifying the design of the detector holder to accommodate the solid state detectors used, planning the power supply auxiliary interlock which protects both the spectromagnet and the Mobley bunching magnet from water failures, aligning the system optically, and, finally, a great deal of plumbing associated with both the water cooling and the vacuum systems.

The thesis is divided into two parts. The first-order theory of the spectrograph-spectrometer is developed in Part I, first from a straightforward

geometric argument (Chapter 1) and then making use of the matrix formalism (Chapter 2), the two approaches being compared at each step. The second part describes the calibration experiments, first on the spectrograph alone (Chapter 4), and then on the combined spectromagnet and quadrupole, or spectrometer (Chapter 5). The apparatus used is described briefly in Chapter 3, and some of the difficulties encountered in a series of four Appendices.

ACKNOWLEDGMENTS

I wish to thank my supervisors; Dr. W. K. Dawson, for having suggested the project; Dr. W. C. Olsen, whose many contributions are only hinted at in the text of this thesis; and Dr. G. Roy, whose invaluable suggestions, unflagging optimism, and countless hours of work made the completion of this project possible. Dr. G. C. Neilson has also contributed many useful ideas and discussions.

I wish to thank Mr. Con Green and Mr. Dick Gordon for tirelessly producing first-class machining from third-class drawings; Mr. Lars Holm for making my electronic embarrassment less conspicuous; and Mr. J. B. Elliott who, with unfailing good humour and interest, has rescued me from one quandary after another.

I wish to thank Mr. Tom Grandy for the use of his kinematics program; Mr. Henry Leighton for the many hours he has contributed; and Mr. Andrew Obst, both for the several computer programs he has written and the many early morning hours during which his help was invaluable.

I am most grateful to Miss Greta Tratt, who has somehow contrived to translate an illegible scrawl into these typewritten pages.

The financial assistance, both of the National Research Council and the University of Alberta, is gratefully acknowledged.

Finally, I am indebted to my wife for her patience and encouragement.

TABLE OF CONTENTS

PART I: Theory

Chapter 1: Geometrical Formulation

| | |
|-------------------------------------------|---|
| (a) Barber's Rule | 2 |
| (b) Circular Magnetic Field | 3 |
| (c) The Focal Plane | 5 |
| (d) Magnification, Dispersion, Resolution | 6 |
| (e) Projections on the Focal Plane | 7 |

Chapter 2: Matrix Formulation

| | |
|------------------------------------|----|
| 1. General Theory | |
| (a) Matrix Equations | 10 |
| (b) Meaning of the Matrix Elements | 12 |
| (c) Lenses | 15 |
| 2. The Spectrograph | |
| (a) Derivation of the Matrix | 17 |
| (b) The Matrix Elements | 22 |
| (c) Kinematic Broadening | 25 |
| 3. The Spectrometer | |
| (a) Derivation of the Matrix | 27 |
| (b) The Matrix Elements | 33 |
| (c) Thin Lens Approximation | 35 |
| (d) Solid Angle | 38 |

PART II: Experimental

Chapter 3: Apparatus

| | |
|---------------------------------|----|
| (a) The Spectromagnet and Base | 42 |
| (b) The Quadrupole Lens | 43 |
| (c) Field Measurement | 44 |
| (d) The Target Chamber | 45 |
| (e) Targets | 46 |
| (f) The Detector and Step Wedge | 47 |

Chapter 4: The Spectrograph

| | |
|------------------------------------|----|
| (a) Location of the Focal Plane | 49 |
| (b) Determining the Reaction Angle | 53 |
| (c) The Calibration Curve | 57 |
| (d) The Dispersion Curve | 62 |
| (e) Solid Angle | 65 |

Chapter 5: The Spectrometer

| | |
|-------------------------------------------|----|
| (a) Preliminaries | 66 |
| (b) Location of the Focal Plane | 67 |
| (c) The Calibration Curve | 69 |
| (d) Dispersion, Magnification, Resolution | 70 |
| (e) Solid Angle | 74 |

| | |
|-------------------------------------------|----|
| Appendix A: The Quadrupole Lens | 78 |
|-------------------------------------------|----|

| | |
|------------------------------------------|----|
| Appendix B: The Target Chamber | 85 |
|------------------------------------------|----|

| | |
|----------------------|----|
| Appendix C | 88 |
|----------------------|----|

| | |
|----------------------|----|
| Appendix D | 91 |
|----------------------|----|

PART I: THEORY

CHAPTER 1: GEOMETRICAL FORMULATION

(a) Barber's Rule

The geometrical formulation is based entirely upon Barber's Rule for focusing (Barber, 1933) which states that particles which enter and leave a region of uniform magnetic field normally are focused on a straight line which includes the source (S') and the center of curvature of the path of the particles in the field (O). (See figure 1-2.)

The proof of the rule follows from figures 1 and 2. The arc SCI in figure 1 represents the central ray in a 180 degree focusing magnet, while SDI is a non-central ray with a small departure angle α from the source, S. From the geometry of the figure:

$$\begin{aligned}OP &= \rho\alpha \\OQ &= \rho\beta = \rho\alpha \cos \theta = \rho\alpha \cos(s/\rho) \\ \text{i.e. } \beta &= \alpha \cos(s/\rho)\end{aligned}$$

where s is the distance along the central ray and ρ is the radius of curvature of both rays.

To first order, β is the angle between the normals to the two rays, and hence is equal to the angle between the tangents to the two rays. Thus, if x is the perpendicular distance between the two rays at a distance s along the central ray, we have:

$$dx/ds = \beta = \alpha \cos(s/\rho) \tag{1-1}$$

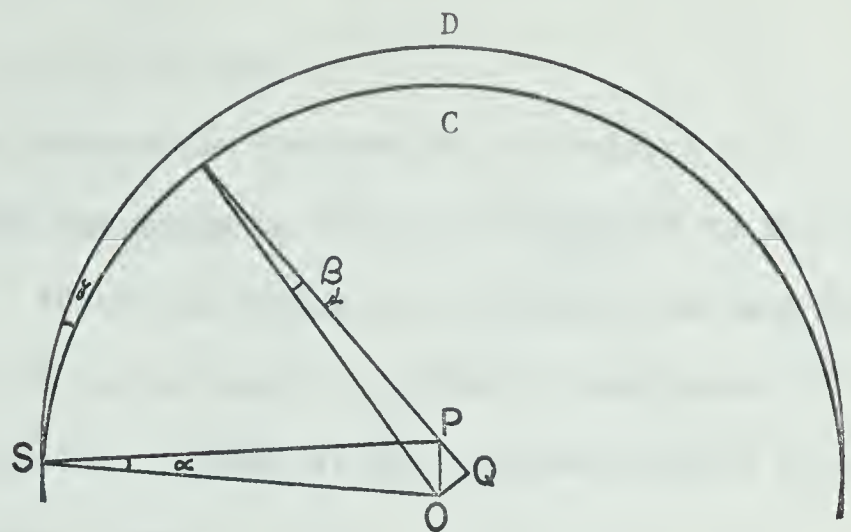


FIGURE 1-1

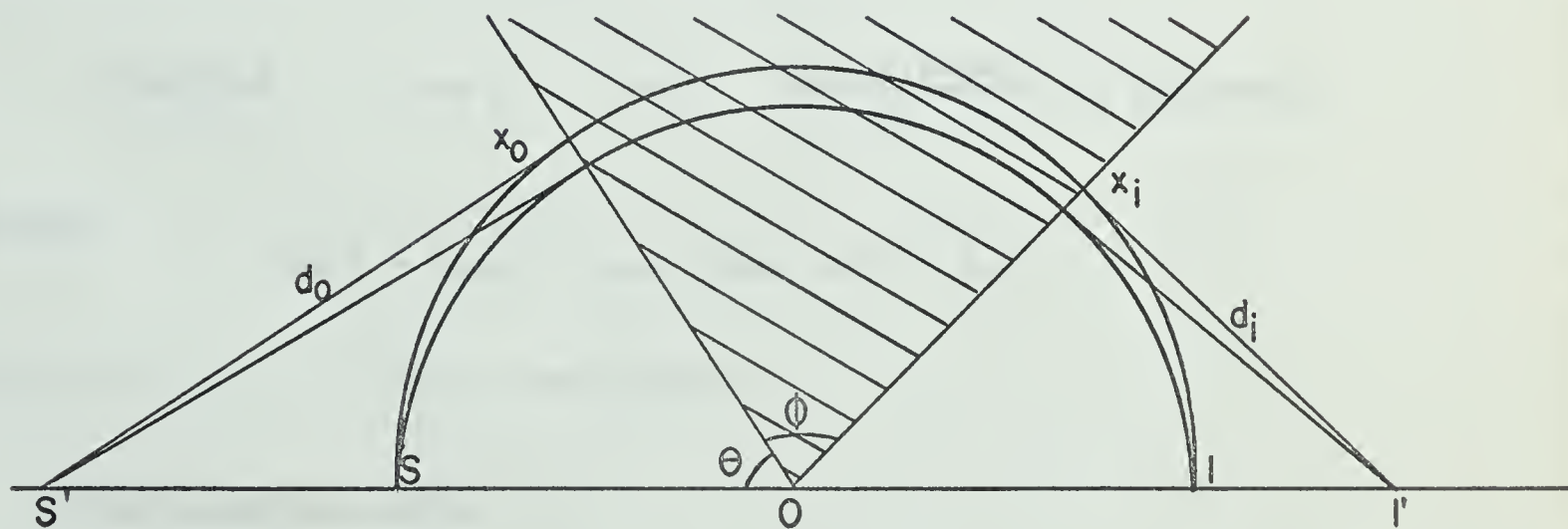


FIGURE 1-2

BARBER'S RULE

Integrating (1-1) gives

$$x = \rho \alpha \sin(s/\rho) \quad (1-2)$$

where the constant of integration vanishes as $x = 0$ for $s = 0$.

We now assume that the magnetic field is restricted to the shaded area ϕ in figure 1-2. If the particles are to follow the same paths in the field as before, the source must be removed to some point S' and the image to some other point I' located at the intersections of the tangents to the rays at the sector faces.

If d_0 is the distance from the first sector face to S' , and d_1 is the distance from the second face to I' , then

$$\frac{x_0}{d_0} = \left. \frac{dx}{ds} \right|_{\theta} \quad \text{and} \quad \frac{x_1}{d_1} = \left. \frac{dx}{ds} \right|_{\pi-\theta-\phi}$$

Substituting from equation (1-1) and (1-2) gives

$$\frac{\rho \alpha \sin \theta}{d_0} = \alpha \cos \theta \quad \text{and} \quad \frac{\rho \alpha \sin(\pi-\theta-\phi)}{d_1} = \alpha \cos(\pi-\theta-\phi)$$

Therefore

$$\tan \theta = d_0/\rho \quad \text{and} \quad \tan (\theta+\phi) = d_1/\rho$$

That is, S' , S , O , I , and I' are colinear.

(b) Circular Magnetic Field

Consider next a ray which enters normally a circular magnetic field of radius R and follows an arc of radius r through an angle α before leaving the field. The situation is illustrated in figure 3. Three facts

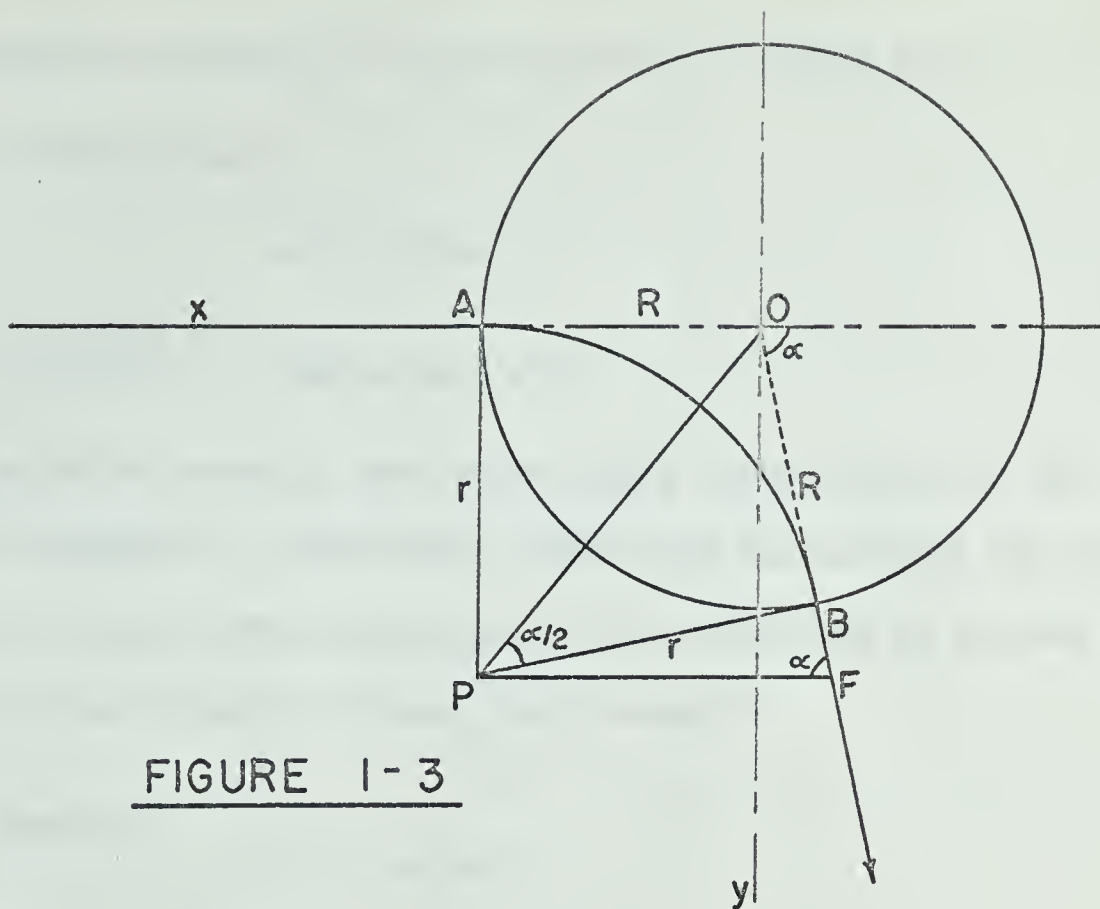


FIGURE 1-3

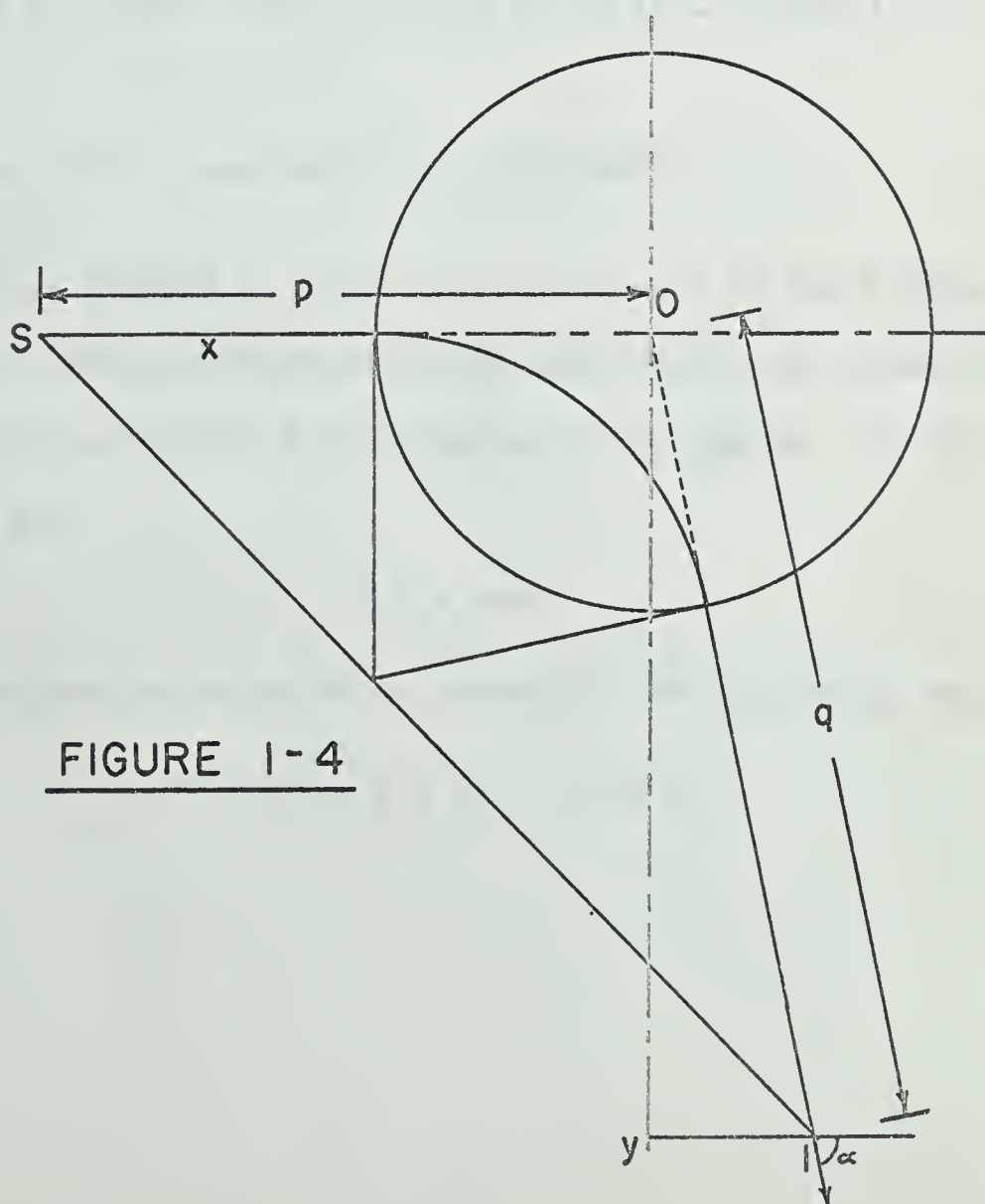


FIGURE 1-4

may be ascertained directly from the geometry of figure (1-3).

(i) Firstly, since

$$\triangle AOP \equiv \triangle POB$$

therefore

$$OBP = OAP = 90^\circ$$

Thus the ray exits normally, and we may apply Barber's Rule in our geometrical arguments. Furthermore, since both the incident and the deflected rays pass through the point O, the system may be treated as a thin lens whose principle planes pass through O.

(ii) Secondly,

$$r = R \cot \alpha/2 \quad (1-3)$$

Thus we have

$$\cos \alpha = (\cot^2 \alpha/2 - 1)/(\cot^2 \alpha/2 + 1) = (r^2 - R^2)/(r^2 + R^2) \quad (1-4)$$

$$\text{and} \quad \sin \alpha = (1 - \cos^2 \alpha)^{1/2} = 2rR/(r^2 + R^2) \quad (1-5)$$

(iii) Thirdly, suppose a source is located at ∞ on the x axis.

By Barber's Rule, particles emitted at the source will be focused at F, which, by definition, must be a focal point of the system. In the triangle BPF we see

$$BF = OF - R = r \cot \alpha$$

By using (1-3) we can solve for OF in terms of r or R, getting respectively

$$OF = r/\sin \alpha = R/(1 - \cos \alpha)$$

Since the principal plane of the system passes through O, the distance OF is the focal length, f , of the system, and we have

$$f = r/\sin \alpha = R/(1 - \cos \alpha) \quad (1-6)$$

(c) The Focal Plane

The equation of the focal plane now can be determined by the application of the well-known focusing condition for a thin lens, namely

$$\frac{1}{p} + \frac{1}{q} = \frac{1}{f} = \frac{(1 - \cos \alpha)}{R} \quad (1-7)$$

where p and q are the object and image distances respectively. (See figure 1-4.)

Solving for q gives

$$q = Re/(1 - e \cos \alpha) \quad (1-8)$$

where $e = p/(p - R)$.

From figure 1-4 we see that the position of the focus is defined by the coordinates

$$\begin{aligned} x &= -q \cos \alpha \\ y &= q \sin \alpha \end{aligned} \quad (1-9)$$

Equations (1-8) and (1-9) may now be used to eliminate α and q from equation (1-7), the result being

$$\left\{x - \frac{e^2}{e^2 - 1} R\right\}^2 - y^2/(e^2 - 1) = R^2 e^2/(e^2 - 1)^2 \quad (1-10)$$

Thus the focal plane is a conic section which, for $e > 1$ is a hyperbola.

It is also useful to have an expression for the slope of the focal plane, dy/dx , in terms of α . We first observe from equation (1-7) that

$$\frac{dq}{d\alpha} = \frac{-Re^2 \sin \alpha}{(1 - e \cos \alpha)^2} \quad (1-11)$$

Then, combining equations (1-8), (1-9), and (1-11) we have

$$\frac{dx}{d\alpha} = -\frac{dq}{d\alpha} \cos \alpha + q \sin \alpha = \frac{Re \sin \alpha}{(1 - e \cos \alpha)^2}$$

and, similarly

$$\frac{dy}{d\alpha} = \frac{dq}{d\alpha} \sin \alpha + q \cos \alpha = \frac{-Re(e - \cos \alpha)}{(1 - e \cos \alpha)^2}$$

Hence the slope of the focal plane is

$$\frac{dy}{dx} = \frac{-(e - \cos \alpha)}{\sin \alpha} \quad (1-12)$$

(d) Magnification, Dispersion, Resolution

Continuing the argument from elementary geometrical optics, if the object (or source) is of finite size, the magnification at the image is given by

$$M = -q/p = -Re/p(1 - e \cos \alpha) = (1 - e)/(1 - e \cos \alpha) \quad (1-13)$$

The axial magnification is found by differentiating (1-7) with respect to p . This gives

$$\text{Max} = \frac{dq}{dp} = \frac{q^2}{p^2} = -M^2 = -(1-e)^2/(1 - e \cos \alpha)^2$$

The momentum dispersion of the instrument is easily seen from figure 1-5, where OP is the path of a particle that has been deflected along an arc of radius r through an angle α , and OQ is the path of a particle of slightly different momentum which has been deflected along an arc of radius $r + dr$ through an angle $\alpha + d\alpha$. In the small triangle ABC we see that

$$\begin{aligned} r d\alpha &= dr \sin \alpha \\ \text{i.e. } d\alpha &= dr \sin \alpha / r \end{aligned}$$

Also $dx_3 = q d\alpha = q dr \sin \alpha / r$

The momentum dispersion, by definition, is given by

$$\begin{aligned} D &= r dx_3 / dr = q \sin \alpha \\ &= Re \sin \alpha / (1 - e \cos \alpha) \end{aligned} \tag{1-14}$$

We observe in passing that by substituting

$$\sin \alpha = r/f = \frac{r(p + q)}{pq}$$

into (1-14) we get

$$D = r(1 + q/p) = r(1 - M) \tag{1-15}$$

Finally, the first order resolution is defined by

$$R = -(D/M)(1/x_0) = p \sin \alpha / x_0. \tag{1-16}$$

where x_0 is the source width.

(e) Projections on the Focal Plane

The magnification and momentum dispersion calculated above are in the

FIGURE 1-5

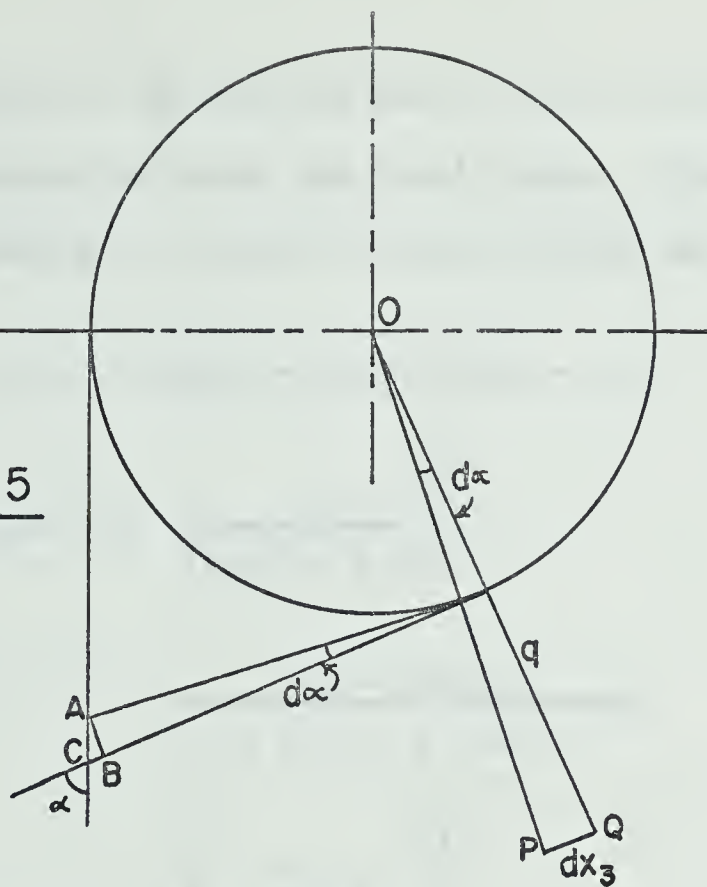
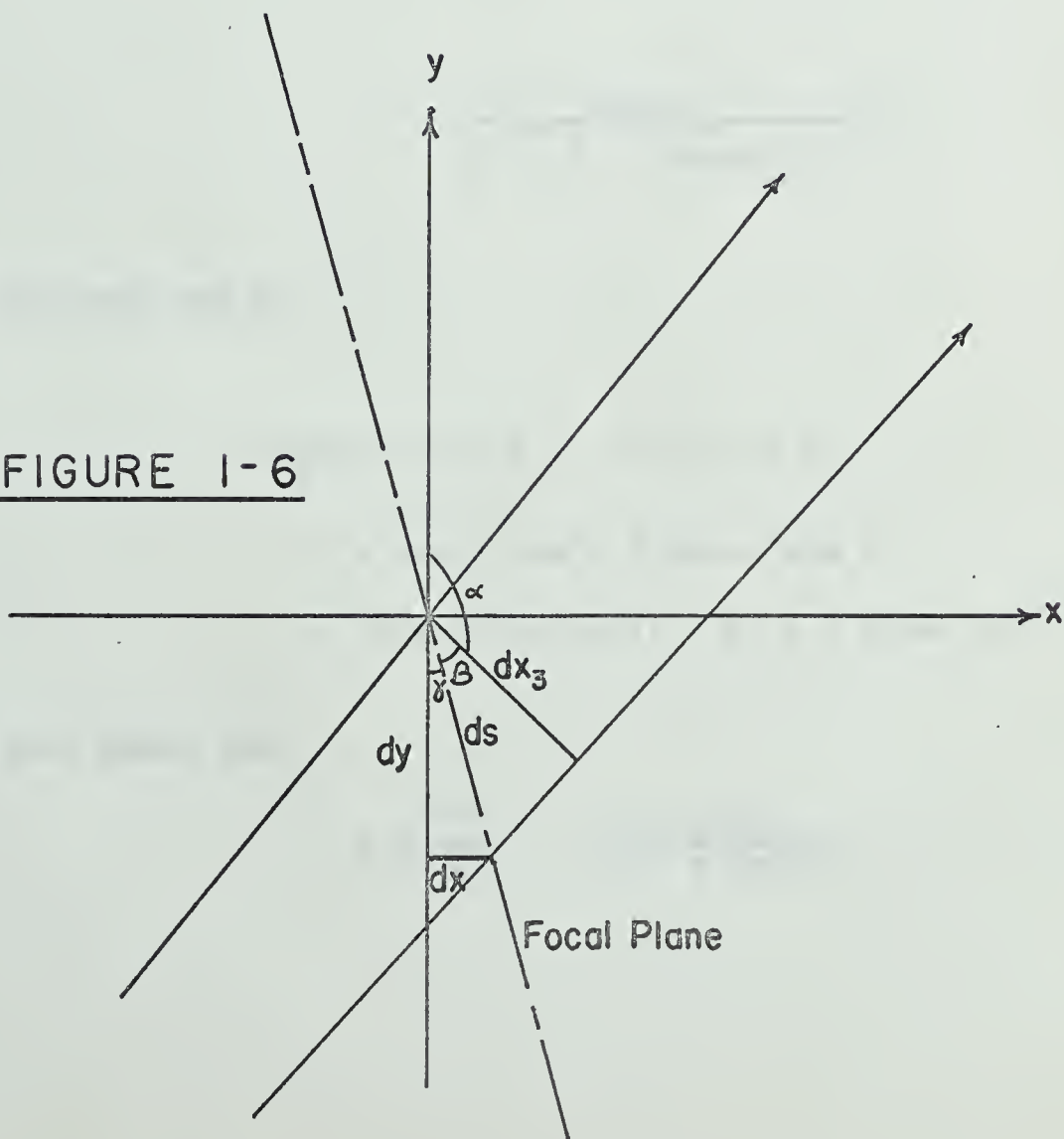


FIGURE 1-6



direction perpendicular to the central ray. It is often necessary, however, to evaluate these properties along the focal plane. This is easily accomplished by appealing to figure 1-6 from which we see

$$\tan \gamma = dx/dy = \sin \alpha / (\cos \alpha - e) \quad (1-12)$$

It follows that

$$\begin{aligned} \cos \gamma &= \left[\frac{1}{(\tan^2 \alpha + 1)} \right]^{1/2} \\ &= \frac{(e - \cos \alpha)}{(1 + e^2 - 2 e \cos \alpha)^{1/2}} \end{aligned} \quad (1-17)$$

and

$$\begin{aligned} \sin \gamma &= \left[\frac{\tan^2 \alpha}{(\tan^2 \alpha + 1)} \right]^{1/2} \\ &= \frac{\sin \alpha}{(1 + e^2 - 2 e \cos \alpha)^{1/2}} \end{aligned} \quad (1-18)$$

We can now make use of

$$\begin{aligned} dx_3/ds &= \cos \beta = - \cos (\alpha + \gamma) \\ &= - \cos \alpha \cos \gamma + \sin \alpha \sin \gamma \\ &= (1 - e \cos \alpha) / (1 + e^2 - 2 e \cos \alpha)^{1/2} \end{aligned}$$

Now we have shown that

$$M = \frac{dx_3}{dx_0} = \frac{(1 - e)}{(1 - e \cos \alpha)}$$

Therefore the magnification along the focal plane is given by

$$M_s = \frac{ds}{dx_0} = \frac{dx_3}{dx_0} \frac{ds}{dx_3} = \frac{(1 - e)(1 + e^2 - 2e \cos \alpha)^{1/2}}{(1 - e \cos \alpha)^2} \quad (1-19)$$

Similarly, we have shown the momentum dispersion to be

$$D_p = \frac{P dx_3}{dP} = \frac{Re \sin \alpha}{(1 - e \cos \alpha)}$$

so that the momentum dispersion observed along the focal plane will be

$$D_{ps} = \frac{P ds}{dP} = \frac{P dx_3}{dP} \frac{ds}{dx_3} = \frac{Re \sin \alpha (1 + e^2 - 2e \cos \alpha)^{1/2}}{(1 - e \cos \alpha)^2} \quad (1-20)$$

CHAPTER 2: MATRIX FORMULATION

1. General Theory

(a) Matrix Equations

Many excellent discussions describing the use of a matrix representation for ray tracing in both geometrical (light) optics and electron or ion optics may be found in the literature. (Halbach, 1964; Haddock, 1965; Penner, 1961; Davies, 1966). In this chapter, therefore, only a brief outline of the general formalism will be attempted, before use is made of the method to describe the spectrograph-spectrometer.

To describe a ray at a reference plane, which is always perpendicular to the optical axis, we introduce the two quantities x and x' illustrated in figure 2-1. The distance between the optical axis and the intersection between the ray and the reference plane is given by x , whereas x' is an abbreviation for dx/ds , describing the change dx in x when the reference plane is displaced by ds . The object of tracing a ray is to establish the relation between x , x' of some initial reference plane x , x' of any other reference plane of interest. In deriving these relations, we assume both x and x' to be small enough so that only the lowest significant powers of x and x' have to be taken into account. This leads to equations that are linear in x and x' , and is known as the "paraxial" approximation, allowing us to refer to x' as the angle between the ray and the optical axis.

RAY TRACING

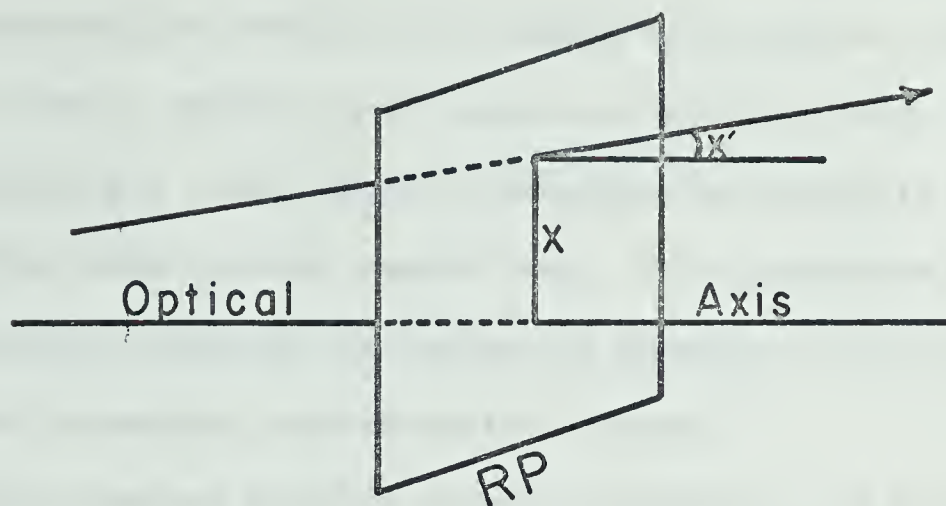
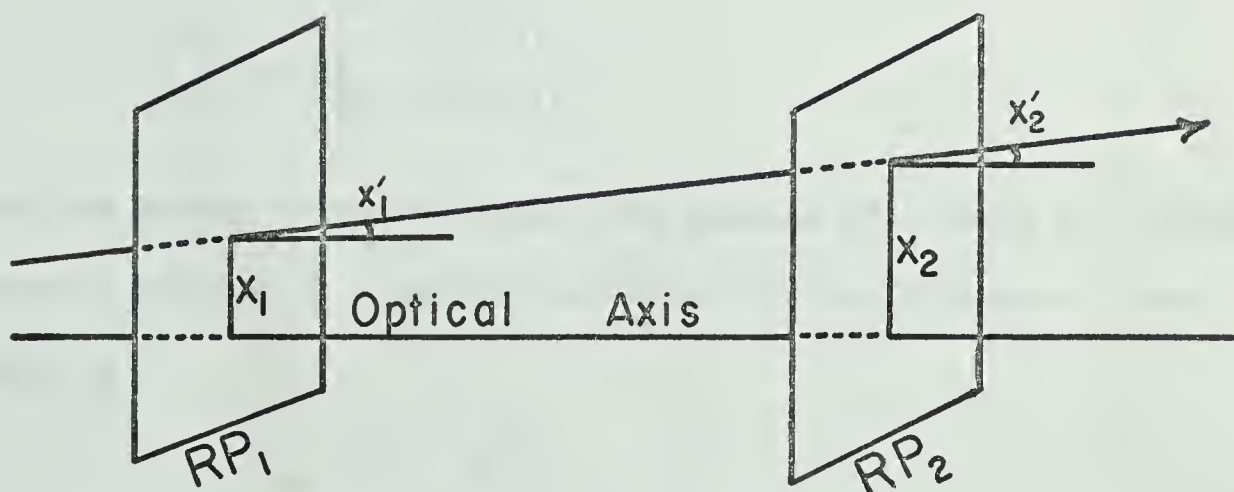


FIGURE 2 - 1



$\longleftarrow l_2 \longrightarrow$

FIGURE 2 - 2

The method of matrix optics then, is to derive, in any way, the equations describing the effect of an element of an optical system on x and x' , and then to express these equations in matrix form. The fact that the equations are linear leads to the important property that makes the matrix method useful, namely that: "the properties of successive piecewise constant regions may be obtained by the multiplication of their respective transformation matrices."

As the very simplest possible example, consider a ray moving in a homogeneous medium at an angle x' to the optical axis. (Figure 2-2). At RP_1 the ray is described by x_1 and x'_1 . After traversing a distance ℓ_2 to RP_2 it may be described by the coordinates:

$$x_2 = x_1 + \ell_2 x'_1$$

$$x'_2 = x'_1$$

These two equations may be written in matrix form:

$$\begin{bmatrix} x_2 \\ x'_2 \end{bmatrix} = \begin{bmatrix} 1 & \ell_2 \\ 0 & 1 \end{bmatrix} \begin{bmatrix} x_1 \\ x'_1 \end{bmatrix}$$

Thus the matrix which represents the passage of a light ray through a homogeneous medium, or a charged particle drifting through a field free space is

$$M = \begin{bmatrix} 1 & \ell_2 \\ 0 & 1 \end{bmatrix} \quad (2-1)$$

Similarly, the effect of any more complex optical elements can be described by a matrix equation of the form

$$\begin{bmatrix} x_2 \\ x'_2 \end{bmatrix} = \begin{bmatrix} m_{11} & m_{12} \\ m_{21} & m_{22} \end{bmatrix} \begin{bmatrix} x_1 \\ x'_1 \end{bmatrix}$$

Since x and x' are assumed small, we usually refer to x' as the angle θ between the ray and the optical axis.

In ion optics it is often useful to include the momentum dispersion $\Delta p/p$ as a third parameter in describing a ray at a reference plane. p is the ion momentum on the central ray (optical axis) and $p + \Delta p$ the momentum of the ray being traced. Thus the matrix equations which we will be using have the form

$$\begin{bmatrix} x_2 \\ \theta_2 \\ \Delta p/p \end{bmatrix} = \begin{bmatrix} m_{11} & m_{12} & m_{13} \\ m_{21} & m_{22} & m_{23} \\ m_{31} & m_{32} & m_{33} \end{bmatrix} \begin{bmatrix} x_1 \\ \theta_1 \\ \Delta p/p \end{bmatrix} \quad (2-2)$$

It should be pointed out here that the matrix formulation is not restricted to first order calculations. The second order trajectory equations can be expressed in a 9×9 matrix form, and higher order equations by still larger matrices. The second order matrix representing a uniform field wedge magnet has been derived by Brown et al (Brown, 1964).

(b) Meaning of the Matrix Elements

Consider the matrix equation 2-2 representing the effect of an optical

element or system between two reference planes. The significance of the matrix elements can be seen by letting certain elements vanish and considering the result. Unless otherwise specified we will suppose $\Delta p/p = 0$. In the case of ion optics this corresponds to the assumption that the ions whose trajectories are of interest are monoenergetic.

(i) Suppose $m_{12} = 0$. We then have the equation

$$x_2 = m_{11} x_1$$

This means that the two reference planes have an object-image relation, with the lateral magnification

$$x_2/x_1 = m_{11} .$$

(ii) Suppose $m_{11} = 0$. We then have the equation

$$x_2 = m_{12} \theta_1$$

Thus a ray parallel to the optical axis ($\theta_1 = 0$) will be focused to a point on the optical axis ($x_2 = 0$) at the exit reference plane independently of the value of x_1 . This is the definition of a focal plane, and therefore the exit reference plane of this system is a focal plane. The matrix equation is therefore

$$\begin{bmatrix} 0 \\ \theta_2 \\ 0 \end{bmatrix} = \begin{bmatrix} 0 & m_{12} & m_{13} \\ m_{21} & m_{22} & m_{23} \\ m_{31} & m_{32} & m_{33} \end{bmatrix} \begin{bmatrix} x_1 \\ 0 \\ 0 \end{bmatrix}$$

so that

$$\theta_2 = m_{21} x_1$$

The matrix element m_{21} has dimensions L^{-1} and is defined as $-1/f_2$ where f_2 is a focal length of the system. The minus sign occurs since θ_2 and x_1 have opposite signs in this situation.

(iii) Similarly, if we suppose $m_{22} = 0$, we find the first reference plane to be a focal plane of the system, so that

$$x_2 = m_{12} \theta_1$$

and m_{12} is defined as f_1 where f_1 is the other focal length of the system.

In most applications the first reference plane is fixed (at the target in our case) and so it is the second focal length which is of importance.

(iv) Finally, we consider the case where $\Delta p/p \neq 0$. We then have the equation

$$x_2 = m_{11}x_1 + m_{12} \theta_1 + m_{13} \Delta p/p$$

On the focal plane $m_{12} = 0$, so ions originating at a spot ($x_1 = 0$) on the first reference plane (the target) arrive at the second reference plane at

$$x_3 = m_{13} \Delta p/p$$

Thus

$$m_{13} = x_3 p/\Delta p$$

which by definition is the momentum dispersion of the system.

Summarizing, there are four important properties of any optical system which bear simple relationships to the matrix elements of the matrix describing the system.

1. The focal plane is given by the equation

$$m_{12} = 0 \quad (2-3)$$

2. The magnification is

$$M = m_{11} \quad (2-4)$$

3. The second focal length of the system is

$$f_2 = -1/m_{21} \quad (2-5)$$

4. The momentum dispersion of the system

$$D = m_{13} \quad (2-6)$$

(c) Lenses

The transformation between any two reference planes may be written in the form

$$\begin{bmatrix} 1 & t_e \\ 0 & 1 \end{bmatrix} \begin{bmatrix} m_{11} & m_{12} \\ m_{21} & m_{22} \end{bmatrix} \begin{bmatrix} 1 & t_i \\ 0 & 1 \end{bmatrix}$$

The dispersion terms have been ignored in the following discussion as they do not affect the argument. t_i is the distance from the first reference plane to the first principal plane of the system, and t_e the distance from the second principal plane to the second reference plane. The matrix in the middle corresponds to the transfer between the two principal planes. But the principal planes are defined as those planes having an object-image relationship with a magnification + 1. Thus

$$m_{11} = m_{22} = 1 \quad (\text{unit magnification})$$

and

$$m_{12} = 0 \quad (\text{object-image relationship})$$

Since m_{21} can be set equal to $-1/f$ without loss of generality, the transformation is

$$\begin{bmatrix} 1 & t_e \\ 0 & 1 \end{bmatrix} \begin{bmatrix} 1 & 0 \\ -1/f & 1 \end{bmatrix} \begin{bmatrix} 1 & t_i \\ 0 & 1 \end{bmatrix} = \begin{bmatrix} 1 - t_e/f & t_i + t_e - t_i t_e/f \\ -1/f & 1 - t_i/f \end{bmatrix}$$

If the reference planes have an object-image relationship, then

$$t_i + t_e - t_i t_e/f = 0$$

which reduces to the familiar lens equation

$$\frac{1}{t_i} + \frac{1}{t_e} = \frac{1}{f}$$

We see from the equation above that the principal planes of any optical system can be located by noting

$$m_{11} = 1 - t_e/f$$

and

$$m_{22} = 1 - t_i/f$$

from which

$$t_e = f(1 - m_{11})$$

(2-8)

and

$$t_i = f(1 - m_{22})$$

A thin lens is defined as a lens for which the two principal planes coincide. It is evident from the foregoing that the matrix representing the effect of such a lens is

$$\begin{bmatrix} 1 & 0 \\ -1/f & 1 \end{bmatrix}$$

The transformation through two individually thin lenses with center to center distance t , and focal lengths f_1 and f_2 respectively is therefore

$$\begin{bmatrix} 1 & 0 \\ -1/f_2 & 1 \end{bmatrix} \begin{bmatrix} 1 & t \\ 0 & 1 \end{bmatrix} \begin{bmatrix} 1 & 0 \\ -1/f_1 & 1 \end{bmatrix} = \begin{bmatrix} 1 - t/f_1 & t \\ -\frac{1}{f_1} - \frac{1}{f_2} + \frac{t}{f_1 f_2} & 1 - t/f_2 \end{bmatrix}$$

(2-9)

The focal length of the system is

$$\frac{1}{F} = -m_{21} = \frac{1}{f_1} + \frac{1}{f_2} - \frac{t}{f_1 f_2} \quad (2-10)$$

The entrance principal plane is a distance

$$t_i = Ft/f_2 \quad (2-11)$$

after the center of the first lens, and the exit principal plane a distance

$$t_e = Ft/f_1 \quad (2-12)$$

before the center of the second lens.

The results presented here are completely general, and may be applied even to the most complex optical system. The application of some of these ideas to the spectrograph-spectrometer system under consideration is described in the following sections.

2. The Spectrograph

(a) Derivation of the Matrix

As discussed in the previous section, the first step in setting up

the matrix formulation is to derive the equations of motion of particles in each element of the system relative to the central ray (or optical axis). For a uniform field magnet, this can be done with reference to figure 2-3. Here XYZ is the central ray, the path of a charged particle moving in a uniform field with the radius of its trajectory r . XWZ is the path of some other particle which intersects the central ray at an angle α and has a trajectory radius $r + \Delta r$.

If s is the distance along the central ray, and x is the distance between the two rays, then, with all other symbols as defined by the figure

$$\frac{dx}{ds} = \beta = \frac{\alpha}{\cos \gamma} \cos \theta = \frac{\alpha}{\cos \gamma} \cos(s/r)$$

Thus

$$x = \frac{r\alpha}{\cos \gamma} \sin(s/r) + a$$

Applying the boundary condition

$$x = 0 \quad \text{at} \quad s/r = -\gamma$$

and using

$$\tan \gamma = \Delta r / r\alpha$$

we find

$$a = \Delta r$$

so that for any s

$$x = \frac{r\alpha}{\cos \gamma} \sin(s/r) + \Delta r$$

At some specific distance along the central ray, s_0 , we have

$$x_0 = \frac{r\alpha}{\cos \gamma} \sin(s_0/r) + \Delta r$$

and

$$x'_0 = \frac{\alpha}{\cos \gamma} \cos(s_0/r)$$

Consider now a distance $s_1 = s_0 + s$ along the central ray. At this point

$$x = \frac{r\alpha}{\cos \gamma} \sin \frac{s_0 + s}{r} + \Delta r$$

Expanding this we find

$$x_1 = x_0 \cos(s/r) + r \sin(s/r)x'_0 + \Delta r(1 - \cos(s/r))$$

$$\text{Therefore } x'_1 = -\frac{\sin(s/r)}{r} x_0 + \cos(s/r)x'_0 + \frac{\Delta r}{r} \sin(s/r)$$

These equations may now be put in matrix form, giving

$$\begin{bmatrix} x_1 \\ x'_1 \\ \Delta p/p \end{bmatrix} = \begin{bmatrix} \cos \theta & r \sin \theta & r(1-\cos \theta) \\ -\frac{\sin \theta}{r} & \cos \theta & \sin \theta \\ 0 & 0 & 1 \end{bmatrix} \begin{bmatrix} x_0 \\ x'_0 \\ \Delta p/p \end{bmatrix}$$

We have used the fact that

$$\frac{\Delta p}{p} = \frac{\Delta r}{r}$$

and now, for consistency with the following chapters, we make the notational changes:

$$\theta \rightarrow \alpha \quad \text{and } x' \rightarrow \theta$$

so that the matrix equation representing the effect of a wedge magnet which deflects a particle through an angle α is

$$\begin{bmatrix} x_1 \\ \theta_1 \\ \Delta p/p \end{bmatrix} = \begin{bmatrix} \cos \alpha & r \sin \alpha & r(1-\cos \alpha) \\ -\frac{\sin \alpha}{r} & \cos \alpha & \sin \alpha \\ 0 & 0 & 1 \end{bmatrix} \begin{bmatrix} x_0 \\ \theta_0 \\ \Delta p/p \end{bmatrix} \quad (2-13)$$

and the matrix representing the effect of the magnet itself is

$$M_M = \begin{bmatrix} \cos & r \sin \alpha & r(1-\cos \alpha) \\ -\frac{\sin \alpha}{r} & \cos \alpha & \sin \alpha \\ 0 & 0 & 1 \end{bmatrix} \quad (2-13a)$$

Particles leaving the target drift a distance ℓ_1 before entering the magnet, and then a distance ℓ_2 between leaving the magnet and being observed. The total transfer matrix of the system is therefore

$$M_S = M_{\ell_2} M_M M_{\ell_1} = \begin{bmatrix} m_{11} & m_{12} & m_{13} \\ m_{21} & m_{22} & m_{23} \\ m_{31} & m_{32} & m_{33} \end{bmatrix}$$

where M_{ℓ_1} and M_{ℓ_2} represent the appropriate drift matrices (equation 2-1). Multiplying these three matrices together, the matrix elements for the spectrograph are

$$\begin{aligned} m_{11} &= \cos \alpha - \frac{\ell_2 \sin \alpha}{r} \\ m_{12} &= (\ell_1 + \ell_2) \cos \alpha - \frac{\ell_1 \ell_2 \sin \alpha}{r} + r \sin \alpha \\ m_{13} &= r(1 - \cos \alpha) + \ell_2 \sin \alpha \end{aligned}$$

$$\begin{aligned}
m_{21} &= -\frac{\sin \alpha}{r} \\
m_{22} &= -\frac{l_1 \sin \alpha}{r} + \cos \alpha \\
m_{23} &= \sin \alpha \\
m_{31} &= 0 \\
m_{32} &= 0 \\
m_{33} &= 1
\end{aligned} \tag{2-14}$$

In formulating this matrix, we have assumed the convention that x is positive when Δr is positive. This holds true for the spectrograph configuration described in the following chapters. However, by simply moving the magnet to the other side of the beam tube, which might frequently be done in experimental situations, x becomes negative for positive Δr . The matrix must then be inverted according to the formula (Penner, 1961).

$$M_{in} = \begin{bmatrix} -1 & 0 & 0 \\ 0 & -1 & 0 \\ 0 & 0 & 1 \end{bmatrix} \begin{bmatrix} \\ M \\ \end{bmatrix} \begin{bmatrix} -1 & 0 & 0 \\ 0 & -1 & 0 \\ 0 & 0 & 1 \end{bmatrix} \tag{2-15}$$

in order to describe the new situation.

This inversion does not affect most of the properties described in the following sections, but does have an important effect on the kinematic displacement of the focal plane which will be discussed in section c.

(b) The Matrix Elements(i) Focal Length

As discussed in the first part of this chapter, the focal length of the system is defined by

$$-\frac{1}{F} = m_{21} = -\frac{\sin \alpha}{r}$$

or

$$F = r/\sin \alpha \quad (2-16)$$

which is the result obtained in chapter 1 from geometrical arguments.

Moreover, if we make the substitutions

$$\begin{aligned} \ell_1 &= p - R_0 \\ \ell_2 &= q - R_0 \end{aligned} \quad (2-17)$$

and

$$F = r/\sin \alpha = R_0/(1-\cos \alpha)$$

we obtain

$$m_{11} = 1 - q/F \quad (2-18)$$

and

$$m_{22} = 1 - p/F \quad (2-19)$$

Comparing these with equations (2-8) the system is equivalent to a lens whose incident principal plane is a distance p from the target, and exit principal plane is a distance q from the detector. From the definitions of p and q , the principal planes are coincident at the center of the magnet, justifying the assumption in Chapter 1 that the spectrograph could be treated as a thin lens.

(ii) Focal Plane

The focal plane of the system is defined by the equation (2-3)

$$m_{12} = 0$$

or

$$(\ell_1 + \ell_2) \cos \alpha + r \sin \alpha - \frac{\ell_1 \ell_2 \sin \alpha}{r} = 0 \quad (2-20)$$

provided it is assumed that $\Delta p/p = 0$. For the 90° ray, where $r = R_0$, this reduces directly to

$$R_0 - \ell_1 \ell_2 / R_0 = 0$$

or

$$\ell_2 = R_0^2 / \ell_1 \quad (2-21)$$

If we again make the substitutions 2-17, this equation reduces to the other familiar form of the lens equation

$$\frac{1}{p} + \frac{1}{q} = \frac{1}{F} .$$

(iii) Magnification

The magnification of the system is equal to the matrix element m_{11} (equation 2-4). That is

$$M = \cos \alpha - \frac{\ell_2 \sin \alpha}{r} \quad (2-22)$$

We have shown (equation 2-18) that the substitutions 2-17 give

$$m_{11} = 1 - q/F$$

On the focal plane, we have

$$F = pq/(p + q)$$

which gives

$$M = m_{11} = -q/p$$

as expected. The form of the magnification arrived at in Chapter 1 follows from the substitution

$$\frac{1}{q} = \frac{1}{F} - \frac{1}{p} = \frac{(1 - \cos \alpha)}{R_0} - \frac{1}{p}$$

which gives

$$M = \frac{R_0}{R_0 - p(1 - \cos \alpha)}$$

(iv) Dispersion and Resolution

If we let dx_3 or simply x_3 be the displacement of a particle from the central ray after it has come out of the magnet, then the momentum dispersion D is given by equation (2-6)

$$D = p \frac{dx_3}{dp} = m_{13} = r(1 - \cos \alpha) + \ell_2 \sin \alpha \quad (2-23)$$

which, upon substituting equations 2-17, becomes

$$D = p \frac{dx_3}{dp} = q \sin \alpha \quad (2-24)$$

This result is once again in agreement with that found in Chapter 1 from geometrical considerations.

Since

$$\frac{E}{dE} = \frac{1}{2} \frac{p}{dp}$$

the energy dispersion D_{en} is

$$D_{en} = E \frac{dx_3}{dE} = q \frac{\sin \alpha}{2} \quad (2-25)$$

and

$$dE = \frac{2E}{q \sin \alpha} dx_3 \quad (2-26)$$

Finally, the first order resolving power is

$$R = \frac{D_{en}}{Mx_0} = \frac{p \sin \alpha}{2 x_0} \quad (2-27)$$

(c) Kinematic Broadening

We have seen (equation 2-21) that if we assume $\Delta p/p = 0$, the first order focus for the 90° ray occurs at

$$l_2 = R_0^2 l_1$$

If, however, $\Delta p/p$ cannot be ignored, then the focus will be displaced. If the detector is not moved to the real focus, the image will appear broader than it should, an effect which is generally referred to as kinematic broadening.

From the matrix equation, the general expression for x_3 at a distance l_2' after the magnet is

$$\begin{aligned} x_3 = & \left\{ \cos \alpha - \frac{l_2' \sin \alpha}{r} \right\} x_0 \\ & + \left\{ (l_1 + l_2') \cos \alpha - \frac{l_1 l_2' \sin \alpha}{r} + r \sin \alpha \right\} \theta_0 \\ & + \left\{ r(1 - \cos \alpha) + l_2' \sin \alpha \right\} \Delta r / r \end{aligned} \quad (2-28)$$

If ℓ_1 represents the position of the target ($x_0 = 0$), then for the 90° ray, where $r = R_0$,

$$x_3 = \{R_0 - \ell_1 \ell_2' / R_0\} \theta_0 + \{R_0 + \ell_2'\} \Delta r / R_0$$

Thus the displaced focus ($x_3 = 0$) occurs when ℓ_2' satisfies the equation

$$\{R_0 - \ell_1 \ell_2' / R_0\} \theta_0 + \{R_0 + \ell_2'\} \Delta r / R_0 = 0$$

If we make the substitution

$$\ell_2' = \ell_2 - D = R_0^2 / \ell_1 - D$$

and solve for D, we find that the focus should be displaced a distance

$$\begin{aligned} D &= \frac{R_0}{\ell_1} \frac{\ell_1 + R_0}{\Delta r - \ell_1 \theta_0} \Delta r \\ &= \frac{R_0}{\ell_1} \frac{\ell_1 + R_0}{1 - \ell_1 (\theta_0 / \Delta r)} \end{aligned} \quad (2-29)$$

It must be noted here that if the inverted matrix (equation 2-15) is used in this derivation, that is, the matrix which describes the spectrograph when it is on the opposite side of the beam tube, there is an important change in this displacement, which becomes

$$D' = \frac{R_0}{\ell_1} \frac{\ell_1 + R_0}{1 + \ell_1 (\theta_0 / \Delta r)} \quad (2-30)$$

This is the displacement given by Enge (Enge, 1958) in his discussion of the kinematic broadening effect. It is evident that this is a preferable

situation, since the focus moves progressively closer to the magnet as the target nuclei become lighter ($\Delta r/\theta_0$ large). In the other case, however, the displacement moves away from the magnet, and can become infinite if

$$l_1(\theta_0/\Delta r) = 1$$

Such a situation could arise for very light target nuclei.

The factor $\Delta r/\Delta\theta$ is simply a kinematic factor which may be obtained by differentiating the general Q equation. The result is

$$\frac{1}{r} \frac{\Delta r}{\Delta\theta} = \frac{1}{2} \frac{1}{E} \frac{\Delta E}{\Delta\theta} = \frac{A \sin \theta}{1 - A \cos \theta} \quad (2-31)$$

where

$$A = \frac{(M_I M_E E_I/E_{E0})^{1/2}}{(M_R + M_E)}$$

The subscripts I, R, and E refer to the incident, residual, and outcoming particles respectively.

3. The Spectrometer

(a) Derivation of the Matrix

Enge (Enge, 1958) suggested that the solid angle of the spectrograph could be greatly enhanced by placing a quadrupole lens between the target and the spectromagnet, as illustrated in figure 2-4. The convenience of the matrix formulation becomes evident when it is used to describe this more complex system. All that need be done is to express in matrix form the equations for the trajectories of ions in the lens, and then

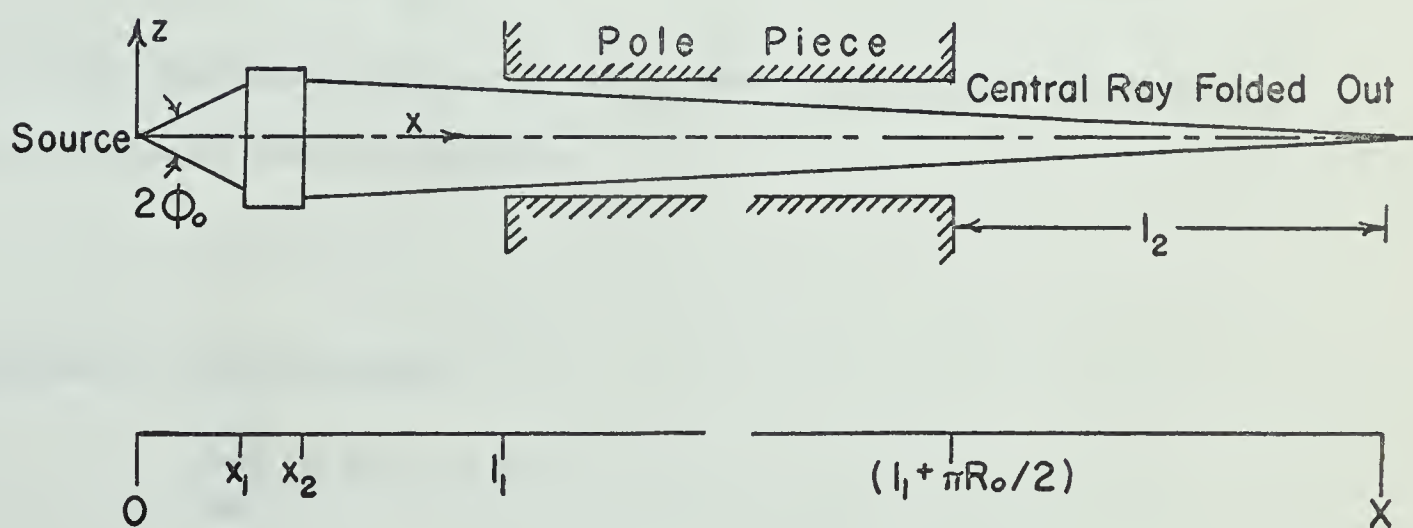
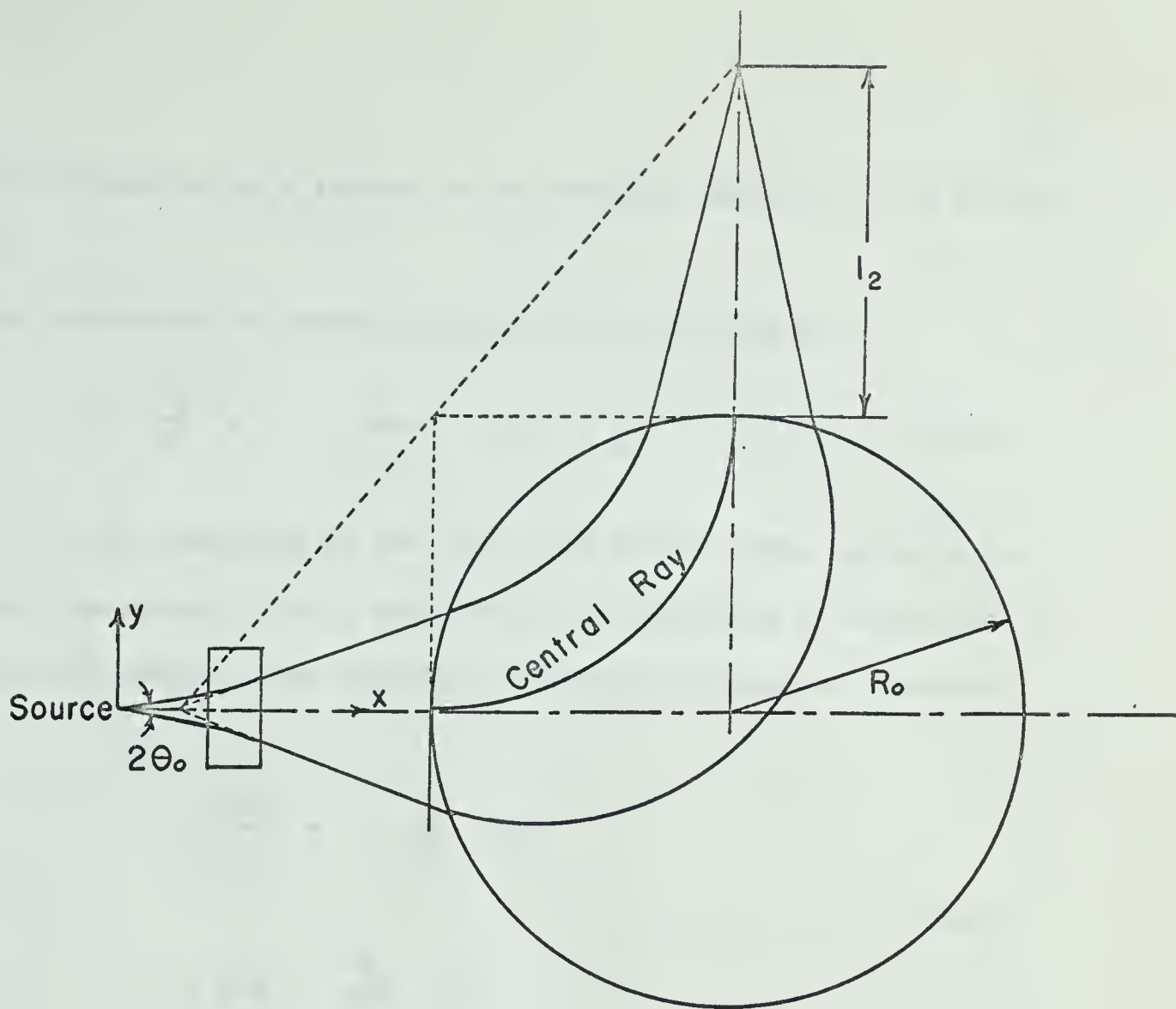


FIGURE 2 - 4

SPECTROMETER GEOMETRY

include this matrix as a factor in the transfer matrix for the entire system.

The components of magnetic induction in the lens are

$$B_z = -\frac{B_\ell}{a} y \quad \text{and} \quad B_y = -\frac{B_\ell}{a} z \quad (2-32)$$

where B_ℓ is the induction at the pole tips of the lens, and a is the distance from center line to pole tip. The equations of motion for a particle with charge q and velocity v inside the lens are therefore

$$m \frac{d^2 z}{dt^2} = -\frac{B_\ell}{a} z q v \quad (2-33)$$

and

$$m \frac{d^2 y}{dt^2} = \frac{B_\ell}{a} y q v$$

The velocity of the particles is determined by the spectromagnet to be

$$v = q B_0 r / m \quad (2-34)$$

where r is the trajectory radius and B_0 is the field in the main magnet.

If we now make the approximation

$$v_x \sim v$$

the equations of motion become

$$\frac{d^2 z}{dx^2} + k^2 z = 0$$

and

$$\frac{d^2 y}{dx^2} - k^2 y = 0 \quad (2-35)$$

where

$$k^2 = \frac{q B_\ell}{amv} = \frac{B_\ell/B_0}{ra} \quad (2-36)$$

For the 90° ray, where $r = R_0$

$$k^2 = \frac{B_\ell/B_0}{a R_0} \quad (2-37)$$

The solutions of these equations are

$$y = Y \sinh (kx + \lambda_1) \quad (2-38)$$

and

$$z = Z \sin (kx + \lambda_2)$$

If we now apply the initial conditions

$$\begin{aligned} y = y_0 & \quad ; \quad \theta_0 = (dy/dx)_0 \\ z = z_0 & \quad ; \quad \phi_0 = (dz/dx)_0 \end{aligned} \quad (2-39)$$

at the lens entrance, the values of z , y , θ , and ϕ at the exit of a lens of length L are

$$y = y_0 \cosh kL + \frac{\theta_0 \sinh kL}{k}$$

$$\theta = y_0 k \sinh kL + \theta_0 \cosh kL$$

$$z = z_0 \cos kL + \frac{\phi_0 \sin kL}{k}$$

$$\phi = -z_0 k \sin kL + \phi_0 \cos kL$$

In matrix form, these equations are

$$\begin{bmatrix} y \\ \theta \end{bmatrix} = \begin{bmatrix} M_D \end{bmatrix} \begin{bmatrix} y_0 \\ \theta_0 \end{bmatrix} \quad (2-41)$$

$$\begin{bmatrix} z \\ \phi \end{bmatrix} = \begin{bmatrix} M_C \end{bmatrix} \begin{bmatrix} z_0 \\ \phi_0 \end{bmatrix} \quad (2-42)$$

where

$$M_D = \begin{bmatrix} \cosh kL & \frac{\sinh kL}{k} \\ k \sinh kL & \cosh kL \end{bmatrix} \quad (2-43)$$

and

$$M_C = \begin{bmatrix} \cos kL & \frac{\sin kL}{k} \\ -k \sin kL & \cos kL \end{bmatrix} \quad (2-44)$$

Here M_D represents the effect of the quadrupole lens in the y plane, the plane in which the trajectories diverge. M_C is the effect of the lens in the z plane, the plane in which trajectories converge.

In general, any element which does not deflect the central trajectory produces no first order dispersion (Penner, 1961). Thus the three dimensional matrices for the quadrupole are

$$M_D = \begin{bmatrix} \cosh kL & \frac{\sinh kL}{k} & 0 \\ k \sinh kL & \cosh kL & 0 \\ 0 & 0 & 1 \end{bmatrix} \quad (2-45)$$

and

$$M_C = \begin{bmatrix} \cos kL & \frac{\sin kL}{k} & 0 \\ -k \sin kL & \cos kL & 0 \\ 0 & 0 & 1 \end{bmatrix} \quad (2-46)$$

In the y plane, particles leaving the target drift a distance x_1 before entering the quadrupole, a distance $(\ell_1 - x_2)$ between the quadrupole and the magnet, and then a distance ℓ_2 between the magnet and the detector. The matrix representing the entire system in this plane is thus

$$M_y = M_{\ell_2} M_M M_{(\ell_1 - x_2)} M_D M_{x_1}$$

$$= \begin{bmatrix} y_{11} & y_{12} & y_{13} \\ y_{21} & y_{22} & y_{23} \\ y_{31} & y_{32} & y_{33} \end{bmatrix}$$

Multiplying these five matrices together, we find

$$y_{11} = \cos \alpha \{ \cosh kL + (\ell_1 - x_2)k \sinh kL \} + kr \sin \alpha \sinh kL$$

$$- \frac{\ell_2 \sin \alpha}{r} \{ \cosh kL + (\ell_1 - x_2)k \sinh kL \} + k\ell_2 \cos \alpha \sinh kL$$

$$y_{12} = \cos \alpha \{ x_1 \cosh kL + \frac{\sinh kL}{k} + (\ell_1 - x_2)(x_1 k \sinh kL + \cosh kL) \}$$

$$+ r \sin \alpha \{ x_1 k \sinh kL + \cosh kL \}$$

$$- \frac{\ell_2 \sin \alpha}{r} \{ x_1 \cosh kL + \frac{\sinh kL}{k} + (\ell_1 - x_2)(x_1 k \sinh kL + \cosh kL) \}$$

$$+ \ell_2 \cos \alpha \{ x_1 k \sinh kL + \cosh kL \}$$

$$y_{13} = r(1 - \cos \alpha) + \ell_2 \sin \alpha$$

$$y_{21} = -\frac{\sin \alpha}{r} \{ \cosh kL + (\ell_1 - x_2)k \sinh kL \} + k \cos \alpha \sinh kL$$

$$y_{22} = -\frac{\sin \alpha}{r} \{ x_1 \cosh kL + \frac{\sinh kL}{k} + (\ell_1 - x_2)(x_1 k \sinh kL + \cosh kL) \} \\ + \cos \alpha \{ x_1 k \sinh kL + \cosh kL \}$$

$$y_{23} = \sin \alpha$$

$$y_{31} = 0$$

$$y_{32} = 0$$

$$y_{33} = 1 \quad (2-47)$$

In the z plane, particles leaving the target drift a distance x_1 before entering the quadrupole, and then drift a distance $X - x_2$ (where $X = \ell_1 + \pi r/2 + \ell_2$) between the quadrupole exit and the detector. In this plane, the transfer matrix is therefore

$$M_z = M_{X-x_2} M_c M_{x_1}$$

$$= \begin{bmatrix} z_{11} & z_{12} & z_{13} \\ z_{21} & z_{22} & z_{23} \\ z_{31} & z_{32} & z_{33} \end{bmatrix}$$

Multiplying these matrices together gives

$$z_{11} = \cos kL - (X - x_2)k \sin kL$$

$$\begin{aligned}
z_{12} &= x_1 \cos kL + \frac{\sin kL}{k} + (X - x_2)(\cos kL - kx_1 \sin kL) \\
z_{13} &= 0 \\
z_{21} &= -k \sin kL \\
z_{22} &= \cos kL - x k \sin kL \\
z_{23} &= 0 \\
z_{31} &= 0 \\
z_{32} &= 0 \\
z_{33} &= 1
\end{aligned} \tag{2-48}$$

(b) The Matrix Elements

(i) The Focal Planes

The y plane focus is defined by equation (2-2).

$$y_{12} = 0$$

For the 90° ray, where $r = R_0$, this gives the equation

$$\begin{aligned}
-\frac{\ell_2}{R_0} \{x_1 \cosh kL + \frac{\sinh kL}{k} + (\ell_1 - x_2)(x_1 k \sinh kL + \cosh kL)\} \\
+ R_0 \{x_1 k \sinh kL + \cosh kL\} = 0
\end{aligned} \tag{2-49}$$

This can be solved for ℓ_2 , with the result

$$\ell_2 = \frac{R_0^2 (x_1 k \sinh kL + \cosh kL)}{x_1 \cosh kL + \frac{\sinh kL}{k} + (\ell_1 - x_2)(x_1 k \sinh kL + \cosh kL)} \tag{2-50}$$

The z plane focus is defined by the equation

$$z_{12} = 0$$

which, for the 90° ray, reduces to

$$x_1 \cos kL + \sin kL/k + (X - x_2)(\cos kL - kx_1 \sin kL) = 0$$

or

$$-(X - x_2) = \frac{1}{k} \left[\frac{kx_1 + \tan kL}{1 - kx_1 \tan kL} \right] \quad (2-51)$$

(ii) Magnification, Dispersion, Resolution

The y plane magnification is given by y_{11} , which, for the 90° ray, reduces to

$$M_y = y_{11} = R_0 k \sinh kL - \frac{\ell_2}{R_0} \{ \cosh kL + (\ell_1 - x_2) k \sinh kL \} \quad (2-52)$$

Equation 2-50 may now be used to eliminate ℓ_1 from this expression, resulting in the following convenient expression for the y plane magnification at the focal plane.

$$M_y = \frac{-\ell_2/R_0}{x_1 k \sinh kL + \cosh kL} \quad (2-53)$$

The z plane magnification may be read directly from the matrix

$$M_z = z_{11} = \cos kL - (X - x_2) \sin kL \quad (2-54)$$

Because no dispersion occurs in the quadrupole lens, the momentum dispersion of the instrument has the same form as for the spectrograph, namely

$$\begin{aligned} D = y_{13} &= p \frac{dx_3}{dp} = r(1 - \cos \alpha) + \ell_2 \sin \alpha \\ &= q \sin \alpha \end{aligned} \quad (2-55)$$

The numerical value of the dispersion will, of course, differ, since q is greater in the spectrometer mode.

Arguing as in the last section, the resolving power of the instrument is

$$R_1 = \frac{q \sin \alpha}{2 M_y x_0} \quad (2-56)$$

where the value of M_y may be substituted from equation 2-53.

(c) Thin Lens Approximation

Dr. Karl Brown (Brown, 1965b) has suggested an alternate formulation, based on the approximation that the quadrupole lens may be treated as a thin lens. We have (equation 2-8) that for a thick lens, the positions of the principal planes are defined by

$$\begin{aligned} t_e &= f(1 - m_{11}) \\ t_i &= f(1 - m_{22}) \end{aligned} \quad (2-8)$$

With reference to equation 2-43, we see that for the quadrupole lens in the y plane

$$f = -1/m_{21} = -1/k \sinh kL \quad (2-57)$$

Using this in equations 2-8 gives

$$t_e = t_i = \frac{(\cosh kL - 1)}{k \sinh kL} \quad (2-58)$$

This expression can be expanded in powers of kL to give

$$t_e = t_i = \frac{L}{2} \left\{ 1 + \frac{1}{12} k^2 L^2 + \dots \right\} \quad (2-59)$$

A lens is thin if the two principal planes coincide. By symmetry, this requires

$$t_i = t_e = L/2 \quad .$$

Comparing this with equation 2-59, we see that the thin lens approximation is valid provided

$$k^2 L^2 \ll 1$$

If we treat the quadrupole as a thin lens, then, since we have already shown the spectromagnet to be a thin lens, the system may be described simply as two thin lenses separated by a distance t . The geometry of this situation is illustrated in figure 2-5. The focal lengths of the lenses are

$$f_q = -1/k \sinh kL$$

and

$$f_m = r/\sin \alpha$$

respectively. In the thin lens approximation

$$1/f_q = -k^2 L \left(1 + \frac{k^2 L^2}{6} + \dots \right) \approx -k^2 L$$

or

$$f_q = -1/k^2 L$$

The focal length of the entire system is given by equation 2-10

$$\frac{1}{F} = \frac{1}{f_q} + \frac{1}{f_m} - \frac{t}{f_q f_m} \quad (2-60)$$

The principal planes of the system are located at (2-11, 2-12)

$$t_i = Ft/f_m$$

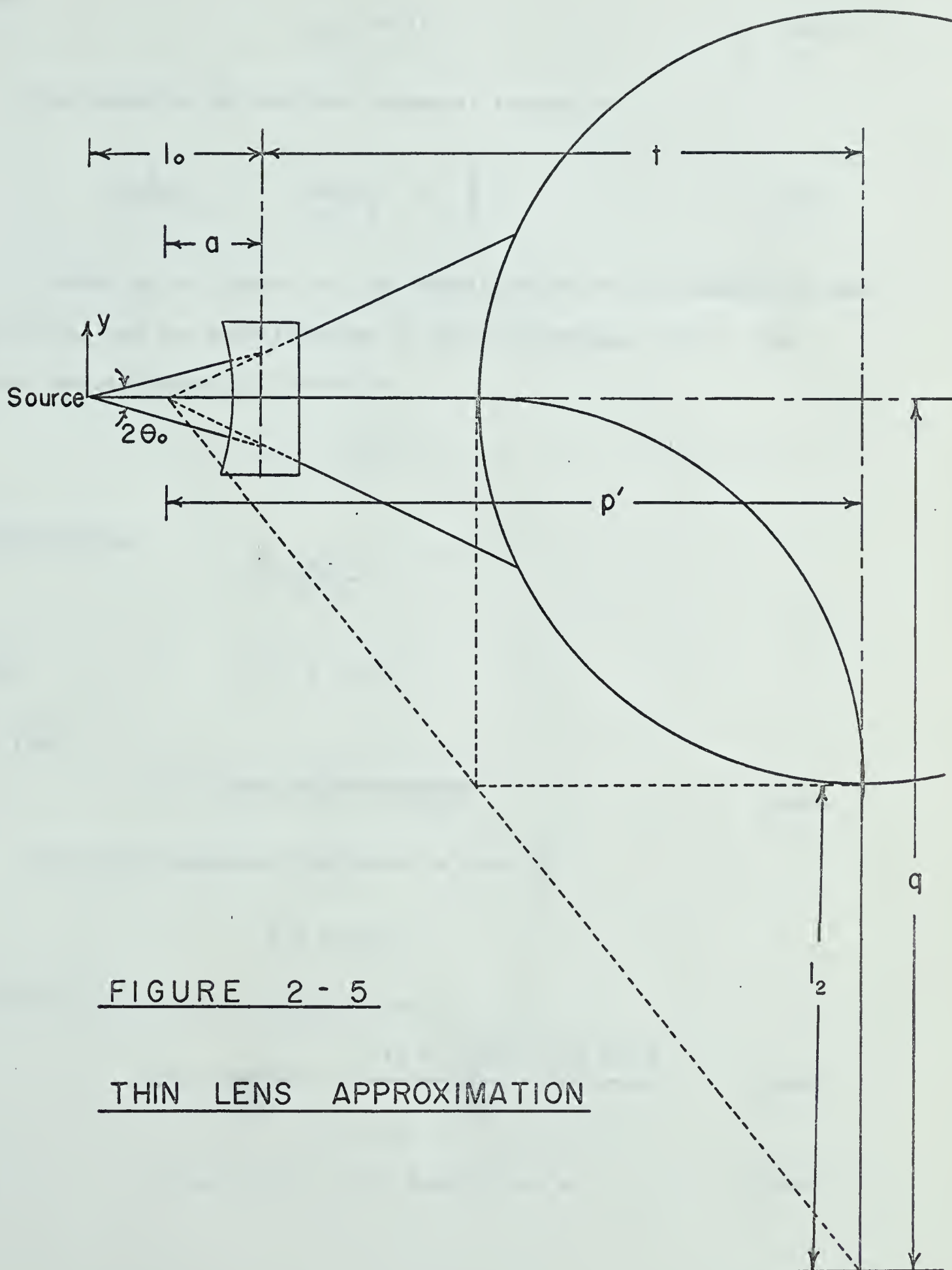


FIGURE 2 - 5

THIN LENS APPROXIMATION

and

$$t_e = Ft/f_q \quad (2-61)$$

The equation of the focal plane is therefore

$$\frac{1}{\ell_0 + t_i} + \frac{1}{t_e + q} = \frac{1}{F} \quad (2-62)$$

Referring to figure 2-5, the magnification of the quadrupole lens is $-a/\ell_0$, and the magnification of the spectromagnet $-q/p'$. The total magnification is therefore

$$M_y = q a/p' \ell_0$$

Substituting

$$a = \frac{f_q \ell_0}{f_q - \ell_0}$$

and

$$p' = t + |a|$$

we find

$$M_y = \frac{q}{[\ell_0 + t(1 - \ell_0/f_q)]} \quad (2-63)$$

Since the momentum dispersion is given by

$$D = q \sin \alpha$$

the first order resolving power is

$$R_1 = \frac{D}{M_y x_0} = \frac{[\ell_0 + t(1 - \ell_0/f_q)] \sin \alpha}{x_0} \quad (2-64)$$

or

$$R_1 x_0 = [\ell_0 + t(1 + \ell_0 L k^2)] \sin \alpha \quad (2-65)$$

It should be pointed out that expressions 2-62, 63 and 64 may all be applied even without assuming the quadrupole to be a thin lens, provided that the distances l_0 and t are measured from the principal planes of the lens. In this case the method reduces to the complete matrix method described earlier, since the positions of the principal planes must be determined (introducing cosh terms) and the exact focal length must be used (introducing sinh terms).

(d) Solid Angle

The matrix formulation also provides a means of evaluating the solid angle of the spectrometer system. As illustrated in figure 2-6, the maximum allowable excursion in the lens is assumed to be $a/\sqrt{2}$. In the diverging plane, this must occur at the lens exit, a distance L through the lens. The transfer from the target to the end of the lens is therefore

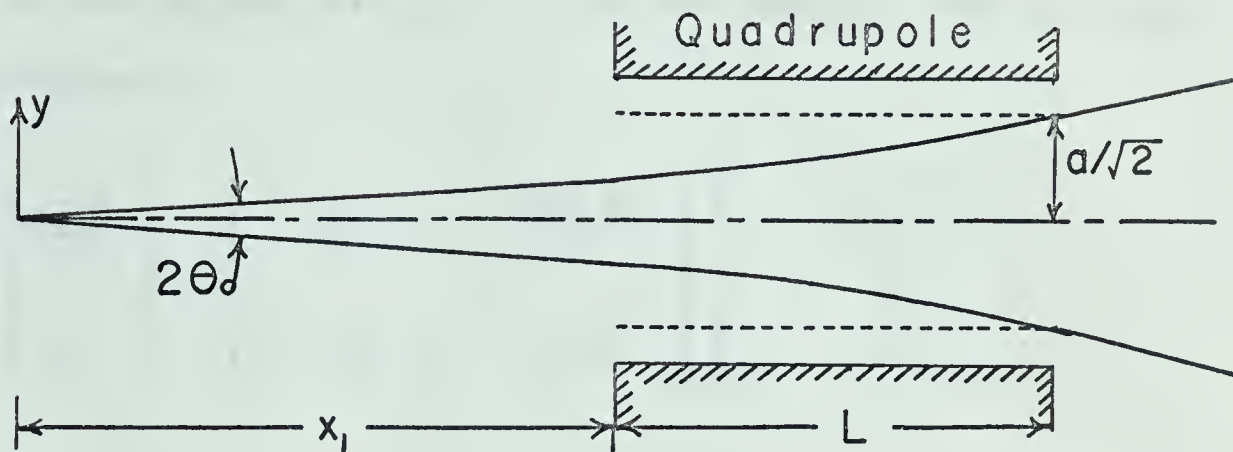
$$\begin{bmatrix} a/\sqrt{2} \\ \theta_2 \end{bmatrix} = \begin{bmatrix} \cosh kL & \frac{\sinh kL}{k} \\ k \sinh kL & \cosh kL \end{bmatrix} \begin{bmatrix} 1 & x_1 \\ 0 & 1 \end{bmatrix} \begin{bmatrix} 0 \\ \theta_0 \end{bmatrix}$$

from which

$$a/\sqrt{2} = (x_1 \cosh kL + \frac{\sinh kL}{k})\theta_0$$

$$\text{or } \theta_0 = \frac{ka}{\sqrt{2}} \frac{1}{(kx_1 \cosh kL + \sinh kL)} \quad (2-66)$$

DIVERGING PLANE



CONVERGING PLANE

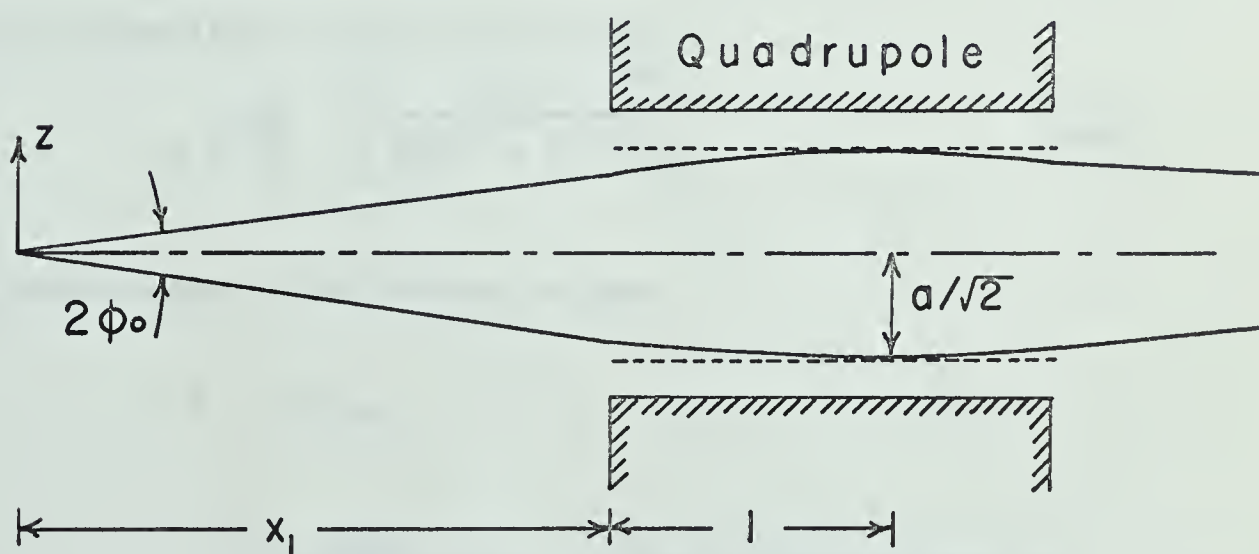


FIGURE 2 - 6 SOLID ANGLE CALCULATIONS

In the converging plane, the maximum excursion $a/\sqrt{2}$ is reached at some distance ℓ inside the lens. At this position the ray is parallel to the optical axis ($\phi_2 = 0$), so the transfer from the target to this position is

$$\begin{bmatrix} a/\sqrt{2} \\ 0 \end{bmatrix} = \begin{bmatrix} \cos k\ell & \frac{\sin k\ell}{k} \\ -k \sin k\ell & \cos k\ell \end{bmatrix} \begin{bmatrix} 1 & x_1 \\ 0 & 1 \end{bmatrix} \begin{bmatrix} 0 \\ \phi_0 \end{bmatrix}$$

from which

$$\phi_0(\cos k\ell - x_1 k \sin k\ell) = 0 \quad (2-67)$$

and

$$\frac{ka}{\sqrt{2}} = (kx_1 \cos k\ell + \sin k\ell)\phi_0 \quad (2-68)$$

From 2-67 we have

$$k\ell = \tan^{-1}(1/kx_1)$$

which can be substituted into 2-68 to give

$$\phi_0 = \frac{ka}{\sqrt{2}} \left[\frac{1}{(x_1^2 k^2 + 1)^{1/2}} \right] \quad (2-69)$$

The solid angle of the system is then

$$\begin{aligned} \Omega &\sim 4\theta_0 \phi_0 \\ &= \frac{2a^2 k^2}{(x_1^2 k^2 + 1)^{1/2}} \frac{1}{(kx_1 \cosh kL + \sinh kL)} \quad (2-70) \end{aligned}$$

Account must, of course, be taken of any other stops in a particular experimental arrangement, as has been done in the solid angle calculation in Chapter 5, section e.

PART II: EXPERIMENTAL

CHAPTER 3: APPARATUS

(a) The Spectromagnet and Base

The experiment involved the alignment and calibration of the University of Alberta 50 cm. magnetic spectrograph-spectrometer of the Browne-Buecher-Enge type.*

This magnet has been placed in the horizontal position suggested by Enge (Enge, 1958) so that the kinematic broadening effects can be eliminated in spectrometer applications. It rests on three 1-1/2" bolts fixed to a rotating carriage which allows the system to be rotated to various angles of observation between + 175° and - 125°. These bolts allow an adjustment of 1-1/2 inches in the height of the magnet, and are necessary both for levelling and for bringing the center of the 3/4 inch magnet gap to beam height. The bolts in turn fit three adjustable pads mounted on the magnet side, which allow some variation of the magnet position relative to the rotating carriage.

The carriage rolls on a machined I beam 100 inches in diameter which has been carefully levelled and grouted with epoxy grout to a cement base in the laboratory floor.

The magnet pole pieces are made of DC magnetic ingot iron, while the remaining portions of the magnetic circuit are manufactured from C1010 steel plate.

*Spectromagnetic Industries Ltd., Hayward, California.

The coils are wound with hollow core copper conductor and are water cooled. The individual conductors are insulated with cotton tape, and the entire coil impregnated with epoxy resin and cured.

The magnet is powered from the same current regulated power supply model BR6538* which is used for the University of Alberta Mobley time compression magnet. This power supply provides up to 210 amps regulated to 0.001 % for 10% line per load change. At 125 amps the gap field of the magnet is 12 kilogauss.

The manufacturer's specifications claim a field uniformity at 7000 gauss of $\Delta B/B$ better than 0.1% over 2 inches from the pole edges, and nuclear magnetic resonance measurements indicate that this specification is satisfied. Figure 3-1 is the magnet induction curve provided by the manufacturer.

(b) The Quadrupole Lens

As suggested by Enge, the spectromagnet is fitted with a quadrupole lens in order to increase the effective solid angle when used as a spectrometer. The yoke structure of this lens is of low carbon steel plate. The coils are the same as those described for the main magnet above, the four water cooling circuits being connected in parallel while the four electrical circuits are in series.

The physical length of the lens is 4 inches, with a bore diameter of 1.375". The coils are connected in series with the coils of the main

* Spectromagnetic Industries Ltd., Haywood, California

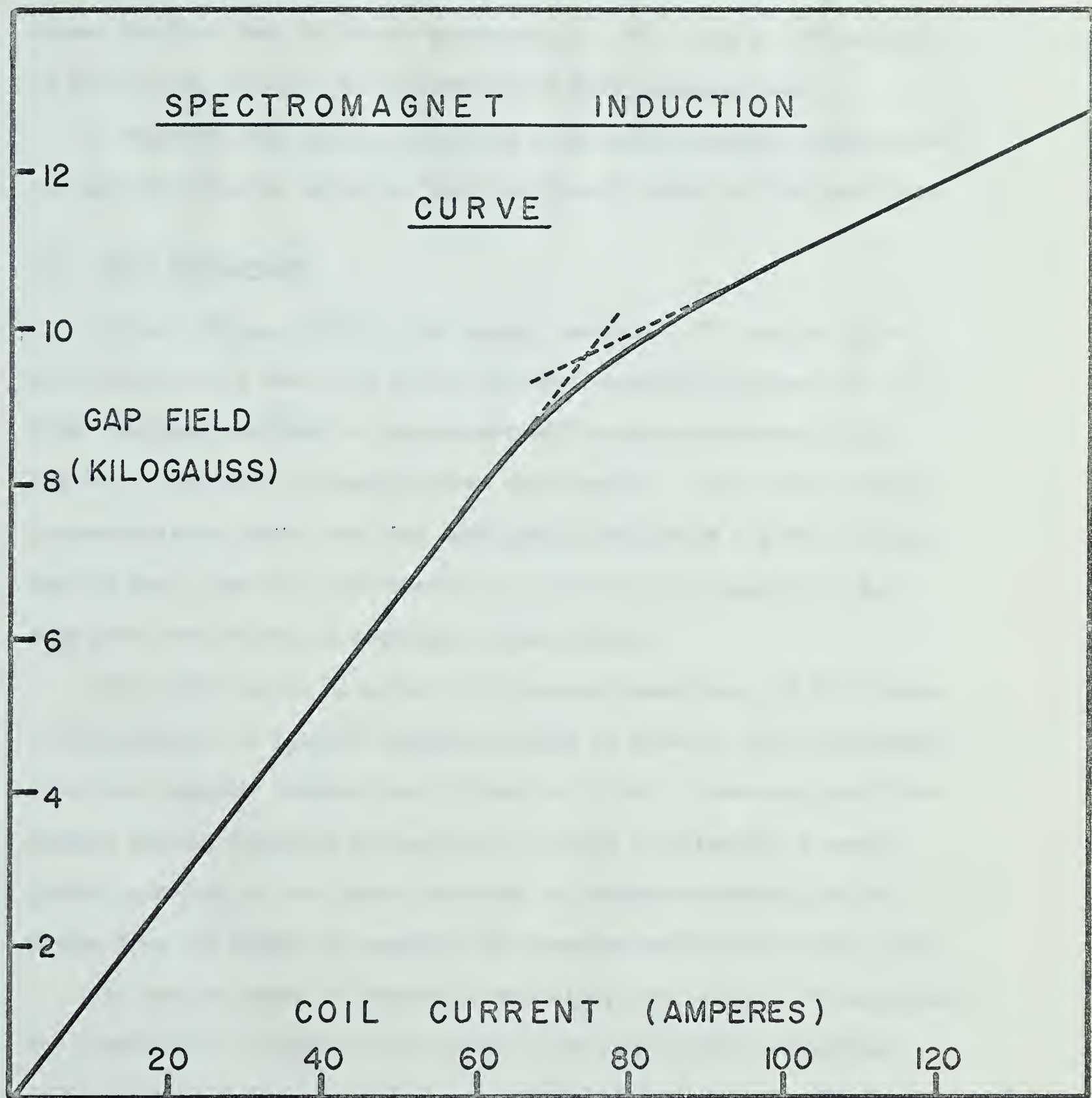


FIGURE 3 - 1

magnet, with an automatic shorting switch in the main power supply to bypass the lens when it is not in operation. The field at 100 amperes is 6000 gauss, giving a field gradient of 8400 gauss per inch.

A separate trim supply, providing a maximum 45 amperes superimposed through the coils in either a "buck" or "boost" mode, is also available.

(c) Field Measurement

Because the gap width of the magnet was only 3/4", smaller than most commercially available nuclear magnetic resonance probes, Dr. W. C. Olsen designed and built a transistorized frequency modulated N.M.R. system for use with the spectrometer installation. This system, which is particularly useful for this application because of its small probes and the fact that their orientation in the field is unimportant, has been described in detail elsewhere (Olsen, 1962).

Four probes serve to cover the frequency range from 4.8 to 55 Mc/s corresponding to a range of magnetic fields of from 1.1 to 13 kilogauss, or proton energies ranging from 150 keV to 25 MeV. These can easily be changed without breaking the vacuum. In order to eliminate a severe pick-up problem, it was found necessary to insulate electrically the probes from the magnet by wrapping the grounded shield with teflon tape.

The entire system is remotely controlled, with only the RF oscillator and preamplifier located at the magnet. The tank circuit capacitance is varied by a selsyn motor drive geared down by a ratio of approximately 60 to 1. The proton resonance is displayed on an oscilloscope*, and the

* James Millen Mfg. Co. Inc., Malden, Massachusetts

resonant frequency on a frequency meter (Hewlett Packard Model 524C).

Although it represents no great inconvenience, occasional adjustments do have to be made to the amplitudes of both the RF and 200 cps modulating frequencies to maintain large resonance signals. It was also found useful to leave all power supplies running continuously, as the warm-up time is a few hours. Otherwise, the system operates satisfactorily over its entire frequency range, with a long-term drift of only 4 - 5 kilocycles in as many hours.

(d) The Target Chamber

Mounted over the center axis of the rotating base is a target chamber of the sliding seal type designed and built in this laboratory. Contrary to usual practice, it is mounted such that the chamber itself is fixed in space, and the sliding seal moves as the system is rotated. This keeps the target angle constant for various positions of the system.

As well as the target support itself, the chamber contains facilities for a Faraday cup with electron suppression, and a monitor counter. The top is easily removed for changing of targets.

The principal features of the target chamber design are indicated in figure 3-2. It is manufactured of brass, with walls 3/16" thick, a lucite top, and a teflon base. The sliding seal is of .006" stainless steel. The coupling to the main magnet is designed to allow some axial movement to compensate for any lack of concentricity and is also shown in figure 3-2. Further discussion of the target chamber may be found in Appendix B.

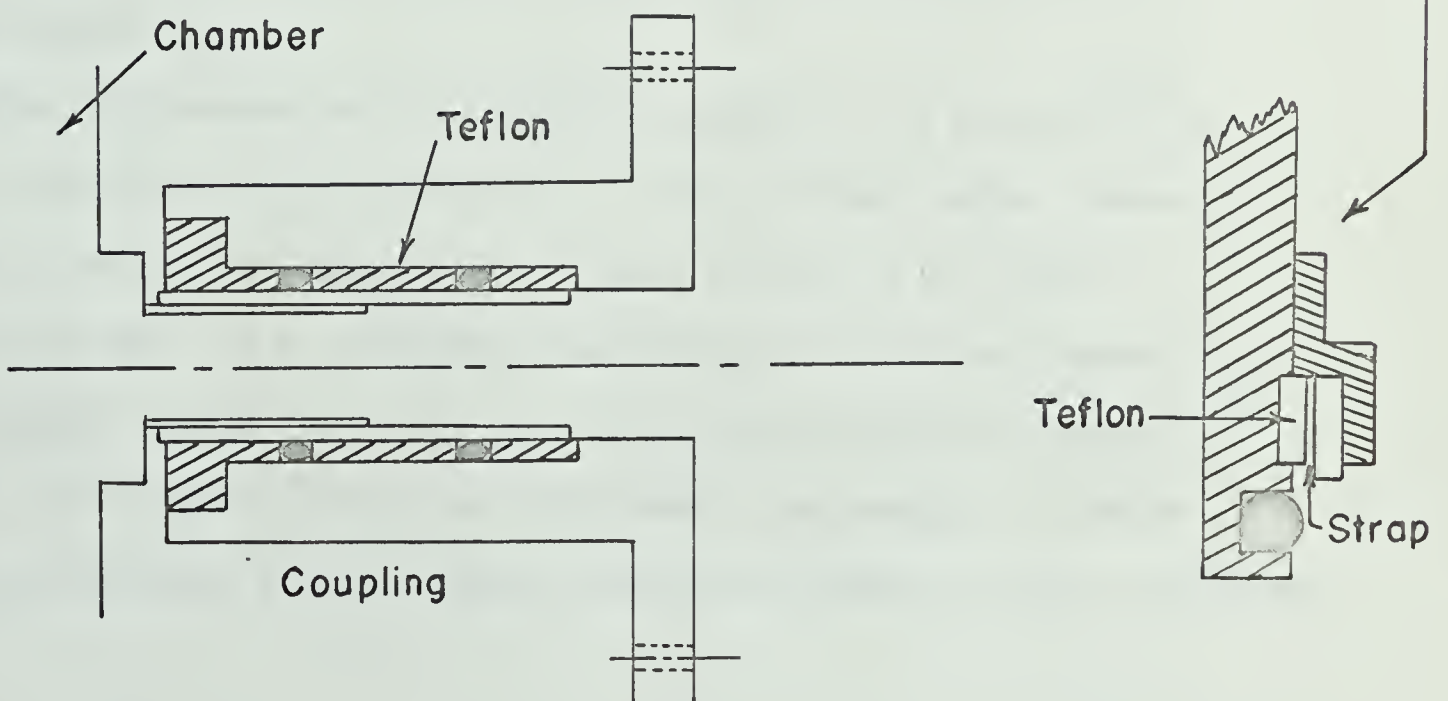
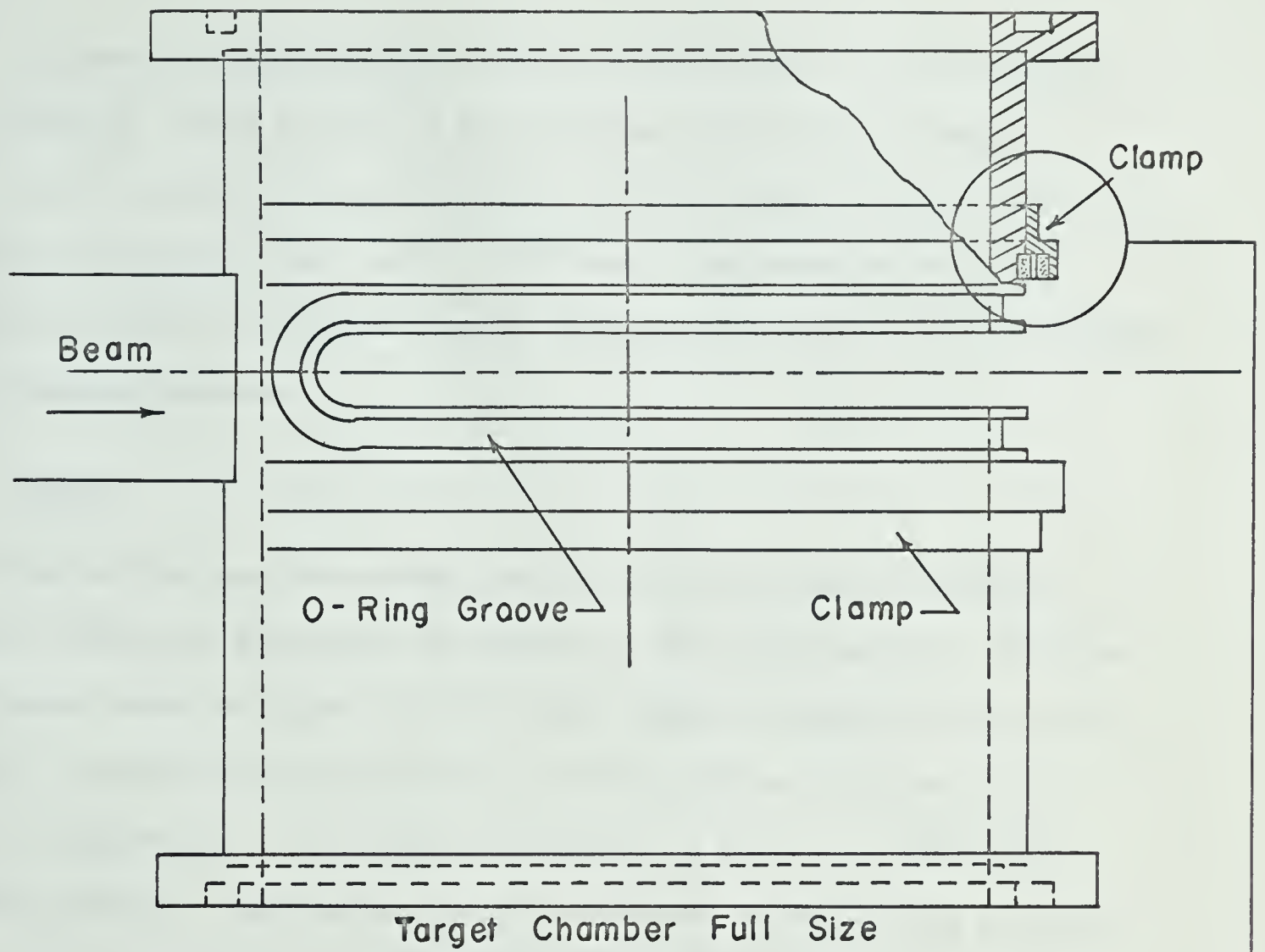


FIGURE 3-2 Target Chamber & Coupling to Lens

The beam is collimated to a 1.6 mm. diameter spot on the target by a collimation system located at the entrance to the target chamber. This system consists of two .020" tantalum discs separated by 20 cms. along the beam tube, each with a 1/16" hole. The tantalum has been coated with zinc sulphide so that the beam may be viewed at the collimators for alignment purposes.

(e) Targets

Most of the experiments described in the following two chapters involve Rutherford scattering on targets of gold and aluminum. The first experiments were performed with thin gold targets evaporated onto formvar films. The remaining experiments, involving gold and aluminum, were made by evaporating a thin layer of gold onto a thin, self supporting, aluminum target. The aluminum targets were made by evaporating aluminum onto glass slides previously coated with detergent (Teepol). The aluminum was then floated off in luke warm water and picked up with aluminum target blanks.

Target thicknesses were estimated by observing the energy loss of the 5.41 MeV alpha particles from Am^{241} . The thickest target observed (gold on aluminum) was only $20 \text{ keV} \pm 5 \text{ keV}$, or about 5 keV thick to protons of 1 MeV. At a kicksorter sensitivity of 13 keV per channel no alpha particle energy loss could be observed in the gold on formvar targets. The targets, therefore, were deemed thin enough, in view of other uncertainties, that no energy correction was made for their thickness.

(f) The Detector and Step Wedge

At the focal plane of the system a solid state detector (Nuclear Diodes PL2 35 10 #329*) was mounted in such a way as to allow its movement parallel to the focal plane and/or parallel to the 90° exit ray. (See figure 3-3.) The detector is used in conjunction with an Ortec system preamplifier and amplifier (Models #101 and 201 respectively**).

Even for spectrometer applications, it is desirable to have some position definition of the image at the detector. This could be accomplished by using an array of solid-state detectors at the image, involving a rather formidable electronic arrangement (Alexander) or with a position sensitive detector. The former method was the one originally intended at this laboratory; the latter is the method planned for the future.

In these experiments a technique considerably simpler in principle was used. In front of the 10 mm. diameter detector was placed an 8 mm. square step wedge. (See figure 3-4.) Different step wedges were used for various particles and energy ranges. The step wedge is divided into four 2 mm. x 8 mm. strips, each strip or "step" being from 100 - 500 keV thicker than its neighbour to the particles under observation. The three steps (for the fourth one is of zero thickness) were made of nickel foil or aluminized mylar, held onto brass frames with Scotch Tape. Care was taken that the area of each step was the same, and that the entire wedge was mounted centrally over the detector.

*Nuclear Diodes, Highland Park, Illinois.

**Oak Ridge Technical Enterprises Corp., Oak Ridge, Tennessee.

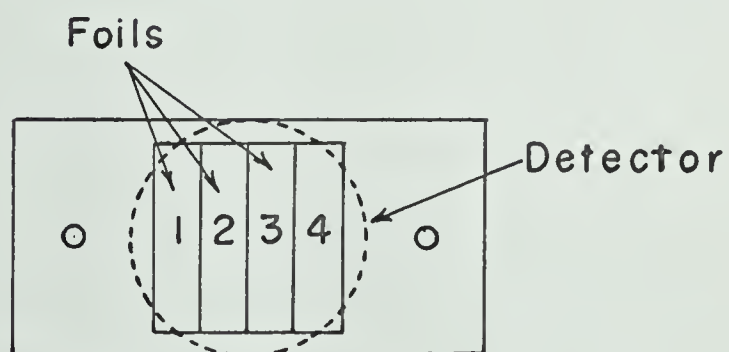
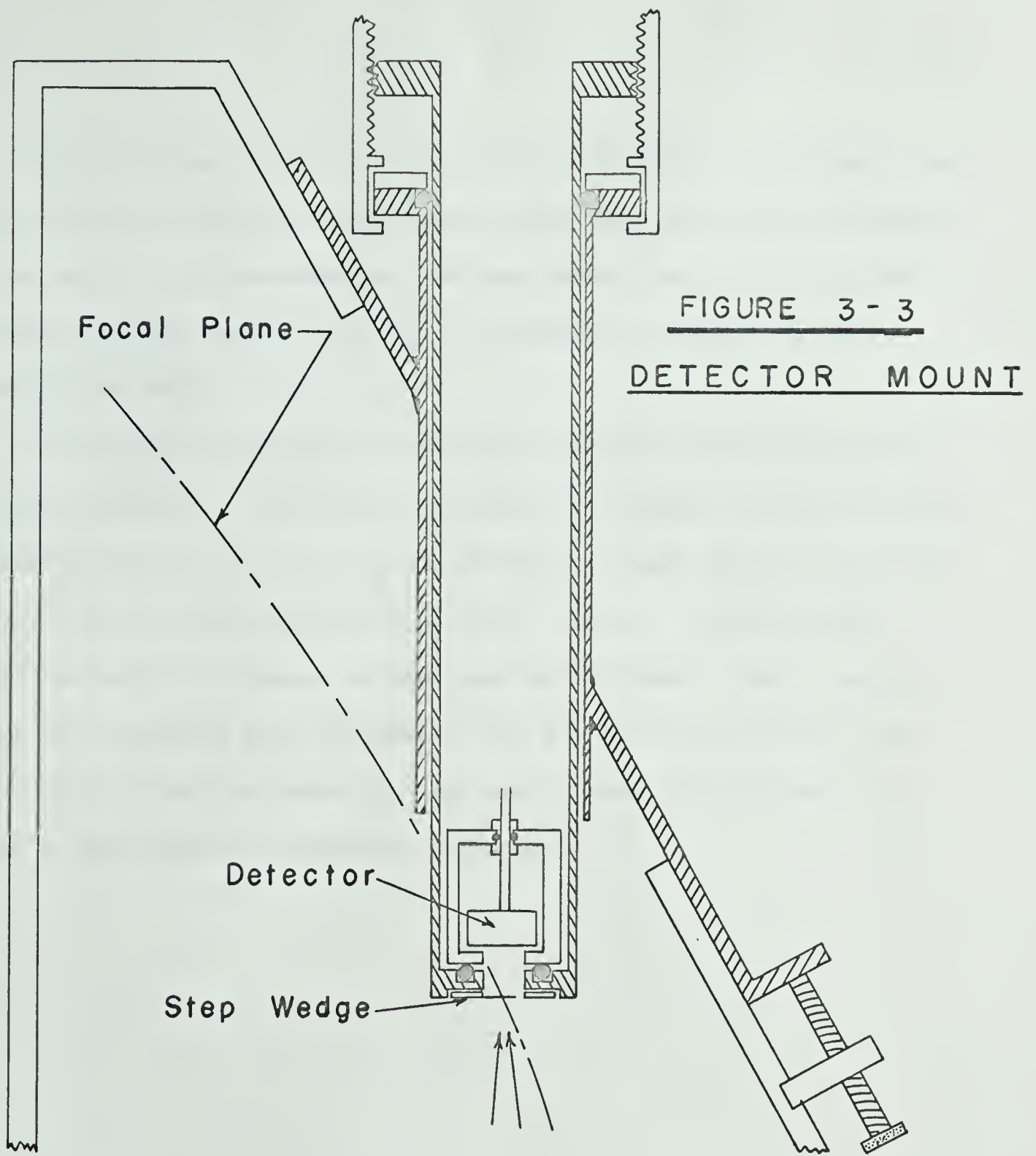


FIGURE 3 - 4 STEP WEDGE

This technique proved to be entirely satisfactory. Each wedge was found to be useful over a wider energy range than had been anticipated, and so very little inconvenience was experienced due to the fact that the entire system had to be let up to atmospheric pressure in order to change the wedge.

The position resolution, of course, is rather crude by comparison with other methods. (Photographic plates, for example have been scanned by Browne (Browne, 1956) in 1/4 mm. strips, or eight strips to our one.) However, in view of our large object size (1.6 mm.), and the unit magnification of the system in the spectrograph mode, steps 2 mm. wide cannot be considered much too great. The position resolution of the system will be much improved with the anticipated acquisition of a 10 mm. x 10mm. position sensitive detector.

CHAPTER 4: THE SPECTROGRAPH

(a) Location of the Focal Plane

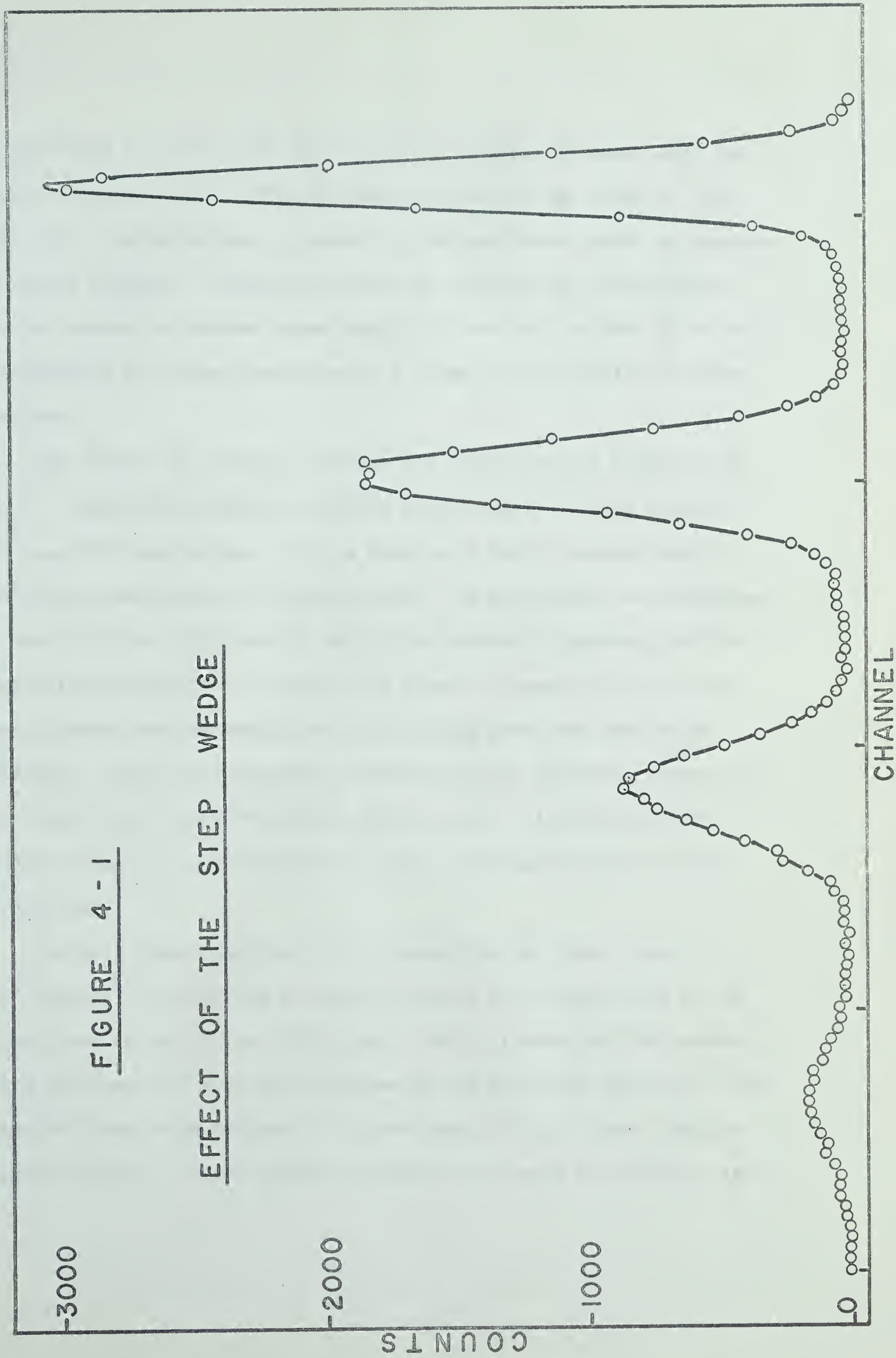
Particles deflected by the spectrometer were first observed on October 30, 1965. These were protons elastically scattered from a 10 microinches nickel foil and, for historical interest if nothing else, this first spectrum is shown in figure 4-1. The four peaks are due to the four steps of the step wedge described earlier.

The beam spot on the target was 1.6 mm. in diameter and the magnification of the system, in theory at least, is unity, so the image at the focal plane should be expected to fit almost entirely into one of the 2 mm. wide steps of the wedge. The problem of finding the focal plane, then, reduces to that of finding the position of the wedge where the maximum number of counts are focussed into one step.

Several such searches were carried out during the course of these experiments, for the image of elastic scattering from targets of nickel, aluminum and gold, both with and without the quadrupole lens, and for various assemblies used to hold the detector and wedge. These searches, in general, were not very satisfactory. The maxima observed were very broad, usually with no statistically significant change in the percentage of counts in the third step over a range of 2 - 3 centimeters. This is not entirely unexpected because of the small angle of the particle

FIGURE 4 - 1

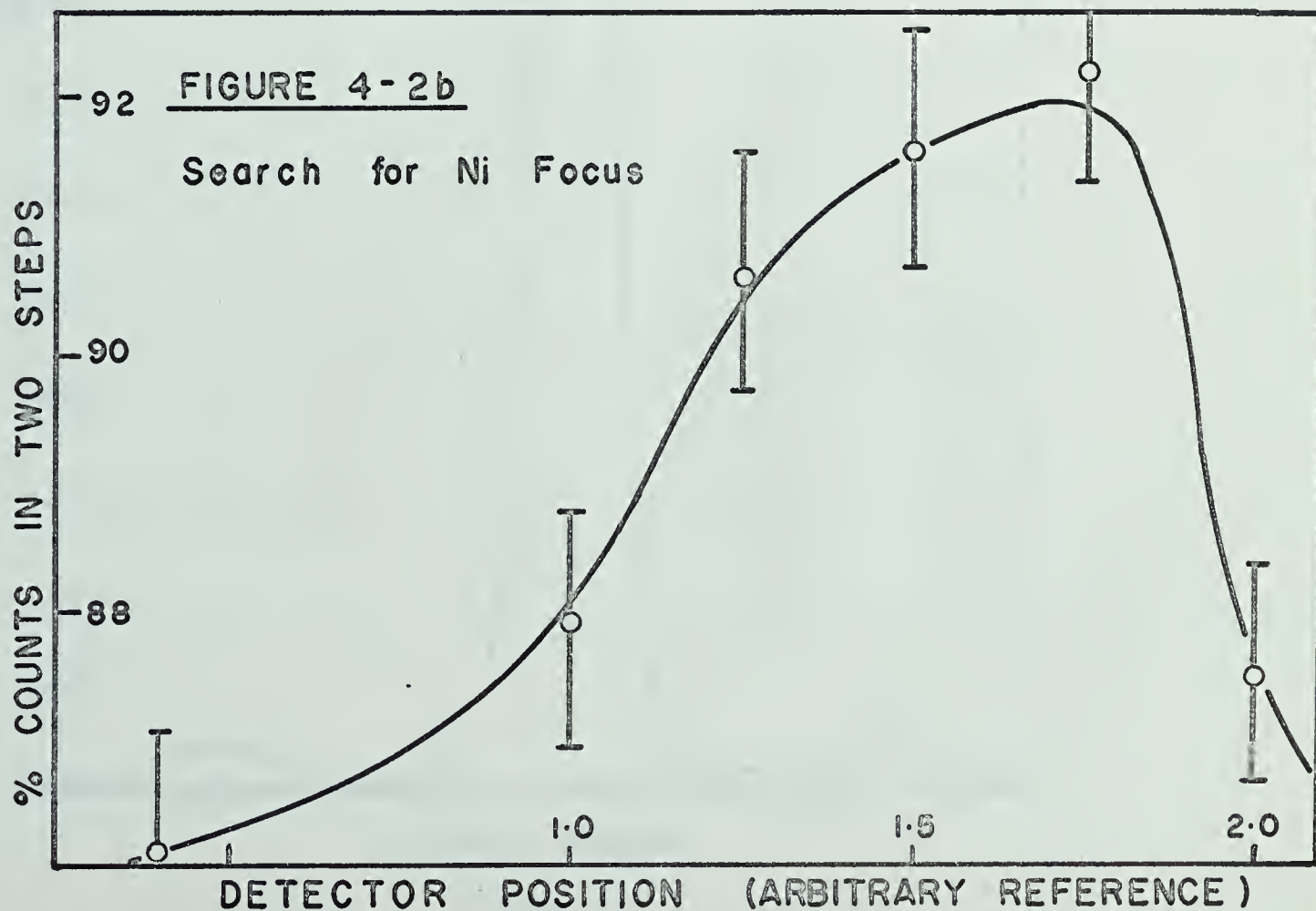
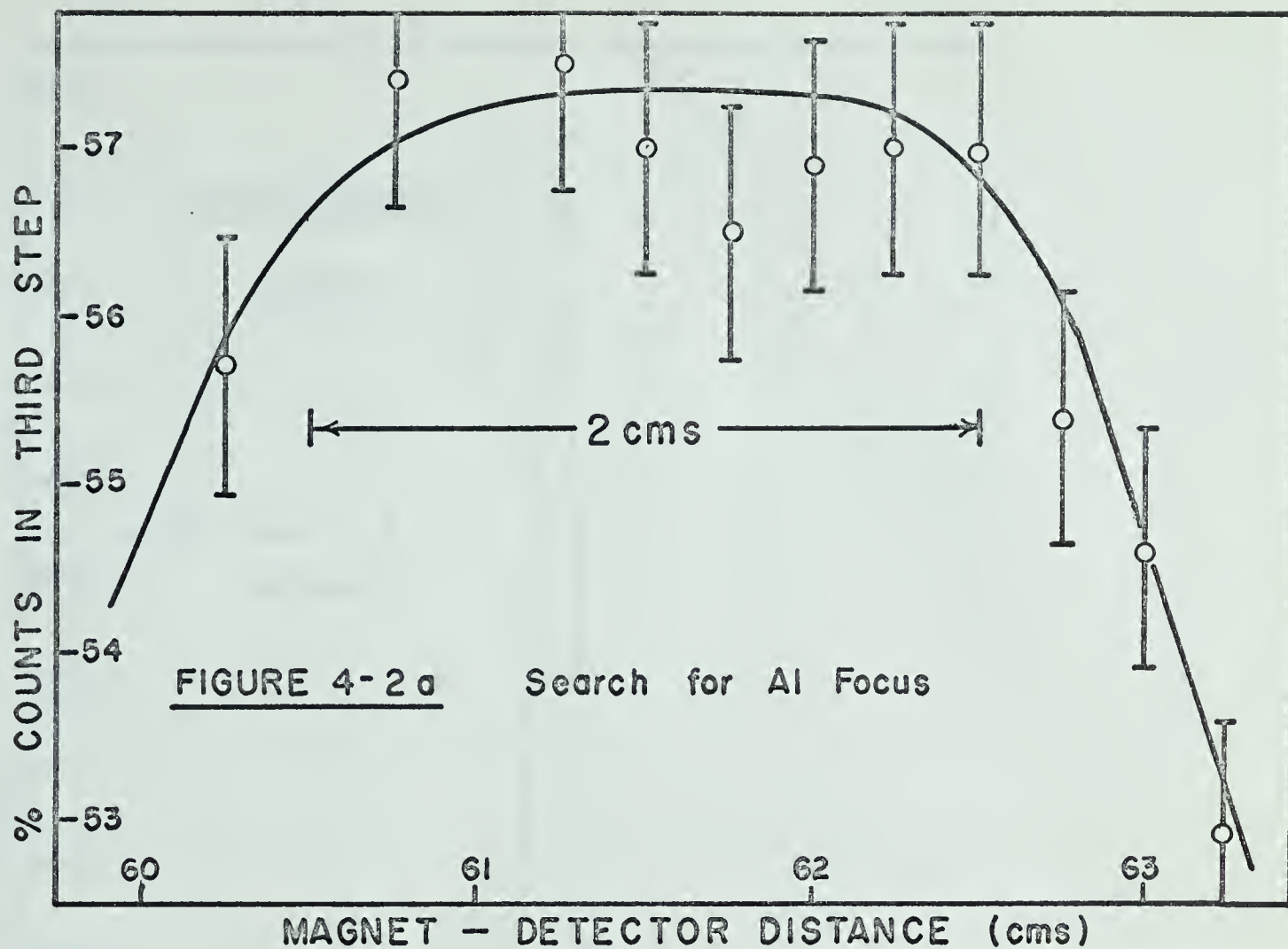
EFFECT OF THE STEP WEDGE



trajectories ($\sim 2-1/2^\circ$), and the fact that the step is larger than the theoretical image size. This accounts for an inherent range of 1 cm. over which the percentage of counts in the third step should be expected to remain constant. Kinematic effects and statistical uncertainties can be expected to broaden this range still further, so that it is not unreasonable to estimate an error of ± 2 cms. on the results of these searches.

The results of two such searches are illustrated in figures 4-2a and b. Figure 4-2a shows the results of the search for the focus of $\text{Al}^{27}(\text{p},\text{p})\text{Al}^{27}$ scattering. This is shown as a fairly typical result, the plateau being about 2.25 cms. broad. The relatively low percentage of counts in the third step is due to the kinematic broadening of the image discussed earlier. Figure 4-2b shows the results of the first search, where the percentage of counts in two steps was used as an indicator. Here again kinematic broadening is an important factor, as the target was a relatively thick nickel foil. This case, though not really typical, is shown because it gives a far more positive focus indication.

The best focus resulting from a search for the focal plane of $\text{Au}^{197}(\text{p},\text{p})\text{Au}^{197}$ scattering is shown in figure 4-3, where 92.6% of the counts have fallen in the third step. This is typical of the spectra which were used for the work described in the following sections. This focus was found at a distance of approximately 57.2 ± 2 cms. from the magnet pole tips. If we assume the detector to be on the 90° ray, and



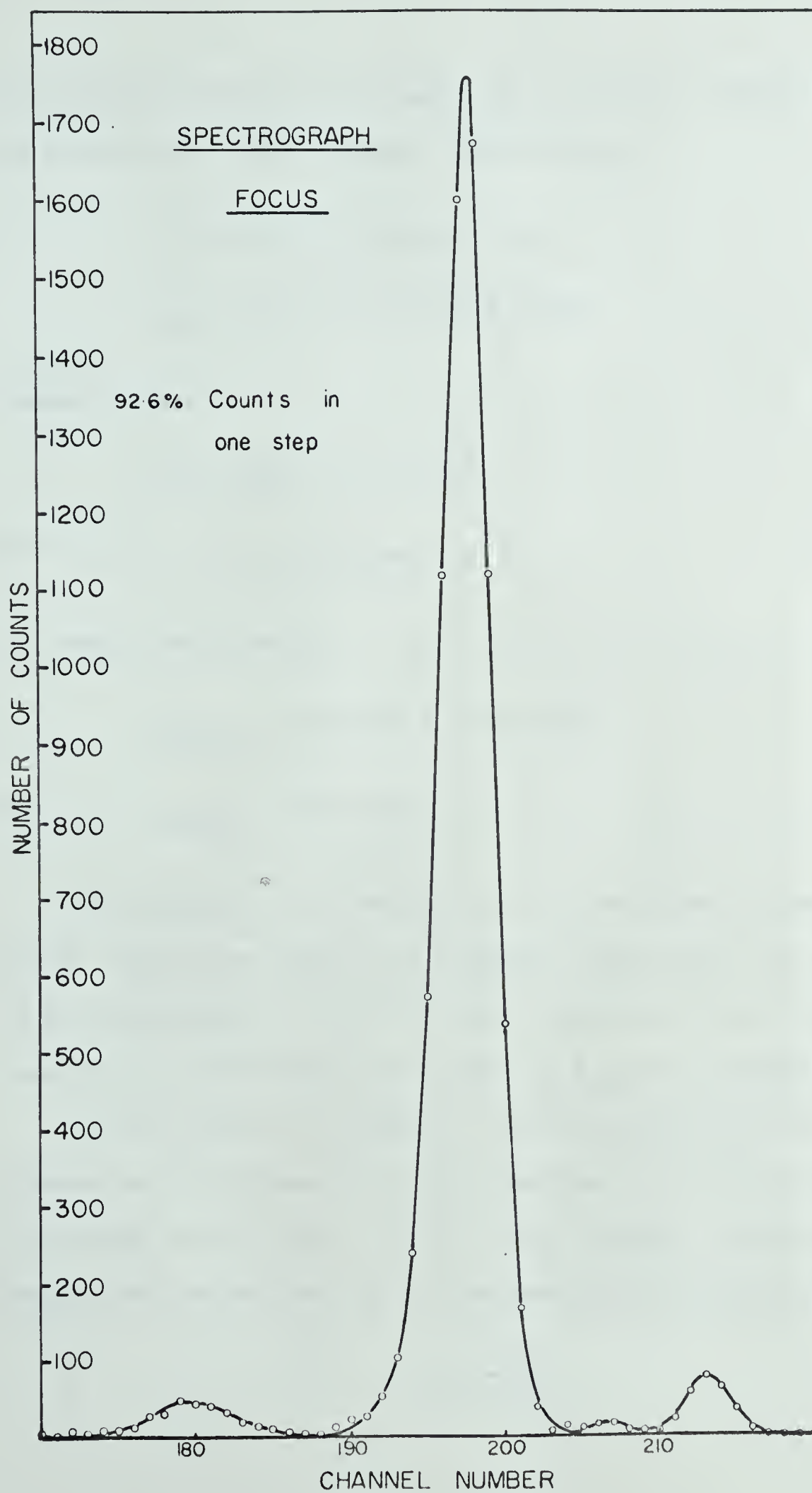


FIGURE 4-3

the effective radius of the magnet to be 52 cms., (assumptions which will be justified in later sections) then we have:

$$\ell_2 = 57.2 - 2 = 55.2 \pm 2 \text{ cms.}$$

$$q_{\text{exp}} = 50 + 57.2 = 107.2 \pm 2 \text{ cms.}$$

However, since

$$\ell_1 \ell_2 = R_{\text{eff}}^2 = 270.4 \text{ cm}^2$$

and

$$\ell_1 = 50.5 \text{ cms.}$$

We should have expected

$$\ell_{2\text{theory}} = 270.4/50.5 = 53.5 \text{ cms.}$$

and

$$q_{\text{theory}} = 105.5 \text{ cms.}$$

The agreement is not as good as might be hoped, although the experimental result does include the predicted value within the estimated range of its uncertainty. It will be noted later that there is also some experimental uncertainty in the value of R_{eff} used in this calculation.

We have observed in Chapter 2 that the position of the focal plane depends upon the kinematics of the reaction, or, in the case of elastic scattering, on the mass, A , of the target nucleus. We should, therefore, expect the aluminum focus to be displaced from the gold focus by an amount

$$D = \frac{R_0}{\ell_1} \times \frac{\ell_1 + R_0}{1 - \ell_1/aR_0}$$

where

$$a = \frac{1}{r} \frac{\Delta r}{\Delta \theta} = \frac{A \sin \theta}{1 - A \cos \theta}$$

and

$$A = (M_I M_E E_I / E_{E0})^{1/2} / (M_R + M_E)$$

For $Al^{27}(p,p)Al^{27}$ we have

$$A \sim 1/28 = 3.6 \times 10^{-2}$$

from which $a \sim 3.2 \times 10^{-2}$ at $\theta = 60^\circ$.

Substituting $\ell_1 = 50.5$ cms. and $R_0 = 52$ cms. we find

$$D \approx 3.6 \text{ cms.}$$

Referring to figure 4-2a we see how difficult it is to determine precisely the position of the aluminum focus. However, the highest percentage of counts in the third step occurs at about 61 cms. from the magnet pole tips, corresponding to a displacement of about 3.8 cms. from the gold focus noted above.

The use of a position sensitive detector, which will give a better picture of the image at any point, will undoubtedly facilitate the location of focal planes. The precise location of the focal plane is not, however, extremely critical for spectrometer applications. The resolution will not be much affected over a range of a centimeter or two in the vicinity of the true focus.

(b) Determining the Reaction Angle

Although a large protractor with a vernier were provided with the spectrometer, so that the angle of the system relative to the beam could be measured with great accuracy, no simple means was provided for finding the zero angle of the system. A single port provided with cross-hairs, or a pin, or mark suitably located in the vacuum chamber, would have allowed the system to be aligned optically, and the vernier and protractor set with relative ease.

The same may be said of the location of the 90° ray at the magnet exit flange, which could easily have been marked by the manufacturer. This, as will appear evident later, would also have greatly simplified matters, eliminating the need for several changes in the position of the detector and wedge.

As it was, a method had to be devised to measure the angle at which the system was oriented relative to the beam. The problem was further complicated by the fact that, due to vacuum difficulties in the target chamber (Appendix B) we were restricted to an angular range of about 30° on the right side of the beam.

It was decided to make use of the $\text{cosec}^4 \theta/2$ dependence of the Rutherford scattering cross-section. The protractor was set as close to the correct angle as was possible by eye, the estimated error being about $\pm 5^\circ$. The system was then set, nominally, at 45° , 55° , and 65° , positions where vacuum difficulties were minimal. At each of these angles, the total number of protons scattered into the system and focussed on the

detector, for a fixed integrated incident current, was counted at various energies. The integrated current was selected so as to give total number of counts which would have statistical errors of less than 1%, a criterion determined by the rate of variation of $\text{cosec}^4 \theta/2$ in this region. The current integrator was carefully calibrated and checked for leakage current with a battery and electrometer before each series of runs, and the electron suppressor in front of the Faraday cup biased at -800 volts. The statistical consistency of the runs was constantly checked.

The results of these measurements are tabulated in Table 4-1. The column labelled "Result" is the average number of counts normalized to an integrated incident current of 6×10^{-6} coulombs, with its statistical error expressed both absolutely and as a percentage. The average lengths of these runs was 2 or 3 minutes.

Table 4-2 shows the first analysis of the data, where the ratios $\bar{N}_{\theta_1}/\bar{N}_{\theta_2}$ have been calculated at each energy for each pair of angles. Finally, the average of these ratios for all energies has been calculated.

The angle can now be determined by comparing these ratios with ratios of $\text{cosec}^4 \theta_1/2 \div \text{cosec}^4 \theta_2/2$. This has been done in figure 4-4, where short sections of the function $\text{cosec}^4 \theta_1/2 \div \text{cosec}^4 \theta_2/2$ have been drawn for values of θ in the vicinity of the nominal values indicated on the figure. The three ratios experimentally determined above have been located on these three curves, and appear with their (vertical) error bars. These points give three determinations of the correct angle, with error bars found by projecting the statistical (vertical) error bars along

TABLE 4-1

| Run | Nominal L | E_0 (MeV) | ΔQ (Coulombs) | $N = \sum p$ | \bar{N} | $\sigma = \sqrt{\bar{N}}/\sqrt{n}$ | Result |
|-----|--------------|-------------|-----------------------------|--------------|-----------|------------------------------------|--------------------------|
| 3 | 45° | 3.0 | 60 x 10 x 10 ⁻⁸ | 18,433 | 18,540 | 79 | 18,540 \pm 79 .43% |
| 4 | 45° | 3.0 | 60 x 10 x 10 ⁻⁸ | 18,597 | | | |
| 5 | 45° | 3.0 | 60 x 10 x 10 ⁻⁸ | 18,589 | | | |
| 12 | 45° | 3.5 | 60 x 10 x 10 ⁻⁸ | 13,654 | 13,603 | 67 | 13,603 \pm 67 .49% |
| 13 | 45° | 3.5 | 60 x 10 x 10 ⁻⁸ | 13,527 | | | |
| 16 | 45° | 3.5 | 60 x 10 x 10 ⁻⁸ | 13,629 | | | |
| 19 | 45° | 4.5 | 90 x 10 x 10 ⁻⁸ | 13,018 | 12,936 | 62 | 8,630 \pm 41 .48% |
| 20 | 45° | 4.5 | 90 x 10 x 10 ⁻⁸ | 12,950 | | | |
| 21 | 45° | 4.5 | 60 x 10 x 10 ⁻⁸ | 8,560 | | | |
| 22 | 45° | 2.5 | 60 x 10 x 10 ⁻⁸ | 27,494 | 27,508 | 117 | 27,508 \pm 117 .43% |
| 22a | 45° | 2.5 | 60 x 10 x 10 ⁻⁸ | 27,523 | | | |
| 24 | 65° | 3.0 | 120 x 10 x 10 ⁻⁸ | 10,783 | 10,870 | 60 | 5,435 \pm 30 .55% |
| 25 | 65° | 3.0 | 120 x 10 x 10 ⁻⁸ | 10,996 | | | |
| 26 | 65° | 3.0 | 120 x 10 x 10 ⁻⁸ | 10,830 | | | |
| 28 | 65° | 3.5 | 150 x 10 x 10 ⁻⁸ | 10,020 | 10,096 | 58 | 4,040 \pm 23 .57% |
| 29 | 65° | 3.5 | 150 x 10 x 10 ⁻⁸ | 10,055 | | | |
| 30 | 65° | 3.5 | 150 x 10 x 10 ⁻⁸ | 10,213 | | | |
| 31 | 65° | 4.0 | 200 x 10 x 10 ⁻⁸ | 10,255 | 10,356 | 59 | 3,105 \pm 18 .58% |
| 32 | 65° | 4.0 | 200 x 10 x 10 ⁻⁸ | 10,373 | | | |
| 33 | 65° | 4.0 | 200 x 10 x 10 ⁻⁸ | 10,439 | | | |
| 34 | 65° | 4.5 | 200 x 10 x 10 ⁻⁸ | 8,278 | 10,213 | 56 | 2,454 \pm 13 .53% |
| 35 | 65° | 4.5 | 250 x 10 x 10 ⁻⁸ | 10,183 | | | |
| 36 | 65° | 4.5 | 250 x 10 x 10 ⁻⁸ | 10,105 | | | |
| 37 | 55° | 3.0 | 60 x 10 x 10 ⁻⁸ | 9,201 | 18,564 | 72 | 9,282 \pm 36 .39% |
| 38 | 55° | 3.0 | 120 x 10 x 10 ⁻⁸ | 18,426 | | | |
| 39 | 55° | 3.0 | 120 x 10 x 10 ⁻⁸ | 18,864 | | | |
| 48 | 55° | 3.5 | 120 x 10 x 10 ⁻⁸ | 13,888 | 13,979 | 68 | 6,989 \pm 34 .49% |
| 49 | 55° | 3.5 | 120 x 10 x 10 ⁻⁸ | 14,081 | | | |
| 50 | 55° | 3.5 | 120 x 10 x 10 ⁻⁸ | 13,968 | | | |
| 59 | 55° | 4.0 | 120 x 10 x 10 ⁻⁸ | 10,616 | 10,614 | 60 | 5,307 \pm 30 .56% |
| 60 | 55° | 4.0 | 120 x 10 x 10 ⁻⁸ | 10,519 | | | |
| 61 | 55° | 4.0 | 120 x 10 x 10 ⁻⁸ | 10,707 | | | |
| 62 | 55° | 2.5 | 60 x 10 x 10 ⁻⁸ | 13,640 | 13,703 | 68 | 13,703 \pm 68 .49% |
| 63 | 55° | 2.5 | 60 x 10 x 10 ⁻⁸ | 13,720 | | | |
| 64 | 55° | 2.5 | 60 x 10 x 10 ⁻⁸ | 13,750 | | | |

TABLE 4-2

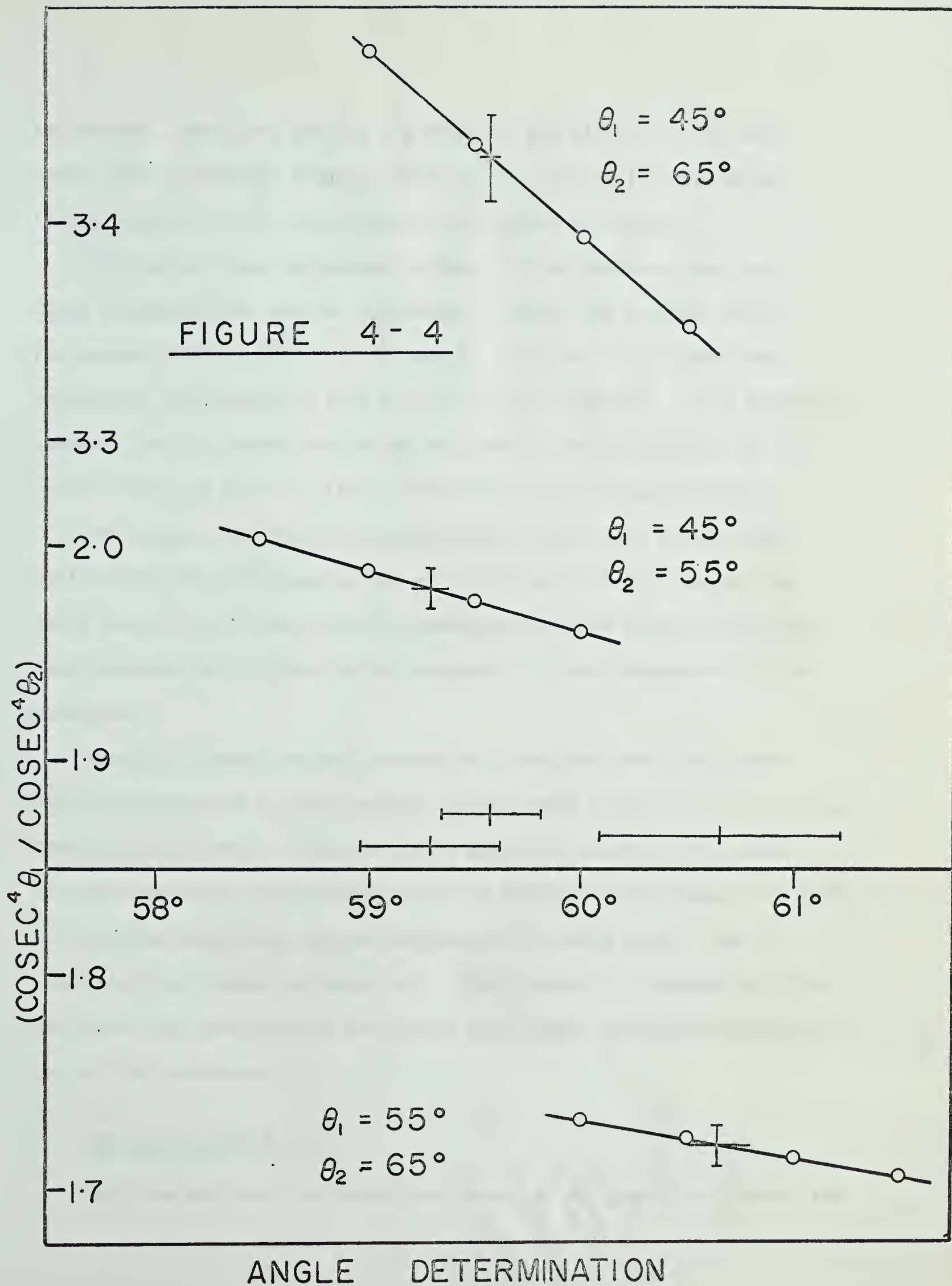
| E_0 | θ_1 | θ_2 | $\overline{N_{\theta_1}}/\overline{N_{\theta_2}}$ |
|-------|------------|------------|---------------------------------------------------|
| 2.5 | 45° | 55° | 2.00 ₅ \pm 0.02 |
| 3.0 | 45° | 55° | 1.99 ₈ \pm 0.02 |
| 3.0 | 45° | 65° | 3.42 \pm 0.03 |
| 3.0 | 55° | 65° | 1.71 \pm 0.02 |
| 4.0 | 55° | 65° | 1.71 \pm 0.02 |
| 3.5 | 45° | 55° | 1.95 \pm 0.02 |
| 3.5 | 45° | 65° | 3.37 \pm 0.03 |
| 3.5 | 55° | 65° | 1.73 \pm 0.02 |
| 4.5 | 45° | 65° | 3.51 \pm 0.04 |

Averaging these values, we get:

$$\overline{N_{45}}/\overline{N_{55}} = 1.98 \pm 0.01$$

$$\overline{N_{55}}/\overline{N_{65}} = 1.72 \pm 0.01$$

$$\overline{N_{45}}/\overline{N_{65}} = 3.43 \pm 0.02$$



the curves. The three results are found to lie within 1.3° of each other, with an average value of $59.8^\circ \pm .2^\circ$. With this information it was possible to set the protractor to within $1/2$ degree.

Two further comments should be made. It is apparent that the three determinations are not independent, since, for example, once the ratios for $\theta_1 = 45^\circ$, $\theta_2 = 55^\circ$ and $\theta_1 = 55^\circ$, $\theta_2 = 65^\circ$ have been determined, the ratio for $\theta_1 = 45^\circ$, $\theta_2 = 65^\circ$ is implied. It is important, however, that all three results be included in the calculation of the mean, since this has the effect of minimizing any systematic error. If, for example, the magnet was positioned slightly off at 55° , then errors would be introduced in the $45^\circ - 55^\circ$ and $55^\circ - 65^\circ$ ratios that would tend to cancel each other, lessening the error which would result from ignoring one of these values because it is not independent of the other two.

Finally, although elastic scattering from gold should be almost entirely Rutherford at these angles, errors would result if, for example, there was a systematic change in solid angle with energy. To insure that the observed cross-sections were due entirely to the $\text{cosec}^4 \theta/2$ term, the counting rates were plotted against $1/E^2$ at each angle. Two of these plots are shown in figure 4-5. Their linearity, combined with the fact that they pass through the origin (not shown) further justifies the use of this technique.

(c) The Calibration Curve

With the angle of the system now known, it was possible to begin the

RUTHERFORD SCATTERING ON GOLD

THOUSANDS OF COUNTS

45°

65°

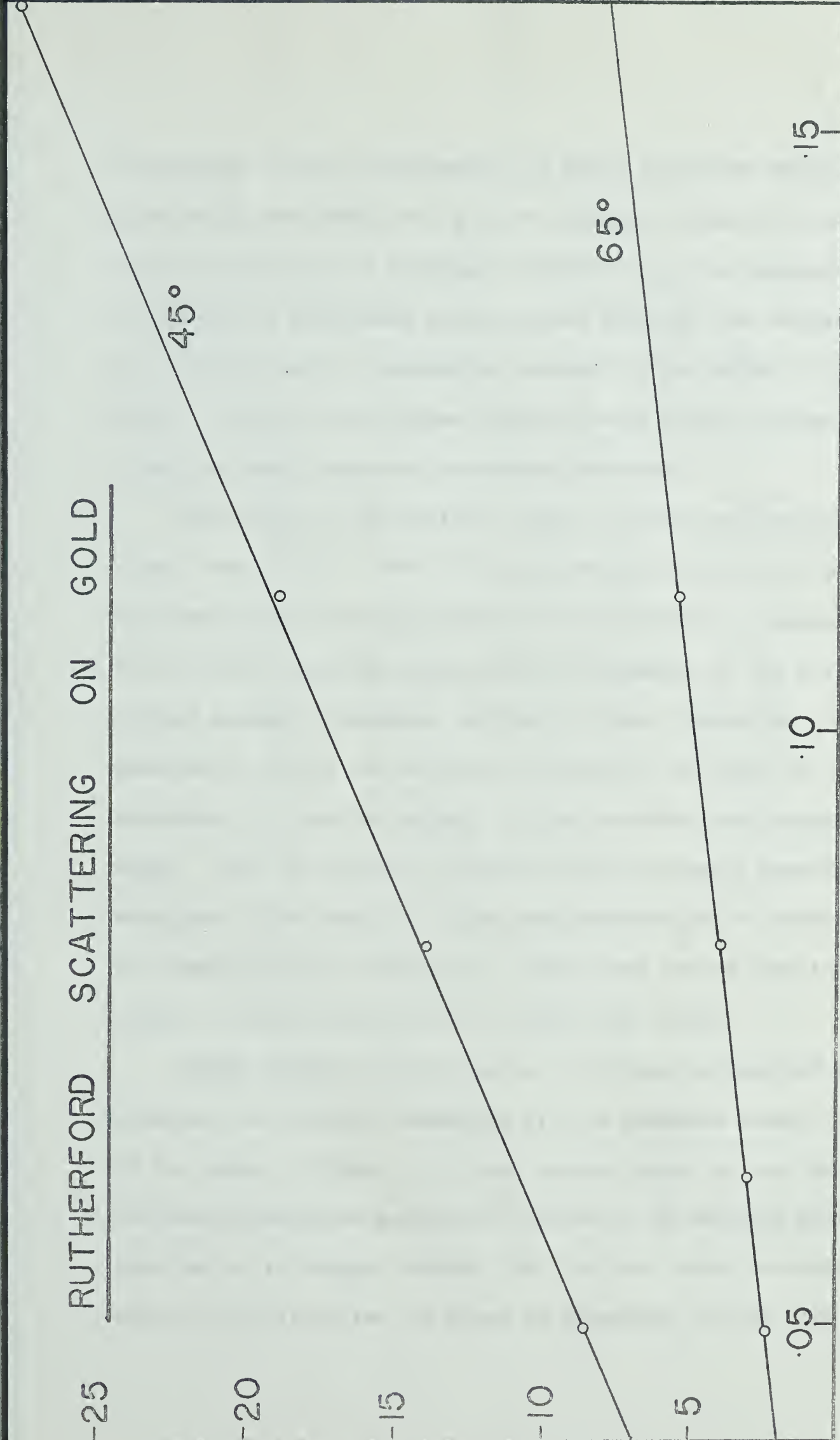
.05

.10

.15

(1/E²) IN MEV⁻²

FIGURE 4-5



calibration of the spectrometer, by using the known energies of particles elastically scattered from gold or aluminum. Since the manufacturer had not indicated the position of the 90° ray, the detector was placed at a position determined by an optical guess at the location of that ray, combined with a reasonable estimate of the effect of the fringing field. As will later become apparent, this choice of detector position along the focal plane was extremely fortunate.

The energy of the incident beam of protons was varied in 100 keV steps from 2.5 to 5.3 MeV. This was repeated with a deuteron beam. At each energy the scattered particles were carefully focused into the third step of the step wedge, and the frequency of the corresponding nuclear magnetic resonance recorded. These frequencies could easily be measured to within one or two kilocycles in the range 20 - 35 Mc/s by observing the relative heights of the two side peaks produced by the wedge. Thus the relative accuracy of the frequency measurements was very good. The results of this gold calibration are shown in Table 4-3, and then plotted in figure 4-6. This curve can be used to set the magnet to focus particles of any specified energy.

Taking somewhat fewer points, the entire calibration was repeated observing the elastic scattering from an aluminum target (Table 4-4). On the scale of figure 4-6, these points appear to fall very close to the gold calibration curve, but plotted on an expanded scale, figures 4-7a and b, it becomes evident that the two curves are separated by as much as 100 kilocycles, or about 50 kilovolts, at the high energy end.

TABLE 4-3

Gold Target

| E ₀ (MeV) | Protons | | Deuterons | | |
|-------------------------|----------------|-----------|----------------|-----------------|-----------|
| | E ₃ | Frequency | E ₃ | 2E ₃ | Frequency |
| 2.5 | 2.487 | 18.635 | 2.475 | 4.950 | 26.240 |
| 2.6 | 2.587 | 18.986 | 2.574 | 5.148 | 26.750 |
| 2.7 | 2.686 | 19.349 | 2.673 | 5.346 | |
| 2.8 | 2.786 | 19.708 | 2.772 | 5.544 | 27.794 |
| 2.9 | 2.885 | 20.058 | 2.871 | 5.742 | 28.290 |
| 3.0 | 2.985 | 20.404 | 2.970 | 5.940 | 28.775 |
| 3.1 | 3.084 | 20.745 | 3.068 | 6.136 | 29.251 |
| 3.2 | 3.184 | 21.074 | 3.167 | 6.334 | 29.716 |
| 3.3 | 3.283 | 21.402 | 3.266 | 6.532 | 30.176 |
| 3.4 | 3.383 | 21.765 | 3.365 | 6.730 | 30.641 |
| 3.5 | 3.482 | 22.045 | 3.464 | 6.928 | 31.084 |
| 3.6 | 3.582 | 22.358 | 3.563 | 7.126 | 31.526 |
| 3.7 | 3.681 | 22.655 | 3.662 | 7.324 | 31.975 |
| 3.8 | 3.781 | 22.960 | 3.761 | 7.522 | 32.389 |
| 3.9 | 3.880 | 23.268 | 3.860 | 7.720 | 32.814 |
| 4.0 | 3.980 | 23.562 | 3.959 | 7.918 | 33.242 |
| 4.1 | 4.079 | 23.860 | 4.058 | 8.116 | 33.665 |
| 4.2 | 4.179 | 24.150 | 4.157 | 8.314 | 34.068 |
| 4.3 | 4.278 | 24.430 | 4.256 | 8.512 | 34.382 |
| 4.4 | 4.378 | 24.720 | 4.355 | 8.710 | 34.890 |
| 4.5 | 4.477 | 25.002 | 4.454 | 8.908 | 35.273 |
| 4.6 | 4.577 | 25.273 | 4.553 | 9.106 | 35.644 |
| 4.7 | 4.676 | 25.543 | 4.652 | 9.304 | 36.045 |
| 4.8 | 4.775 | 25.810 | 4.751 | 9.502 | 36.427 |
| 4.9 | 4.875 | 26.078 | 4.850 | 9.700 | 36.797 |
| 5.0 | 4.974 | 26.340 | 4.949 | 9.898 | 37.165 |
| 5.1 | 5.074 | 26.605 | | | |
| 5.2 | 5.173 | 26.869 | | | |
| 5.3 | 5.273 | 27.123 | | | |

* These points fall slightly high in the plot against \sqrt{E} , explaining the apparent discontinuity in the Au dispersion curve.

TABLE 4-4

Aluminum Target

| E ₀ | | | | | |
|----------------|----------------|-----------|----------------|-----------------|-----------|
| Protons | | | Deuterons | | |
| (MeV) | E ₃ | Frequency | E ₃ | 2E ₃ | Frequency |
| 2.5 | 2.408 | 18.378 | | | |
| 2.6 | 2.505 | 18.749 | | | |
| 2.7 | 2.601 | 19.105 | | | |
| 2.8 | 2.697 | 19.454 | 2.598 | 5.196 | 26.989 |
| 2.9 | 2.794 | 19.793 | | | |
| 3.0 | 2.890 | 20.135 | 2.784 | 5.568 | 27.950 |
| 3.1 | 2.986 | 20.465 | | | |
| 3.2 | 3.083 | | 2.969 | 5.938 | 28.866 |
| 3.3 | 3.179 | 21.122 | | | |
| 3.4 | 3.275 | 21.440 | 3.155 | 6.310 | 29.766 |
| 3.5 | 3.371 | 21.756 | | | |
| 3.6 | 3.468 | 22.065 | 3.341 | 6.682 | 30.649 |
| 3.7 | 3.564 | 22.373 | | | |
| 3.8 | 3.664 | 22.670 | 3.526 | 7.052 | 31.484 |
| 3.9 | 3.757 | 22.966 | | | |
| 4.0 | 3.853 | 23.264 | 3.712 | 7.424 | 32.315 |
| 4.1 | 3.949 | 23.545 | | | |
| 4.2 | 4.046 | 23.830 | 3.897 | 7.794 | 33.123 |
| 4.3 | 4.142 | 24.116 | | | |
| 4.4 | 4.238 | | 4.083 | 8.166 | 33.907 |
| 4.5 | 4.335 | 24.677 | | | |
| 4.6 | 4.431 | | 4.268 | 8.536 | 34.671 |
| 4.7 | 4.527 | 25.214 | | | |
| 4.8 | 4.624 | | 4.454 | 8.908 | 35.415 |
| 4.9 | 4.720 | | | | |
| 5.0 | 4.816 | 26.014 | 4.640 | 9.280 | 36.132 |

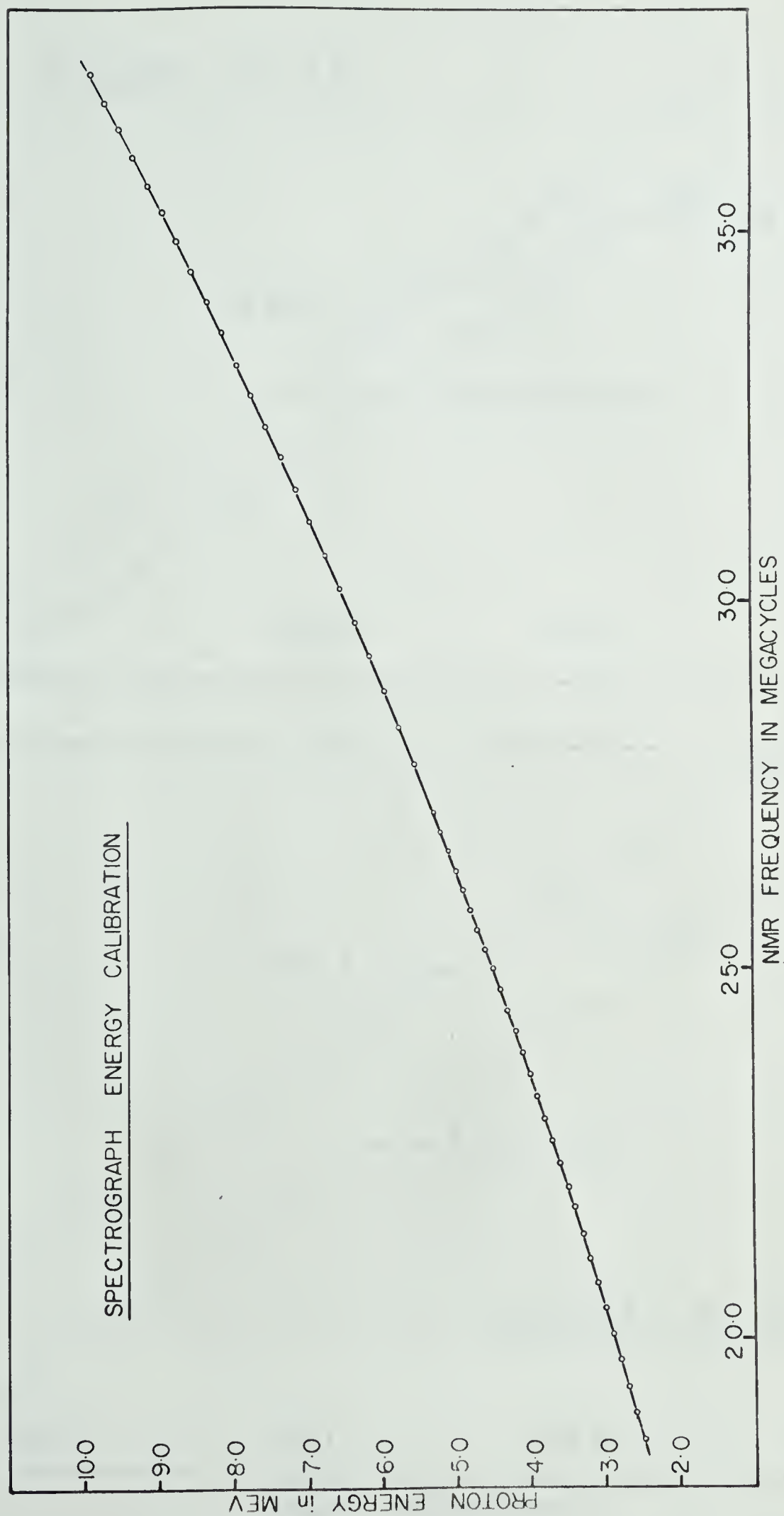
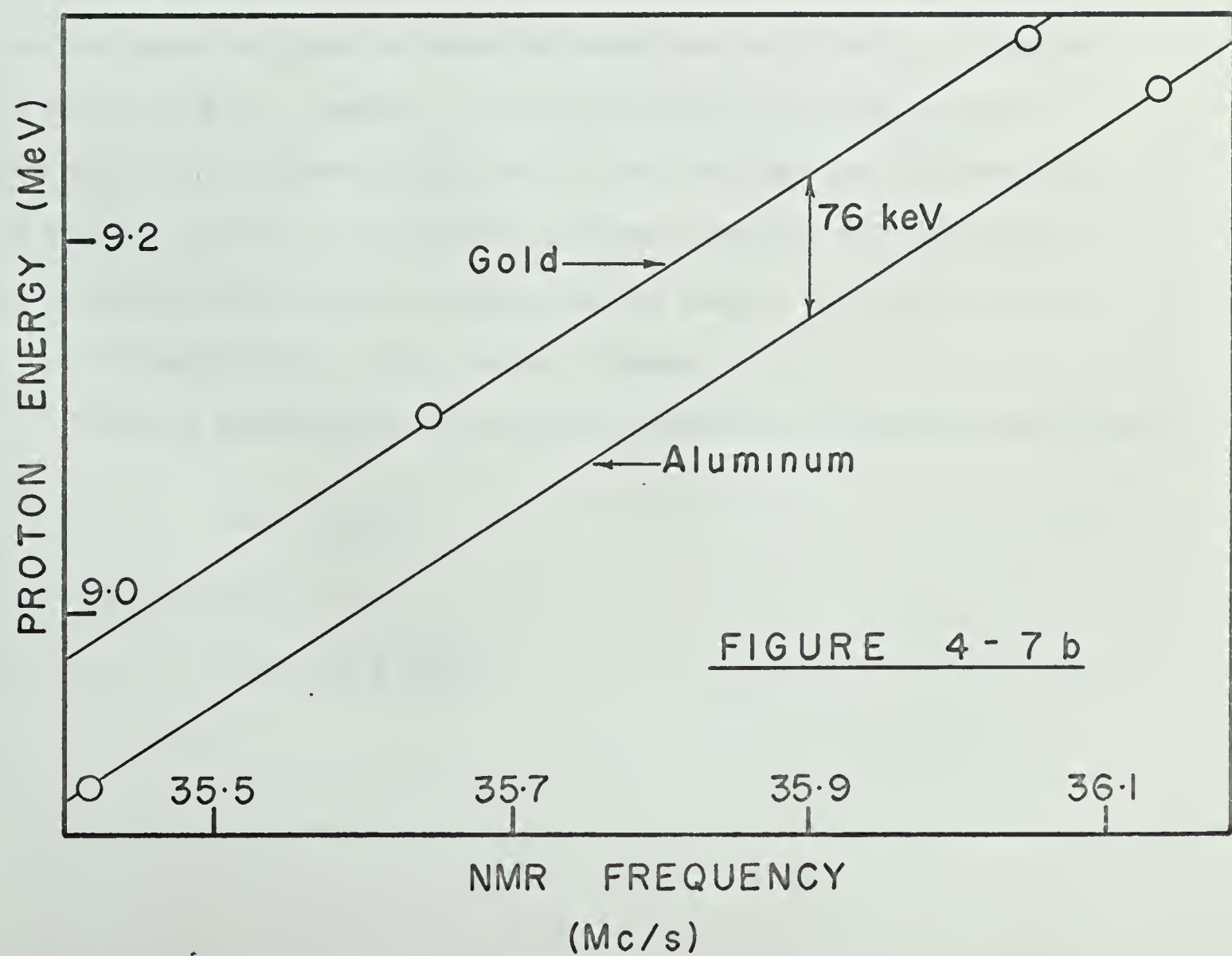
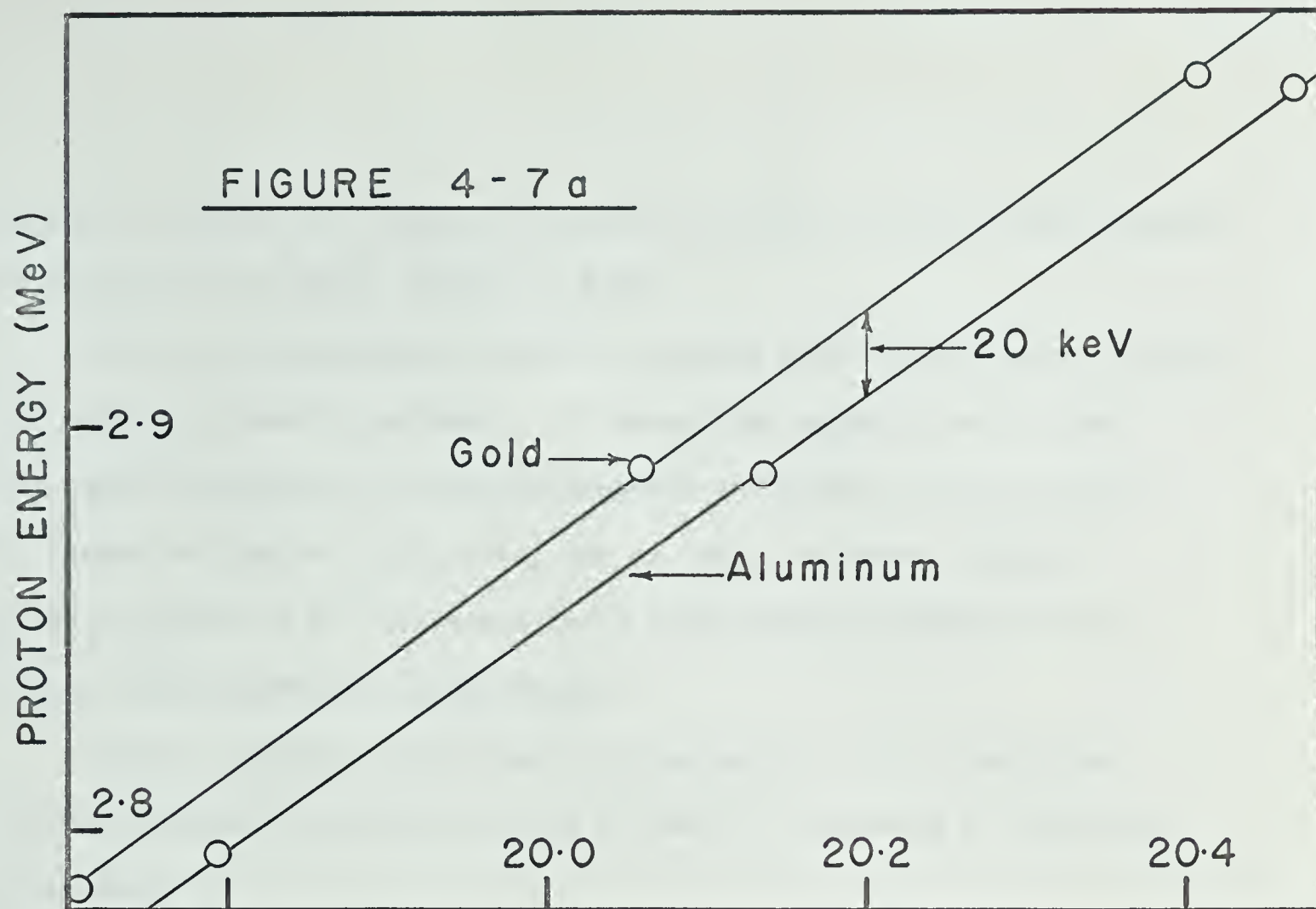


FIGURE 4-6



At lower energies the absolute separation is less, but still considerable, 65 kilocycles, or about 20 keV, at 3 MeV.

This is, unquestionably, the most serious problem which arose during the course of these experiments. It means that although for a given reaction the calibration curve is accurate to within a few kilocycles, it cannot be treated as absolute, and at least one known reference point will have to be determined for a given reaction before absolute energy measurements may be undertaken.

Several possible explanations were advanced for this unexpected and most undesirable observation, and these are discussed at some length in Appendix C.

Since the spectrometer is a momentum resolution device, the calibration points obtained as described above were replotted in figure 4-8 in the form \sqrt{E} vs. frequency. The linearity of this plot, as well as the fact that it passes through the origin, demonstrates that there is no systematic error in the assumed incident energies, and that there is no variation in the effective radius of the magnet, i.e. in the effect of the fringing field, over this field range.

Particle trajectories in the magnet have radii of curvature satisfying:

$$Bev = mv^2/r \quad (4-1)$$

or, in a more useful form:

$$Br = 143.9 \sqrt{m} \sqrt{E} \quad (4-2)$$

where

B is in kilogauss
r is in centimeters

and
m is in amu
E is in MeV

If F is the NMR frequency in megacycles, then

$$B = F/4.26$$

and we have

$$\sqrt{E} = \frac{r}{613\sqrt{m}} F \quad (4-3)$$

so that the slope of figure 4-8 is proportional to the radius of the particle trajectories. The measured slope of the curve is $0.0845 \text{ MeV}^{1/2}/\text{Mc}$, which gives, for $m = 1.008 \text{ amu}$:

$$r = 52.0 \text{ cms.}$$

Thus the calibration data also yields the radius of curvature of the particle trajectories in the magnet.

(d) The Dispersion Curve

In order to measure the actual spatial dispersion of the system, the NMR frequency at which elastically scattered protons from gold were focused into the third step of the wedge was measured at various positions along the focal plane for an incident proton energy of 3 MeV. The results are illustrated in figure 4-9. (An identical curve was obtained by observing protons scattered from an aluminum target.) The detector position is measured relative to an arbitrary reference position.

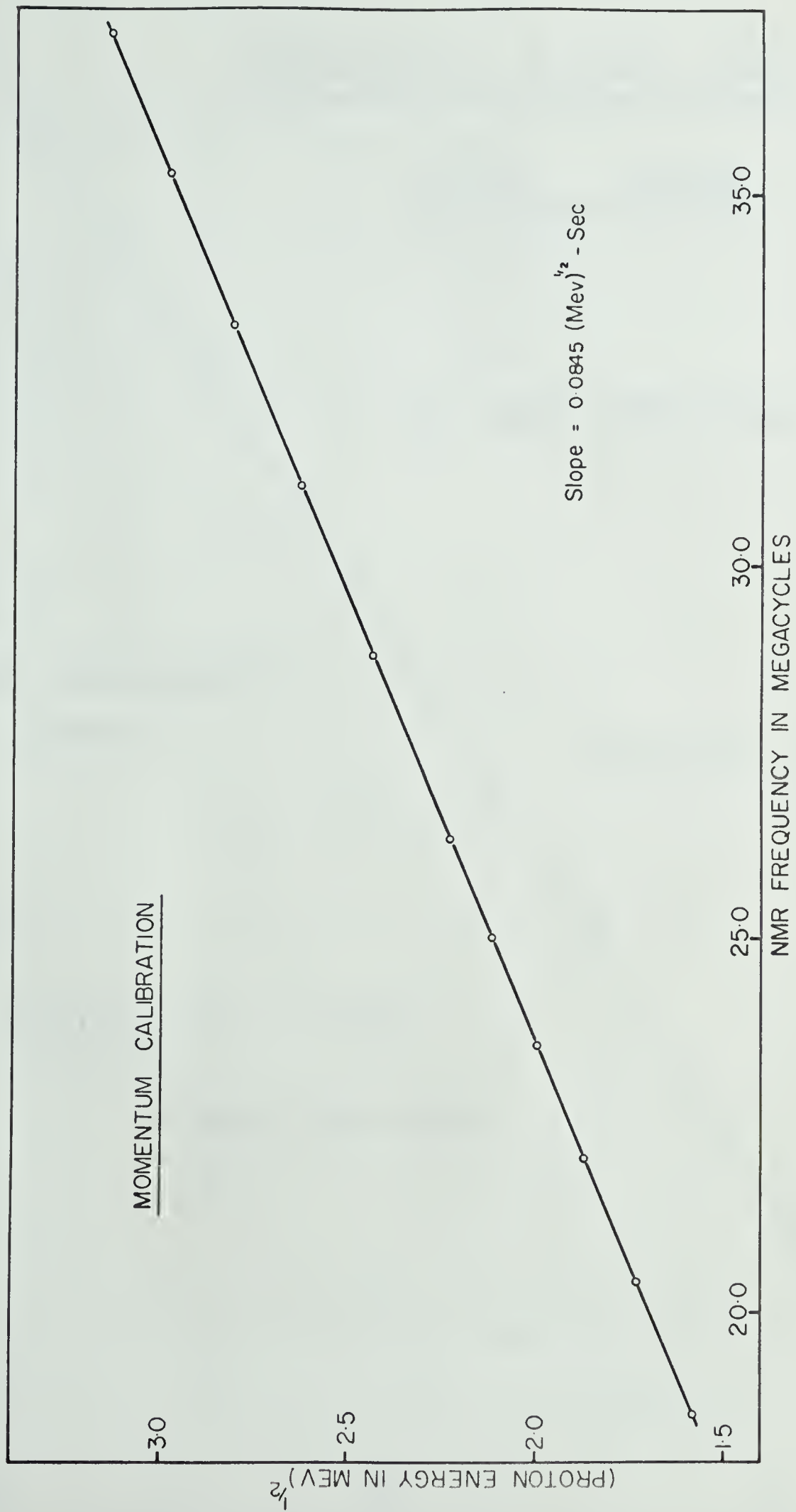


FIGURE 4-8

DISPERSION ALONG THE

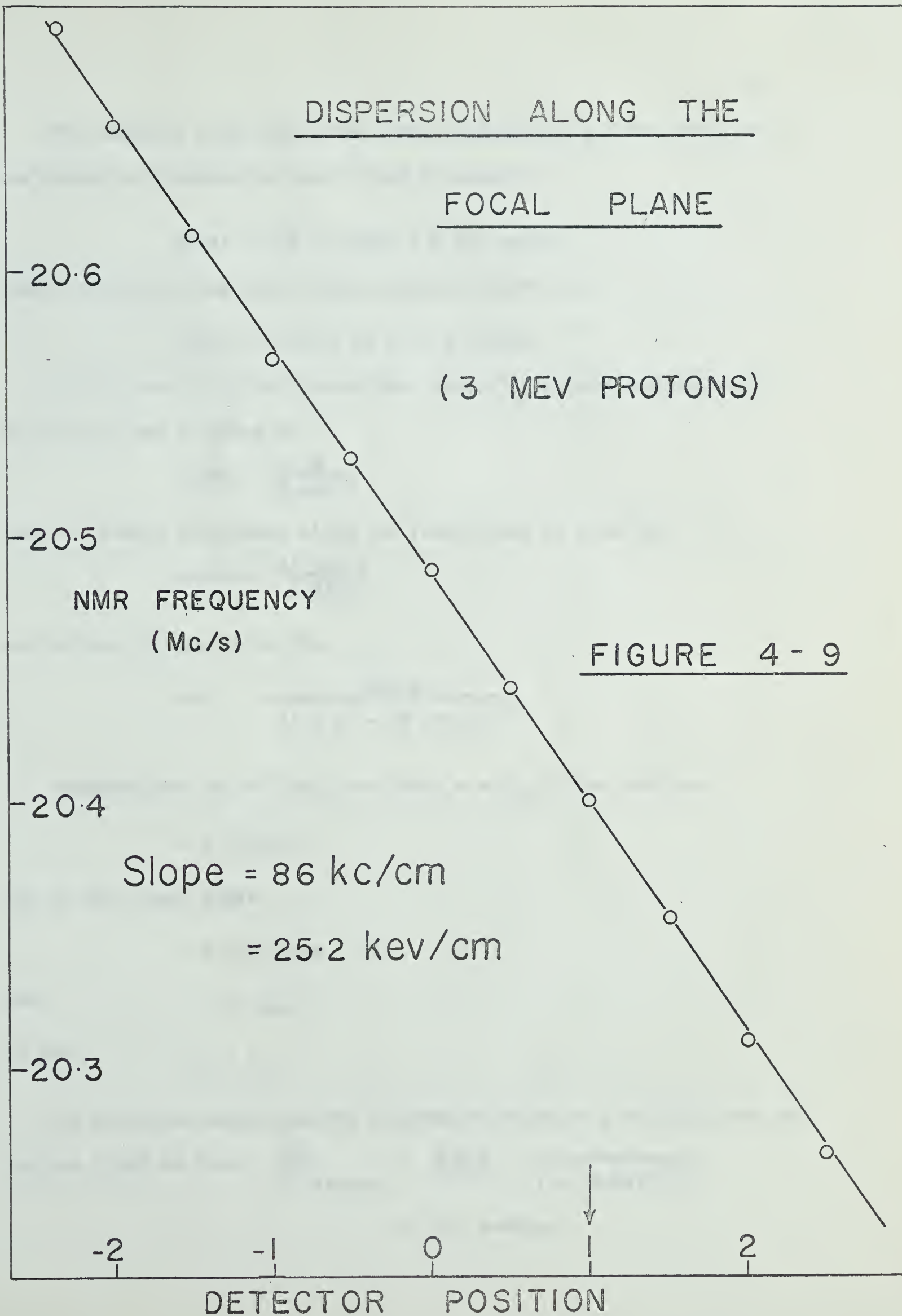
FOCAL PLANE

(3 MEV PROTONS)

NMR FREQUENCY
(Mc/s)

FIGURE 4 - 9

Slope = 86 kc/cm
= 25.2 kev/cm



The slope of this dispersion curve is 86 kc/cm, and the slope of the energy calibration curve at 3 MeV is given by

$$dE/dF = 2\sqrt{E} \times 0.0845 = 0.293 \text{ keV/kc.}$$

Hence the energy dispersion along the focal plane is:

$$dE/ds = 0.293 \times 86 = 25.2 \text{ keV/cm.}$$

We have seen that the theoretical energy dispersion perpendicular to the exit ray is given by

$$dE/dx_3 = \frac{2E}{q \sin \alpha}$$

Thus the energy dispersion along the focal plane is given by

$$dE/ds = \frac{2E \sin \gamma}{q \sin \alpha}$$

and we have already shown that

$$\sin \gamma = \frac{\sin \alpha}{(1 + e^2 - 2e \cos \alpha)^{1/2}}$$

Consider now the 90° ray, for which $r = R_{\text{eff}}$. For this ray

$$e = p/(p-r)$$

and in this case, since

$$p = 102.5 \text{ cms}$$

and

$$r = 52 \text{ cms}$$

we find

$$e = 2.03$$

We have also shown that the theoretical value of q is 105.5 cms. so

$$\begin{aligned} \text{that at 3 MeV we find } \frac{dE}{ds} \text{ theory} &= \frac{2 \times 3}{105.5} \cdot \frac{1}{\{1 + (2.03)^2\}^{1/2}} \\ &= 25.1 \text{ keV/cm.} \end{aligned}$$

This appears to justify the assumption that the detector is located on the 90° ray. We can, therefore, conclude that

$$r = R_{\text{eff}} = 52 \text{ cms.}$$

This means that the effective fringing field in the sharp cut-off approximation is 2 cms, or about 1.05 gap widths. This is perhaps a little higher than expected, but nonetheless entirely reasonable. Browne (Browne, 1956) assumed a fringing field of one gap width as a design figure for his spectrograph.

The dispersion measurement also provides a means of approximating the resolution of the system by allowing the image size to be expressed in terms of energy units. Along the focal plane this is

$$\begin{aligned} dE &= \frac{dE}{ds} \cdot M \cdot x_0 = \frac{dE}{ds} \cdot \frac{q}{p} \sin \gamma \cdot x_0 \\ &= 2.52 \times 1.03 \times 1.6 \\ &= 9.1 \text{ keV} \end{aligned}$$

at 3 MeV. This corresponds to a resolving power of 330, but it is quite apparent that the resolving power can be improved simply by making the beam spot on the target narrower. A new collimation system is currently being designed with rectangular slits to allow a narrower object without decreasing the area of the source. A resolving power greater than 1000 should be attainable.

The resolution along the focal plane calculated above is also the resolution which should be observed in the plane of the step wedge, since in this case

$$M = q/p$$

but now

$$\frac{dE}{ds}_{\text{wedge}} = \frac{dE}{ds}_{\text{focal plane}} \sin \gamma$$

(e) Solid Angle

In the spectrograph mode, the solid angle of the system is determined by very simple geometrical calculations. From the geometry of figure 4-10, the theoretical solid angle for the spectrograph is given by

$$\Omega = 4 \tan \theta_0 \tan \phi_0 = 4.2 \times 10^{-4} \text{ steradians}$$

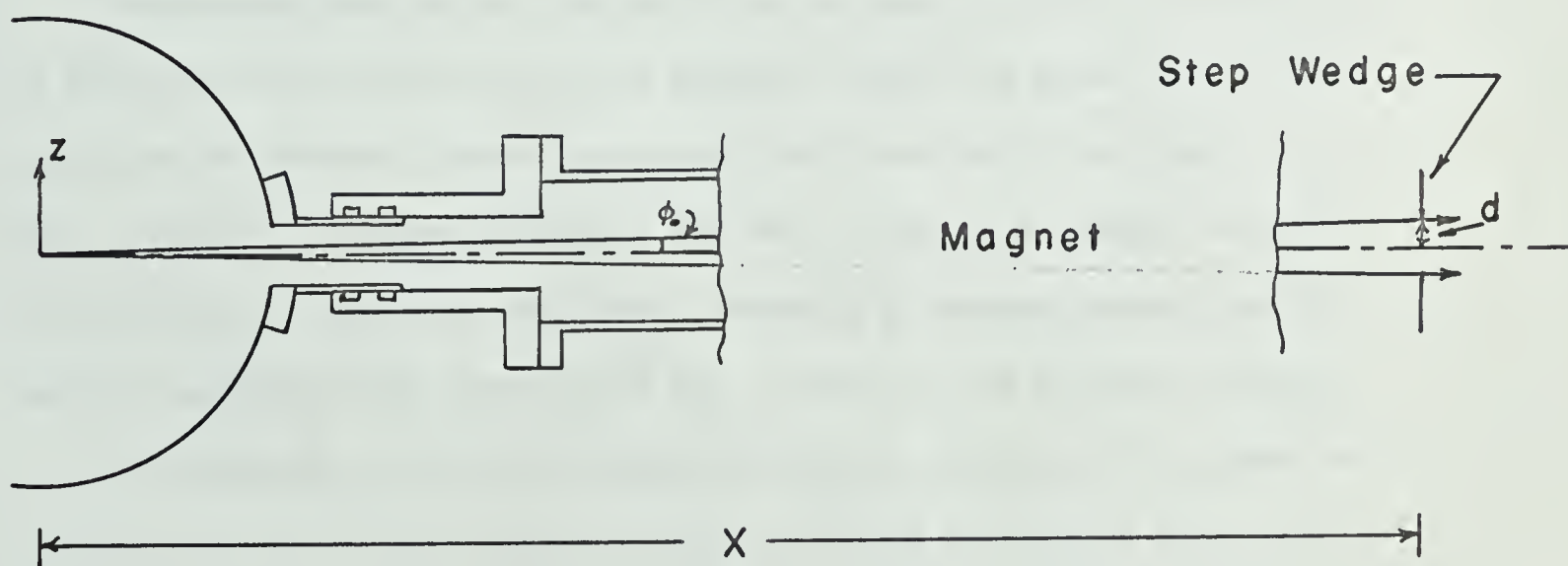
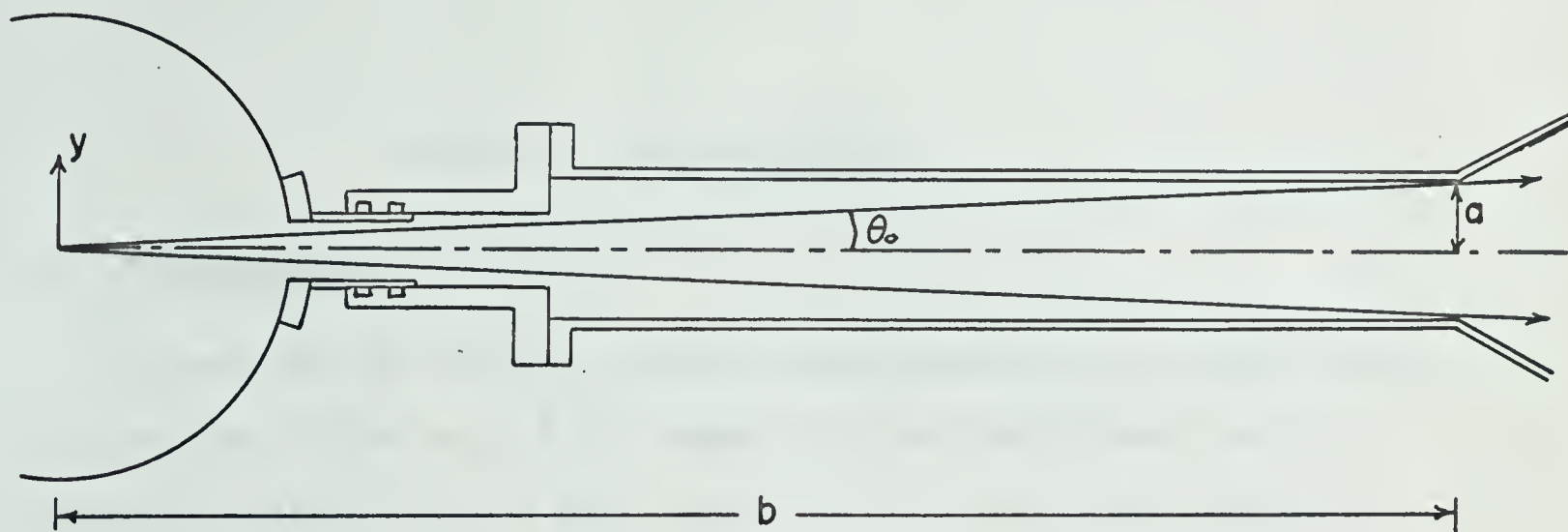
This value is so easily obtained, that it is best to consider it as the true solid angle of the system.

An attempt was made to obtain an experimental value for the solid angle of the system. Using the thickest target, for which the best thickness measurement was available, 10,244 protons were scattered into the system at 60° for an integrated current of 10^{-6} coulombs. The Rutherford scattering cross-section for gold at 3 MeV is 1.44×10^4 mb/steradian, which, with an assumed target thickness of $910 \mu\text{g}/\text{cm}^2$, gives

$$d\Omega = 4.1 \times 10^{-4} \text{ steradians.}$$

The excellent agreement here is largely coincidental, since an error of at least 10 - 20% must be assigned to the target thickness estimate.

FIGURE 4 - 10 SOLID ANGLE GEOMETRY



$$a = 1.5 \text{ cms.}$$

$$b = 30 \text{ cms.}$$

$$d = 0.4 \text{ cms.}$$

$$X = 187.3 \text{ cms.}$$

$$\Omega = 4 \tan \theta_0 \tan \phi_0 = 4ad/bX$$

$$\Omega = 4.2 \times 10^{-4} \text{ Steradians}$$

CHAPTER 5: THE SPECTROMETER

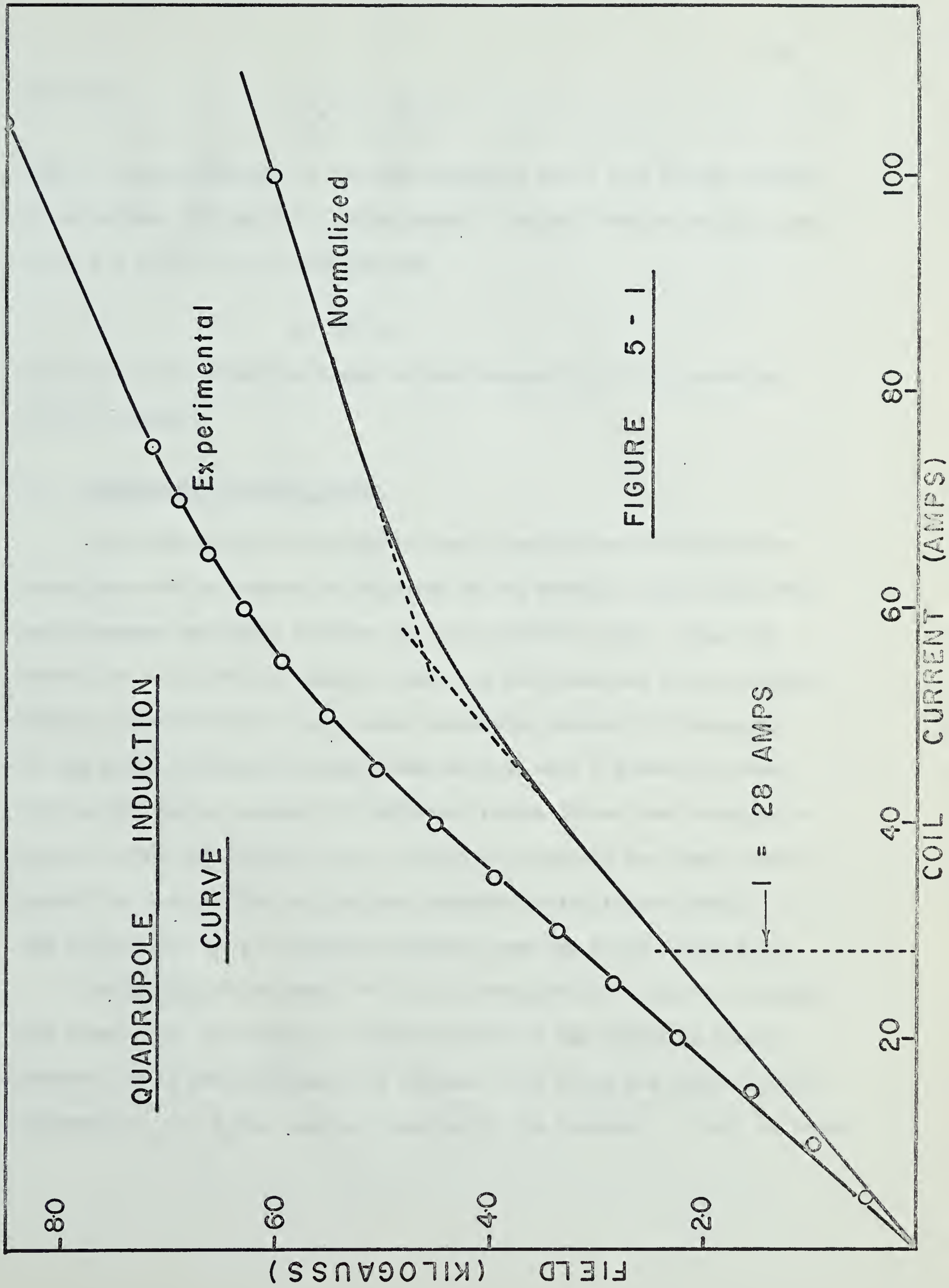
(a) Preliminaries

We have seen in Chapter 2 that all the properties of the spectrometer are functions of the ratio B_ℓ/B_0 , where B_ℓ is the field strength at the pole tips of the quadrupole lens, and B_0 is the field in the main magnet. Because only one point on the B vs. I curve for the quadrupole lens was given in specifications provided by the manufacturer, it was necessary to obtain such a curve ourselves.

The correct way to do this would be to place a Hall probe directly on the pole tip, but this was not possible since the beam tube, which could not be removed, comes in contact with the four pole tips. It was, therefore, decided to locate the Hall probe at a random location in the field of the lens, and then, assuming a constant normalization factor, normalize the resulting B vs. I curve to the one known point.

The results of this calibration are shown in figure 5-1, where we observe that the linear region extends up to 40 amperes, a fact we will refer to later.

The physical length, L' , of the pole tips is 4", or 10.2 cms., but in calculations concerning the effects of the lens it is necessary to assume an effective length, L , of the lens to account for fringing effects. Penner (Penner, 1961) states that the effective length of the lens is



given by

$$L = L' + \epsilon d$$

where d is the diameter of the lens aperture, and ϵ is a factor usually lying between $1/4$ and $3/4$. If we assume ϵ for our case to be $1/2$, then, since $d = 1.375''$ or 3.5 cms. we find

$$L \sim 12 \text{ cms}$$

and this is the effective length we have assumed in all calculations in this Chapter.

(b) Location of the Focal Plane

The function of the quadrupole lens is to increase the effective solid angle of the system by focussing in the vertical plane while the spectromagnet continues to focus in the horizontal plane. Thus the system has two different focal planes, one for focussing in the vertical plane, which we refer to as Z plane focussing, and one for focussing in the usual, horizontal plane, which we will call Y plane focussing. For the 90° ray in a magnet of effective radius 52 cms. and assuming a lens of effective length 12 cms., the position of the two focal points depends on the position of the lens relative to the target, defined by the location x_1 of its effective entrance, and the field radius B_ℓ/B_0 .

The problem of locating the Y plane focus, which is the one important for resolution, is similar to that described in the preceding Chapter. However, it is now complicated by the fact that there are three variable parameters: x_1 , B_ℓ/B_0 , and the position of the detector. If all of these

parameters are allowed to vary, the problem of locating the focus becomes very involved, and the focus arrived at may not correspond to the best solid angle attainable.

It was, therefore, decided to set the lens as close to the target as possible, the position at which the effective solid angle should be expected to be greatest. The limitation here is the point where the lens coils come into contact with the target chamber. Taking into account the effective length of the lens, this sets x_1 at 16 cms.

The position of the Y plane focus was then determined at 3 MeV by first varying the detector position until the best focus was observed by the method described in Chapter 4, then varying the current in the quadrupole until the best focus was observed, then varying the detector position again, etc. Figure 5-2 shows the final plot of the focus against the bucking current in the lens. With the detector located 76.1 cms. from the pole tips, that is, with $\ell_2 = 74.1$ cms., the best focus was observed at a bucking current of 7 amps, where 95.5% of the counts fell in one step of the wedge.

At 3 MeV, the current in the main coils is 35 amps, corresponding to a field B_0 of 4.8 kilogauss. The lens current, therefore, was 28 amps, which, from figure 5-1, corresponds to a pole tip field B_ℓ of 2.3 kilogauss, from which

$$B_\ell/B_0 = 0.48$$

We have already shown that the Y plane focus should occur at

$$\ell_2 = \frac{R^2(x_1 k \sinh kL + \cosh kL)}{x_1 \cosh kL + \frac{\sinh kL}{k} + (\ell_1 - x_2)(x_1 k \sinh kL + \cosh kL)}$$

RESOLUTION & ENHANCEMENT

VS QUADRUPOLE BOOST

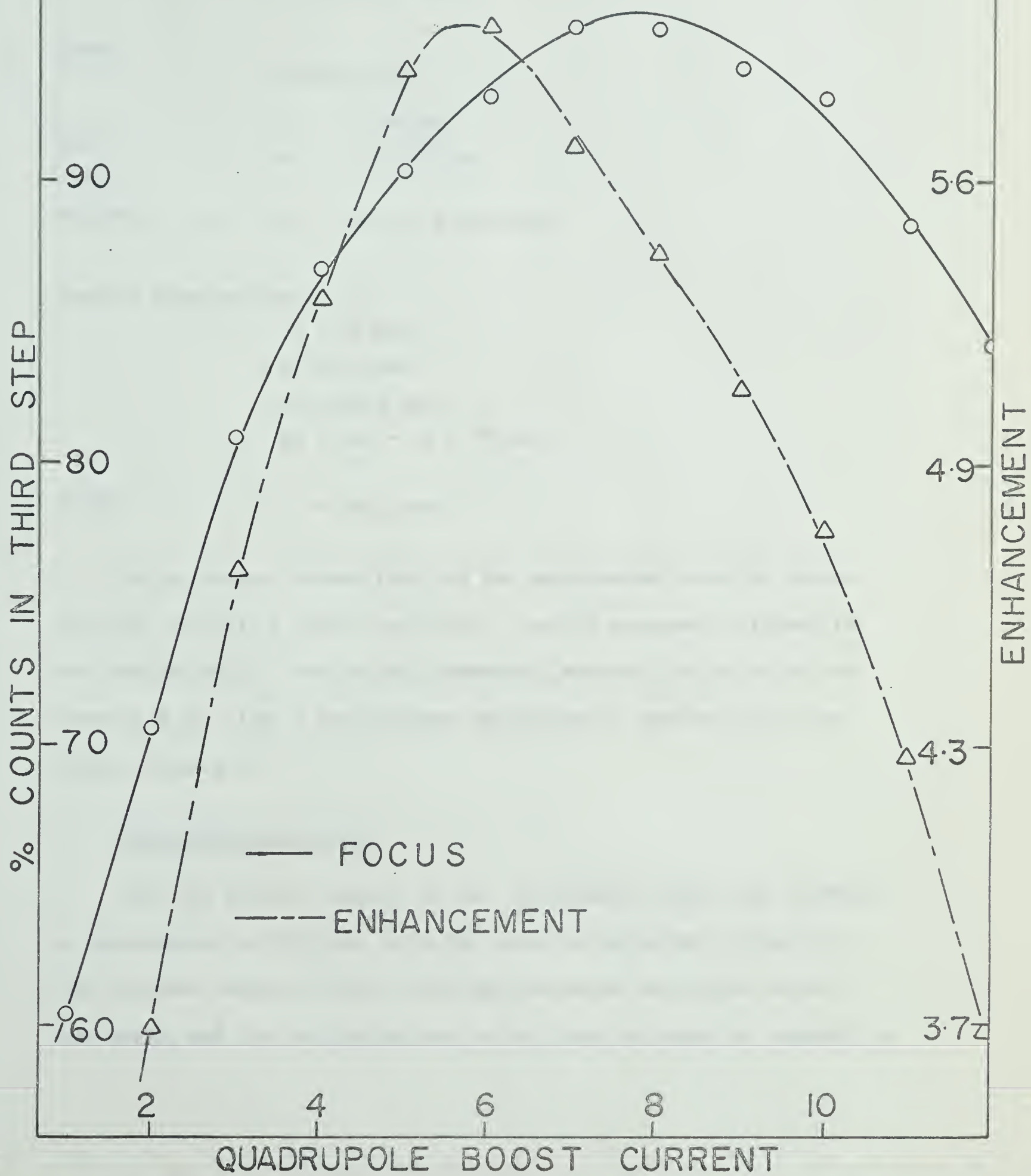


FIGURE 5-2

where

$$k = \left(\frac{B_{\ell}/B_0}{aR} \right)^{1/2}$$

Since

$$B_{\ell}/B_0 = 0.48$$

$$R = 52 \text{ cms}$$

and

$$a = 1.747 \text{ cms}$$

we find

$$k = 7.26 \times 10^{-2} \text{ cm}^{-1}$$

Further substituting

$$x_1 = 16 \text{ cms}$$

$$L = 12 \text{ cms}$$

$$\ell_1 = 50.5 \text{ cms}$$

$$x_2 = (x_1 + L) = 28 \text{ cms.}$$

we get

$$\ell_2 = 73.6 \text{ cms.}$$

The agreement between this and the experimental value is better than 1%, which is a great deal better than the agreement attained for the spectrograph. This is not unexpected, however, as the method of varying B_{ℓ}/B_0 gives a much sharper definition of the best focus, as seen in figure 5-2.

(c) The Calibration Curve

With the detector placed at the spectrometer focus thus located, a spectrometer calibration curve was taken as described in Chapter 4. The incident energy of the protons and deuterons was varied in half MeV steps, and the bucking current in the lens increased as required to

maintain the best focus. Again the calibration was performed using both gold and aluminum elastic scattering. The results of this work are shown in Table 5-1.

Figure 5-3 is the calibration curve, showing all the points that were taken, both in the spectrograph and spectrometer modes. Here we observe that the spectrometer points fall very close to the spectrograph points, a further indication that the detector was located on the 90° exit ray. Once again an expanded scale shows that the aluminum points occur at frequencies slightly higher than the gold curve, although this discrepancy does not seem to be quite so large in the spectrometer mode.

An attempt was made to establish further points on the calibration curve by searching for some of the lower lying states of Al^{28} from the reaction $\text{Al}^{27}(\text{d},\text{p})\text{Al}^{28}$. At an incident energy of 3 MeV, only one such state, the 2.9880 MeV level, was strong enough to be useful, and it is plotted on the complete calibration curve (figure 5-3). The spectrum obtained for this peak is shown in figure 5-4. The four lower energy peaks are deuterons scattered from some lower A contaminant, as indicated by the broadness of the image.

(d) Dispersion, Magnification, Resolution

We have shown in Chapter 2 that for the spectrometer, as for the spectrograph, the energy dispersion perpendicular to the exit ray is

$$\frac{dE}{dx_3} = \frac{2E}{q \sin \alpha}$$

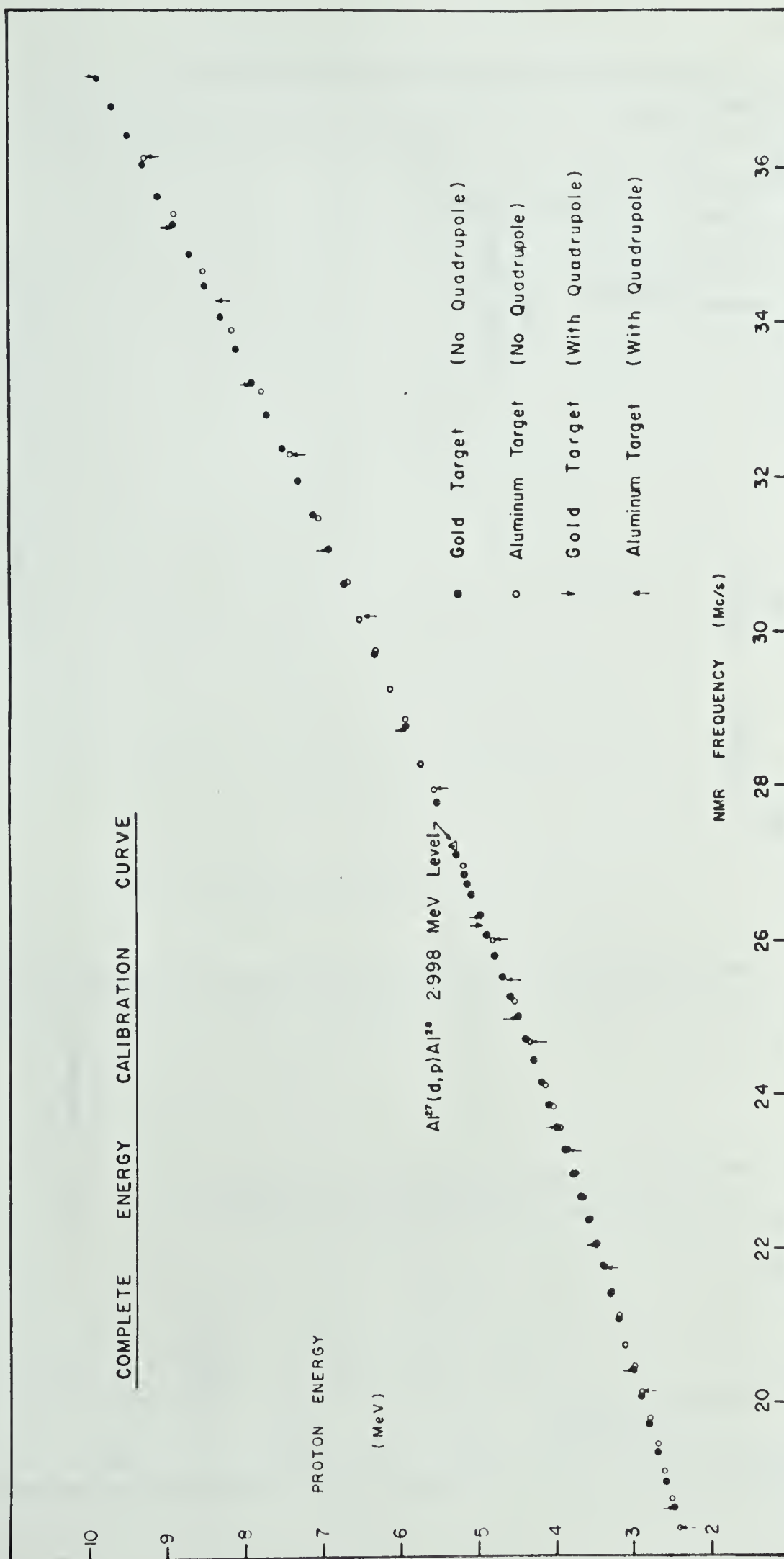


FIGURE 5 - 3

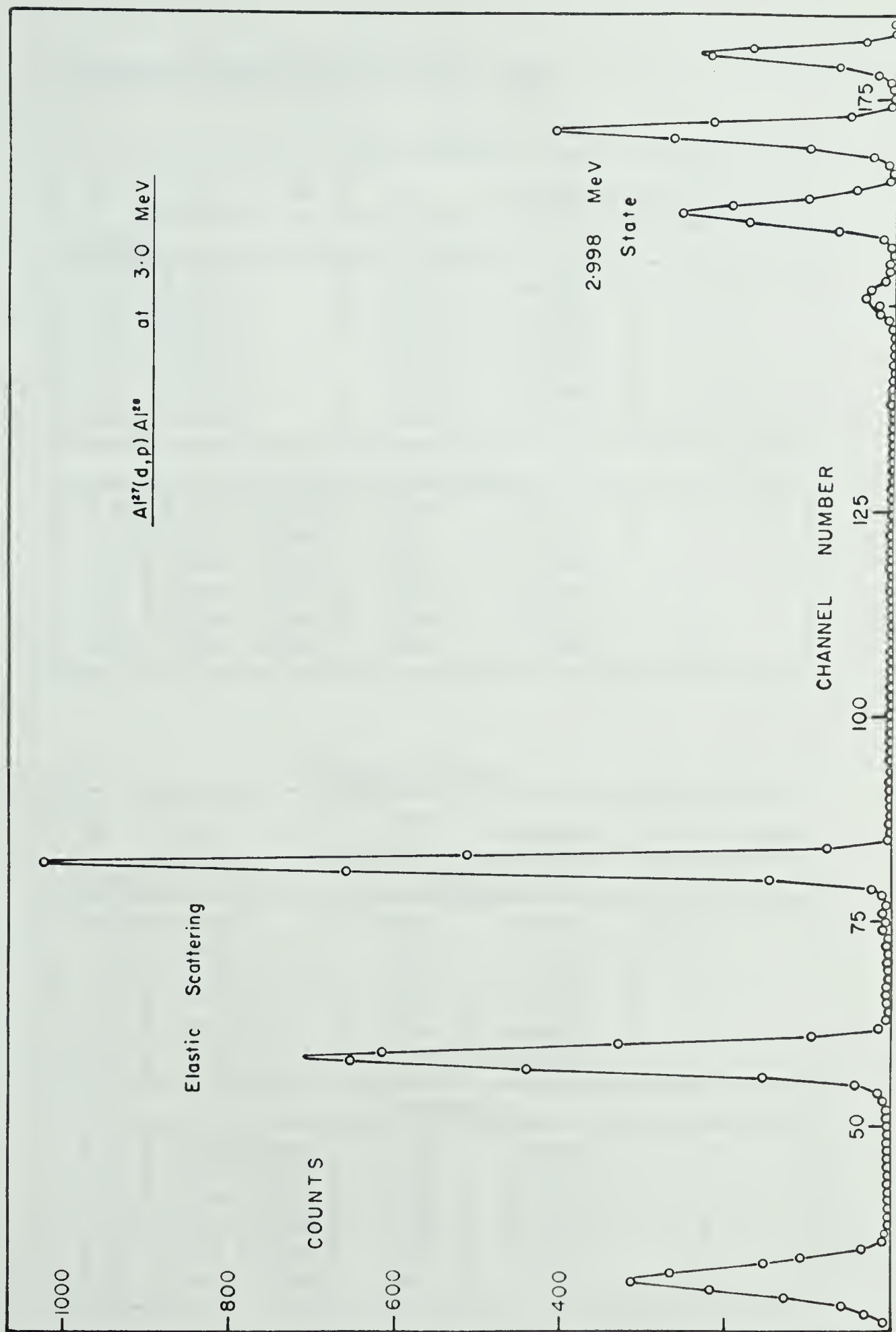


FIGURE 5 - 4

TABLE 5-1

Dispersion Curve with Quadrupole Lens

| Gold Target | | | | | |
|-------------|---------|--------|--------------|-----------|-------------|
| E_0 | E_3 | $2E_3$ | $\sqrt{E_3}$ | Frequency | Quad. Boost |
| (MeV) | Protons | | | | |
| 2.5 | 2.487 | | 1.578 | 18.616 | 6 |
| 3.0 | 2.985 | | 1.728 | 20.401 | 7 |
| 3.5 | 3.482 | | 1.866 | 22.032 | 7 |
| 4.0 | 3.980 | | 1.995 | 23.557 | 7 |
| 4.5 | 4.477 | | 2.116 | 24.996 | 7 |
| 5.0 | 4.974 | | 2.230 | 26.343 | 7 |
| Deuterons | | | | | |
| 2.5 | 2.475 | 4.950 | 2.224 | 26.214 | 7 |
| 3.0 | 2.970 | 5.940 | 2.437 | 28.734 | 7 |
| 3.5 | 3.464 | 6.928 | 2.631 | 31.069 | 7 |
| 4.0 | 3.959 | 7.918 | 2.813 | 33.219 | 9 |
| 4.5 | 4.454 | 8.908 | 2.986 | 35.245 | 10 |
| 5.0 | 4.949 | 9.898 | 3.145 | 37.182 | 10 |

| Aluminum Target | | | | | |
|-----------------|---------|--------|--------------|-----------|-------------|
| E_0 | E_3 | $2E_3$ | $\sqrt{E_3}$ | Frequency | Quad. Boost |
| (MeV) | Protons | | | | |
| 2.5 | 2.408 | | 1.552 | 18.355 | 6 |
| 3.0 | 2.890 | | 1.700 | 20.119 | 6 |
| 3.5 | 3.371 | | 1.836 | 21.733 | 7 |
| 4.0 | 3.853 | | 1.963 | 23.237 | 7 |
| 4.5 | 4.335 | | 2.081 | 24.649 | 7 |
| 5.0 | 4.816 | | 2.195 | 25.975 | 7 |
| Deuterons | | | | | |
| 2.5 | 2.3199 | 4.640 | 2.153 | 25.500 | 7 |
| 3.0 | 2.784 | 5.568 | 2.360 | 27.955 | 7 |
| 3.5 | 3.248 | 6.495 | 2.548 | 30.225 | 9 |
| 4.0 | 3.712 | 7.424 | 2.725 | 32.325 | 9 |
| 4.5 | 4.176 | 8.352 | 2.890 | 34.285 | 10 |
| 5.0 | 4.640 | 9.280 | 3.047 | 36.151 | 10 |

In our case, since $\alpha = 90^\circ$ and

$$q = (R + \ell_2) = 125.6 \text{ cms}$$

we get, at 3 MeV

$$\frac{dE}{dx_3} = 47.6 \text{ keV/cm.}$$

The dispersion along the spectrometer focal plane is rather difficult to evaluate, since the general expression for ℓ_2 (equation 2-50) must be differentiated in order to find the slope of the focal plane at the 90° ray. The differentiation is complicated by the fact that the arguments of all the hyperbolic functions, being functions of r , are also functions of α . However, the dispersion along the focal plane is of no particular significance in the spectrometer mode, it cannot easily be measured with the existing arrangement, and it is not needed to evaluate the resolution, so there is no need to undertake this calculation.

We have also shown that the Y plane magnification of the spectrometer is given by

$$M_y = \frac{-\ell_2/R}{x_1 k \sinh kL + \cosh kL}$$

Using the values for ℓ_2 , R , x , k and L obtained in sections (a) and (b) we find

$$M_y = 0.56$$

Thus we expect a 0.9 mm image in the plane of the detector from our 1.6 mm diameter beam spot.

Expressing this image size in energy units, the resolution at 3 MeV should be

$$\begin{aligned} dE &= 47.6 \text{ keV/cm} \times 0.09 \text{ cm} \\ &= 4.3 \text{ keV} \end{aligned}$$

As explained in Chapter 4, section (d), the same resolution should be observed along the focal plane.

Because the image is 0.9 mm across, while each step in the step wedge is 2 mm. wide, the spatial resolution of the step wedge is not adequate to observe the system resolution. If the entire peak can be obtained in one step of the wedge, it is the step width which determines the observable resolution. Thus we would expect to be able to observe a resolution at 3 MeV of

$$\begin{aligned} dE &= 47.6 \text{ keV/cm} \times 0.2 \text{ cm} \\ &\sim 9.4 \text{ keV} \end{aligned}$$

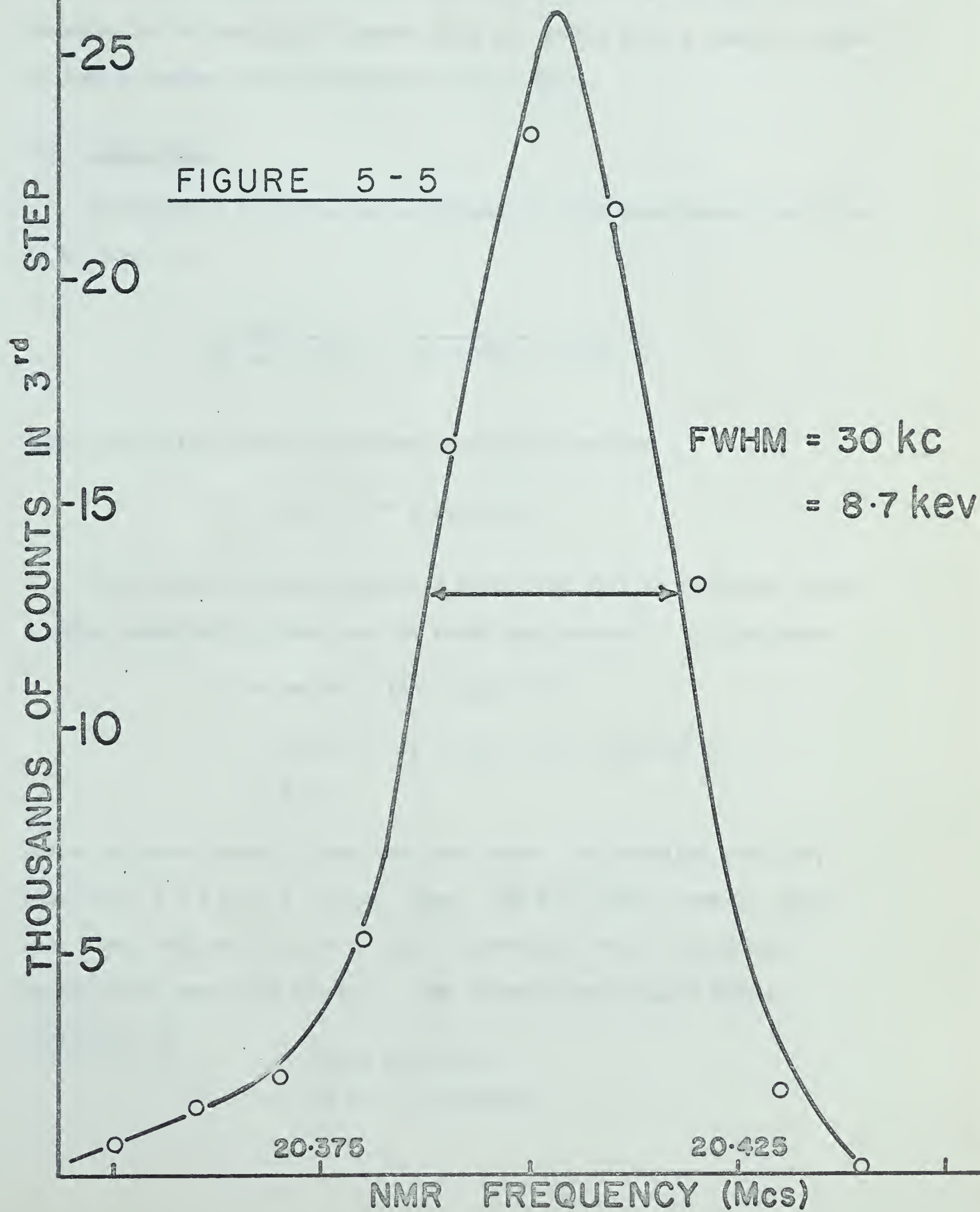
The resolution was observed by varying the magnetic field and counting only those particles which arrived in the third step. The result is shown in figure 5-5. The full width at half maximum is 30 kilocycles, which, at 3 MeV, corresponds to

$$\begin{aligned} dE &= 2 \times 0.845 \times E^{1/2} \times dF \\ &\approx 8.7 \text{ keV.} \end{aligned}$$

The difference between this and the predicted value may be attributed entirely to the FWHM measurement. dE becomes 9.4 keV if the FWHM is taken as 32 kilocycles, which is well within reasonable error estimates.

SPECTROMETER

RESOLUTION



The acquisition of a position sensitive detector, combined with a decrease in the beam spot diameter to 1 mm, should make a resolving power of 1000 or better both obtainable and observable.

(e) Solid Angle

In Chapter 2 the effective solid angle of the spectrometer was shown to be given by

$$\Omega = \frac{2a^2 k^2}{(x_1^2 k^2 + 1)^{1/2}} \frac{1}{kx_1 \cosh kL + \sinh kL}$$

Again making the substitutions mentioned above we find

$$\Omega = 8.04 \times 10^{-3} \text{ steradians.}$$

This is not, however, the solid angle that will be observed, as the Z plane magnification must also be taken into account. In this plane

$$\begin{aligned} M_Z &= \cos kL - (X - x_2)k \sin kL \\ &= \cos kL - (\ell_1 + \pi r/2 + \ell_2 - x_2)k \sin kL \\ &= 9.25 \end{aligned}$$

where the usual substitutions have been used. The vertical image is, therefore, $1.6 \times 9.25 = 14.8$ mm. high. The step wedge, however, being only 8 mm. high acts as a stop which allows only 54% of the focused particles to reach the detector. The observed solid angle should, therefore, be

$$\begin{aligned} \Omega &= 0.54 \times 8.04 \times 10^{-3} \\ &\approx 4.3 \times 10^{-3} \text{ steradians} \end{aligned}$$

an approximate enhancement of a factor of 10 over the solid angle in the spectrograph mode.

Such a large enhancement was never observed. Moreover, the observed enhancements seemed to be rather difficult to reproduce. The largest enhancement observed, in a deliberate enhancement measurement, was 7.1. In another test, where the enhancement was plotted as a function of the bucking current in the quadrupole, (see Table 5-2 and figure 5-2) the largest enhancement was 5.9. This difficulty with the reproducibility of the spectrometer solid angle is probably largely due to the sensitivity of the Z plane magnification to the ratio B_ℓ/B_0 and to the position of the detector relative to the Z plane focus.

It should be possible, however, to keep the spectrometer solid angle constant if care is taken to keep the ratio B_ℓ/B_0 constant. To verify this a series of normalization curves were prepared at various energies by plotting the counting rates vs. the current in the quadrupole lens.

Next, a plot was made of counting rate vs. $1/E^2$, setting the quadrupole current at reasonable values. This gave the meaningless scatter of points shown in figure 5-6. The results were then normalized by referring to the normalization curves to find what the counting rates would have been had the lens current been set exactly to keep I_ℓ/I_0 constant (using the fact that we were on the linear portion of both B vs. I curves.) These normalized curves are shown in figure 5-7. The lines are straight and pass through the origin, indicating that for each value of I_ℓ/I_0 the solid angle is constant over the entire energy range.

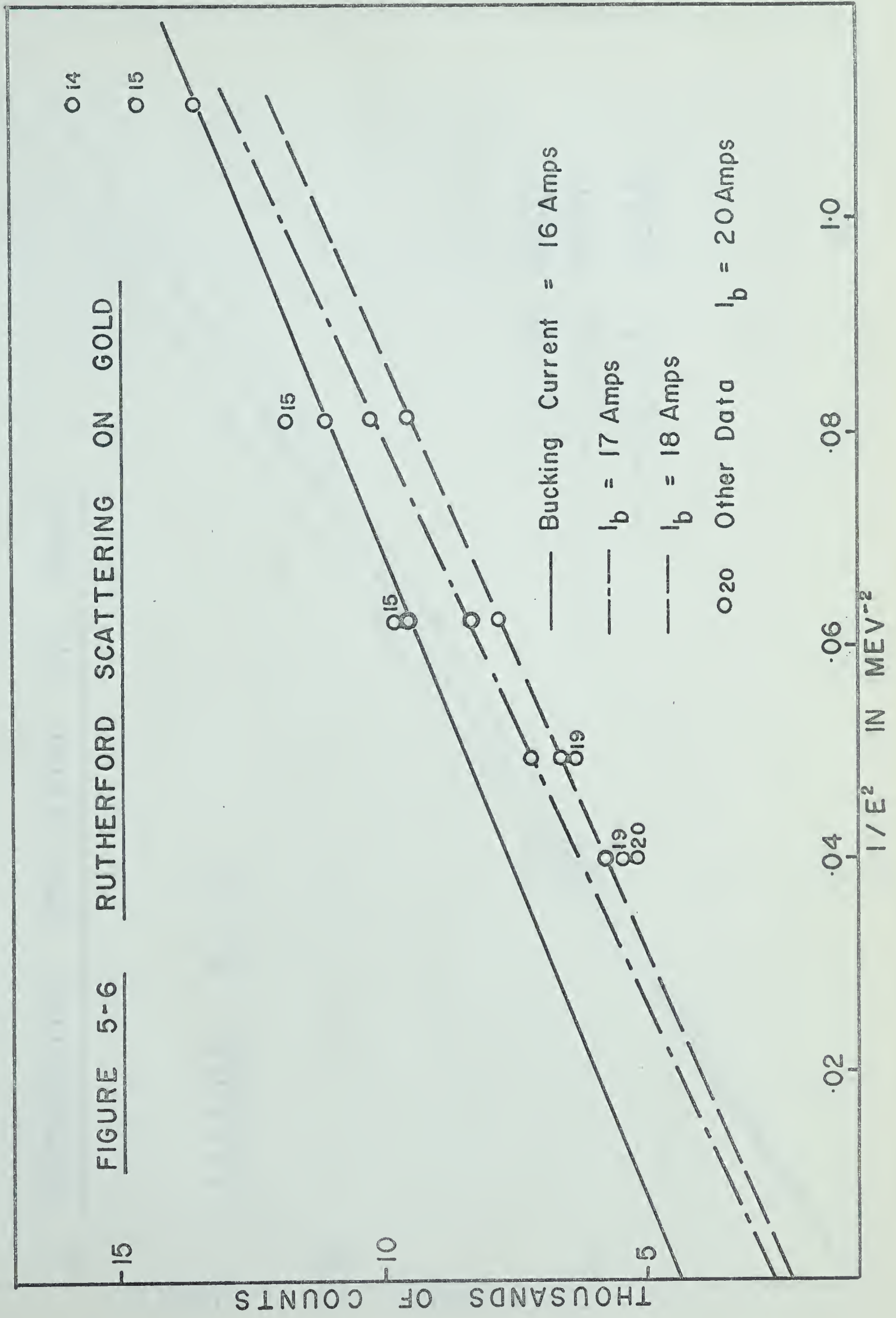
TABLE 5-2

| Run | Quad Boost | f _{mag} | Current | Counts in third step | Total counts | Per cent in third step | Enhancement |
|-----|------------|------------------|----------------------------|----------------------|--------------|------------------------|-------------|
| 391 | 1 | 20,411 | 30 x 10 x 10 ⁻⁸ | 10,809 | 17,877 | 60.5 | 3.2 |
| 380 | 2 | 20,4 | 60 x 10 x 10 ⁻⁸ | 29,013 | 41,109 | 70.6 | 3.7 |
| 390 | 3 | 20,410 | 30 x 10 x 10 ⁻⁸ | 21,165 | 26,134 | 80.9 | 4.7 |
| 381 | 4 | 20,406 | 60 x 10 x 10 ⁻⁸ | 51,735 | 59,508 | 86.9 | 5.3 |
| 389 | 5 | 20,406 | 30 x 10 x 10 ⁻⁸ | 29,436 | 32,587 | 90.4 | 5.8 |
| 382 | 6 | 20,404 | 60 x 10 x 10 ⁻⁸ | 60,764 | 65,441 | 93.0 | 5.9 |
| 388 | 7 | 20,403 | 30 x 10 x 10 ⁻⁸ | 29,978 | 31,396 | 95.5 | 5.6 |
| 383 | 8 | 20,401 | 60 x 10 x 10 ⁻⁸ | 57,498 | 60,271 | 95.4 | 5.4 |
| 387 | 9 | 20,402 | 30 x 10 x 10 ⁻⁸ | 26,762 | 28,426 | 94.0 | 5.1 |
| 384 | 10 | 20,405 | 60 x 10 x 10 ⁻⁸ | 49,679 | 53,456 | 93.0 | 4.8 |
| 386 | 11 | 20,408 | 30 x 10 x 10 ⁻⁸ | 21,093 | 23,811 | 88.5 | 4.3 |
| 385 | 12 | 20,409 | 60 x 10 x 10 ⁻⁸ | 35,013 | 41,602 | 84.2 | 3.7 |

Counts at no quadrupole focus: 5,573

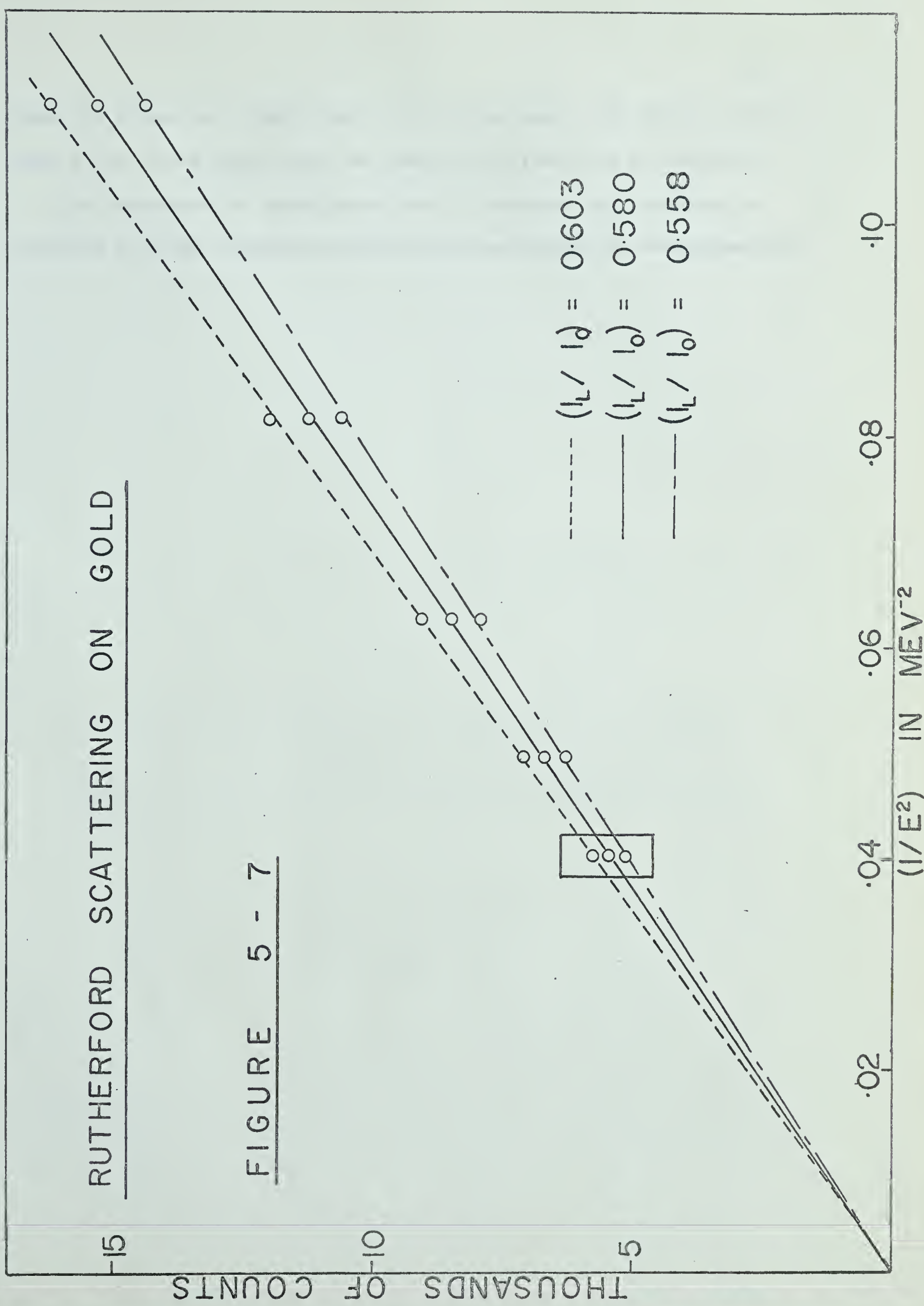
Focus 91.8%

FIGURE 5-6 RUTHERFORD SCATTERING ON GOLD



RUTHERFORD SCATTERING ON GOLD

FIGURE 5 - 7



Since the slopes are proportional to the solid angle, the effect of the ratio B_ℓ/B_0 on the solid angle is clearly seen from this illustration.

The importance of taking great care to maintain the constancy of the ratio of B_ℓ/B_0 in angular distribution work cannot be overemphasized.

APPENDIX A: THE QUADRUPOLE LENS

It seems apparent that the most efficient use of the lens occurs when the Y plane and the Z plane foci coincide. The spectrometer should, therefore, be designed in such a way that the two focus points are coincident at a reasonable position for reasonable values of the other parameters B_ℓ/B_0 and x_1 . Perhaps the best way to realize this is by fixing B_ℓ/B_0 and x_1 , and then solving the two focus equations simultaneously for ℓ_2 and the lens length, L .

Table A-1 shows a sample output from a program which does just this. The input parameters used by Enge (Enge, 1958) in his proposed design have been used here. Enge now states:

For convenience, the coils of the two magnets could be energized from the same power supply (series connection). The induction ratio B_ℓ/B_0 should be chosen so that the hysteresis loops of the two magnets track reasonably well together. This consideration fixes the induction ratio to approximately $B_\ell/B_0 \approx 0.6$ to 0.7 for practical design.

Choosing $B_\ell/B_0 = 0.65$ we see from Table A-1 that $x_2 = 22.35$ cms, giving a lens length of $L = 22.35 - 15.00 = 7.35$ cms. The double focus is located 63.6 cms. from the field cut-off, and the solid angle is 9.2×10^{-3} steradians. These are also the values given by Enge.

Table A-2 is the output of the same program for the spectrometer geometry described in this thesis, with x_1 set at 16 cms. If we choose $B_\ell/B_0 = 0.65$, a lens length of 8.3 cms. is required for double focusing,

TABLE A-1

Spectromagnetic Focusing Conditions

$x_1 = 15$

$R_0 = 50$

| B_ℓ/B_0 | x_2 | L_2 | ω |
|--------------|---------|---------|----------|
| 0.400 | 26.2409 | 66.3204 | 0.00674 |
| 0.450 | 25.1595 | 65.5180 | 0.00730 |
| 0.500 | 24.2714 | 64.8797 | 0.00783 |
| 0.550 | 23.5285 | 64.3598 | 0.00831 |
| 0.600 | 22.8975 | 63.9281 | 0.00876 |
| 0.650 | 22.3545 | 63.5637 | 0.00917 |
| 0.700 | 21.8822 | 63.2522 | 0.00956 |
| 0.750 | 21.4675 | 62.9827 | 0.00991 |
| 0.800 | 21.1004 | 62.7473 | 0.01025 |
| 0.850 | 20.7730 | 62.5398 | 0.01056 |

TABLE A-2

Spectromagnetic Focusing Conditions

$x_1 = 16$

$R_0 = 50$

| B_ℓ/B_0 | x_2 | L_2 | ω |
|--------------|---------|---------|----------|
| 0.400 | 28.6587 | 72.9223 | 0.00767 |
| 0.425 | 28.0223 | 72.3875 | 0.00801 |
| 0.450 | 27.4484 | 71.9143 | 0.00834 |
| 0.475 | 26.9279 | 71.4926 | 0.00865 |
| 0.500 | 26.4537 | 71.1143 | 0.00895 |
| 0.525 | 26.0196 | 70.7731 | 0.00924 |
| 0.550 | 25.6208 | 70.4637 | 0.00952 |
| 0.575 | 25.2531 | 70.1820 | 0.00979 |
| 0.600 | 24.9128 | 69.9243 | 0.01005 |
| 0.625 | 24.5971 | 69.6876 | 0.01030 |
| 0.650 | 24.3033 | 69.4696 | 0.01054 |
| 0.675 | 24.0292 | 69.2680 | 0.01077 |
| 0.700 | 23.7728 | 69.0811 | 0.01100 |
| 0.725 | 23.5325 | 68.9073 | 0.01121 |
| 0.750 | 23.3067 | 68.7454 | 0.01142 |
| 0.775 | 23.0943 | 68.5940 | 0.01163 |
| 0.800 | 22.8939 | 68.4523 | 0.01183 |
| 0.825 | 22.7047 | 68.3193 | 0.01202 |

considerably shorter than the 12 cm. lens provided with the spectrometer. The table indicates that a 12 cm. lens is called for if the induction ratio is chosen to be $B_{\ell}/B_0 = 0.425$. (The solid angle at this ratio is 25% smaller.)

Enge's comment, quoted above, suggests that this ratio does not constitute a "practical design." Another criterion of practicality could be, however, that the current ratio be selected so as to give a field ratio which remains constant over the largest part of the induction (B vs. I) curves of the two magnets. This is equivalent to the condition that the field ratio be such that both induction curves reach their bend at the same time.

Taking this as the criterion for the choice of field ratio for a "practical design," the appropriate ratio can be found by taking the ratio of the fields at the intersections of the straight line portions of the two induction curves. Referring to figures 3-1 and 5-1, this ratio is 0.48, which, by an extremely happy coincidence, is exactly the field ratio used in the experiments described in Chapter 5. This corresponds to a current ratio I_{ℓ}/I_0 of approximately 0.75. Table A-3a shows the variation in the field ratio which would result from keeping the current ratio constant at 0.75. Between 30 and 110 amps, the field ratio changes only 2.5%.

By comparison, suppose a current ratio of 1.3 is chosen in order to give field ratios in the vicinity of 0.65, as suggested by Enge. Table A-3b shows the resulting variation in field ratios to be 25%.

TABLE A-3a

| I_0 | $I_\ell = 0.75 I_0$ | B_ℓ | B_0 | B_ℓ/B_0 |
|-------|---------------------|----------|-------|--------------|
| 10 | 7.5 | .6 | 1.4 | .42 |
| 20 | 15 | 1.2 | 2.7 | .44 |
| 30 | 22.5 | 1.8 | 3.95 | .46 |
| 40 | 30 | 2.4 | 5.2 | .47 |
| 50 | 37.5 | 3.1 | 6.5 | .47 |
| 60 | 45 | 3.6 | 7.8 | .46 |
| 70 | 52.5 | 4.2 | 8.9 | .47 |
| 80 | 60 | 4.6 | 9.7 | .47 |
| 90 | 67.5 | 4.9 | 10.3 | .47 |
| 100 | 75 | 5.2 | 10.9 | .47 |
| 110 | 82.5 | 5.4 | 11.3 | .48 |
| 120 | 90 | 5.7 | 11.8 | .48 |

TABLE A-3b

| I_0 | $I_\ell = 1.3 I_0$ | B_ℓ | B_0 | B_ℓ/B_0 |
|-------|--------------------|----------|-------|--------------|
| 20 | 27 | 2.2 | 2.7 | .81 |
| 30 | 39 | 3.2 | 3.9 | .81 |
| 40 | 52 | 4.1 | 5.2 | .79 |
| 50 | 65 | 4.8 | 6.5 | .74 |
| 60 | 78 | 5.3 | 7.8 | .68 |
| 70 | 91 | 5.7 | 8.9 | .64 |
| 80 | 104 | 6.1 | 9.7 | .63 |

TABLE A-3c

| I_0 | $I_\ell = 0.61 I_0$ | B_ℓ | B_0 | B_ℓ/B_0 |
|-------|---------------------|----------|-------|--------------|
| 20 | 12.2 | .9 | 2.7 | .35 |
| 30 | 18.3 | 1.5 | 3.9 | .38 |
| 40 | 24.4 | 2.0 | 5.2 | .38 |
| 50 | 30.5 | 2.5 | 6.5 | .38 |
| 60 | 36.6 | 3.0 | 7.8 | .39 |
| 70 | 42.7 | 3.5 | 8.9 | .39 |
| 80 | 48.8 | 3.9 | 9.7 | .40 |
| 90 | 54.9 | 4.3 | 10.3 | .42 |
| 100 | 61.0 | 4.6 | 10.9 | .42 |
| 110 | 67.1 | 4.9 | 11.3 | .43 |
| 120 | 73.1 | 5.1 | 11.8 | .43 |
| 130 | 79.2 | 5.4 | 12.3 | .44 |

Table A-3c shows field ratio variations if the current ratio is chosen to give B_ℓ/B_0 in the vicinity of 0.425, the value required to give double focusing with the 12 cm. lens. This variation is about 15%.

It is instructive to plot the positions of the two foci for our lens length and position, as a function of the field ratio B_ℓ/B_0 . This information is included in the program output shown in Table A-4, and is plotted in figure A-1. The position of the Y plane focus changes very little over the range of field ratios plotted, but the Z plane focus varies rapidly, going to infinity for $B_\ell/B_0 \approx 0.370$.

We notice from figure A-1 that double focusing occurs at $B_\ell/B_0 \approx 0.425$ as predicted above. The condition under which the experiments described in Chapter 5 were carried out, namely $B_\ell/B_0 = 0.48$, is also indicated on the graph. The Z plane focus was located at $\ell_2 = -19$ cms., or 17 cms. inside the magnet. Even the small 2.5% variation in B_ℓ/B_0 achieved by maintaining the current ratio constant at 0.75 results in the position of the Z plane focus moving over a 10 cm. range, and the Z plane magnification varying some 22%. This magnification is directly related to the effective solid angle of the system as described in Chapter 5, again indicating the importance of keeping the induction ratio constant.

To achieve double focusing with a 12 cm. lens operated at a field ratio of 0.48 would require the entrance of the lens, x_1 , to be located at about 14 cms. from the target, a condition rendered impossible by the physical size of the target chamber. Alternatively, Table A-2 shows that a lens of effective length 11 cms. would provide double focusing at

TABLE A-4

Spectrometer Focusing Conditions

| B_L/B_0 | L_2 Div | M Div | L_2 Con | M Con | Solid Angle |
|-----------|-----------|--------|------------|---------|-------------|
| 0.300 | 68.390 | -0.680 | -229.718 | -5.538 | 0.007841 |
| 0.325 | 69.254 | -0.661 | -290.250 | -6.069 | 0.007907 |
| 0.350 | 70.078 | -0.642 | -470.113 | -6.597 | 0.007956 |
| 0.375 | 70.866 | -0.624 | -25670.453 | -7.120 | 0.007991 |
| 0.400 | 71.620 | -0.606 | 265.028 | -7.639 | 0.008014 |
| 0.425 | 72.343 | -0.590 | 77.238 | -8.153 | 0.008025 |
| 0.450 | 73.036 | -0.574 | 15.238 | -8.662 | 0.008028 |
| 0.475 | 73.701 | -0.559 | -15.655 | -9.166 | 0.008023 |
| 0.500 | 74.340 | -0.545 | -34.158 | -9.665 | 0.008011 |
| 0.525 | 74.955 | -0.531 | -46.482 | -10.158 | 0.007993 |
| 0.550 | 75.546 | -0.517 | -55.280 | -10.646 | 0.007970 |
| 0.575 | 76.116 | -0.505 | -61.877 | -11.129 | 0.007943 |
| 0.600 | 76.665 | -0.493 | -67.008 | -11.606 | 0.007911 |
| 0.625 | 77.195 | -0.481 | -71.112 | -12.077 | 0.007876 |
| 0.650 | 77.706 | -0.469 | -74.472 | -12.543 | 0.007838 |
| 0.675 | 78.200 | -0.459 | -77.272 | -13.002 | 0.007798 |
| 0.700 | 78.678 | -0.448 | -79.643 | -13.456 | 0.007755 |
| 0.725 | 79.140 | -0.438 | -31.676 | -13.903 | 0.007710 |
| 0.750 | 79.587 | -0.428 | -83.439 | -14.345 | 0.007664 |
| 0.775 | 80.020 | -0.419 | -84.982 | -14.781 | 0.007616 |
| 0.800 | 80.440 | -0.410 | -86.346 | -15.210 | 0.007566 |
| 0.825 | 80.847 | -0.401 | -87.558 | -15.633 | 0.007516 |

SPECTROMETER FOCUSING

CONDITIONS

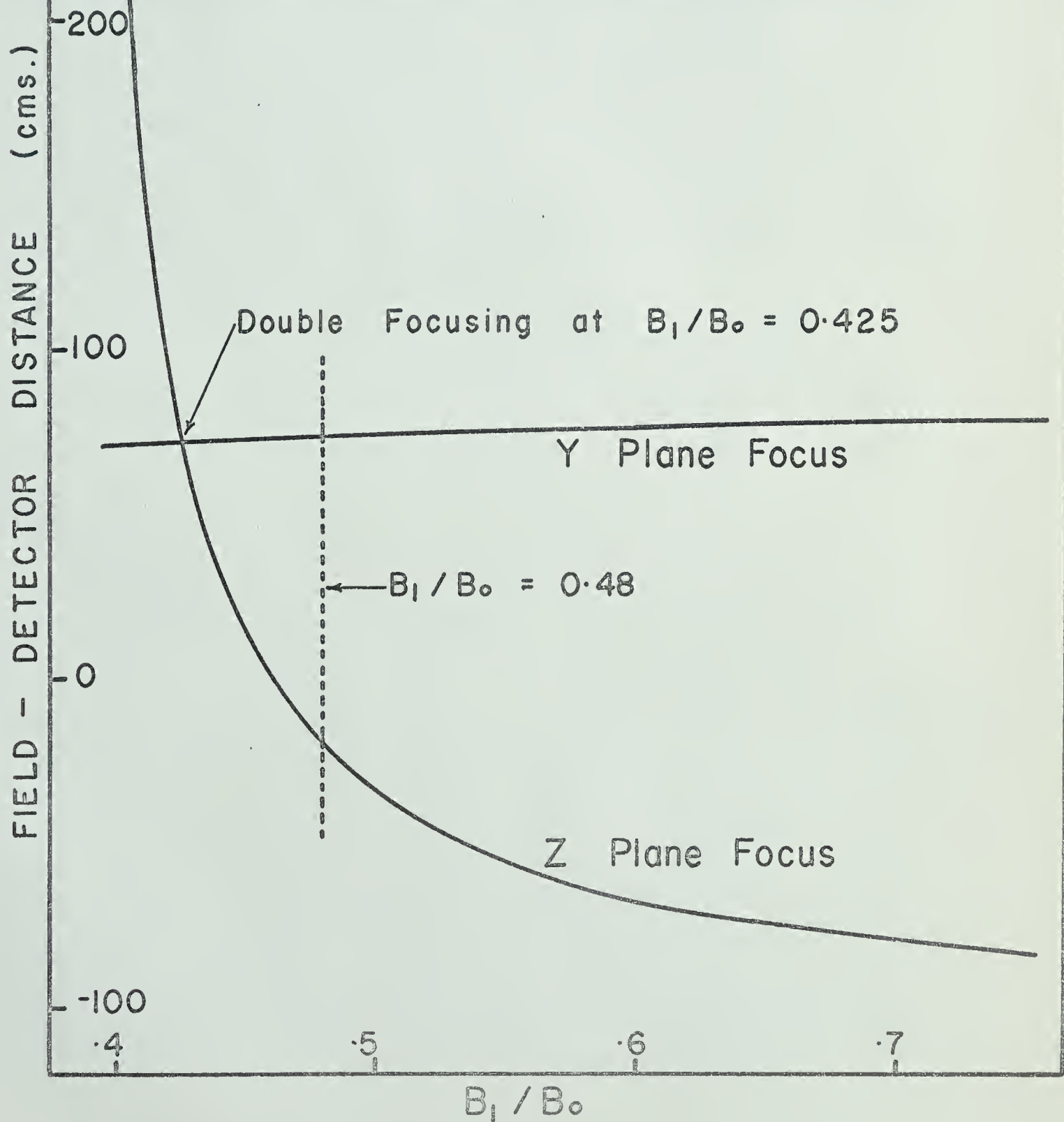


FIGURE A - 1

$B_\ell/B_0 = 0.48$ with existing geometry. The larger target chamber currently under construction would require a shorter lens yet.

To achieve double focusing with $B_\ell/B_0 = 0.65$ in the 12 cm. lens would require a target chamber about 1 cm. in diameter. This would seem to be impractical for use by experimenters with hands of a finite size.

APPENDIX B: THE TARGET CHAMBER

Somewhat in passing, it was mentioned in Chapter 4, Section (b) that, "due to vacuum difficulties," the system could only be operated over a range of about 30° on one side of the beam tube. It is worth discussing these difficulties briefly as they proved to be the main restriction on the work which could be attempted in the calibration process, and are currently preventing the use of the calibrated spectrometer for angular distribution studies.

Several factors undoubtedly contributed to the difficulties encountered with the sliding seal, a form of seal inherently difficult to design, the most satisfactory examples of which themselves leak occasionally.

A series of careful measurements on the target chamber revealed what was certainly the principal cause of vacuum problems. It was discovered that the chamber itself was not perfectly round, but considerably distorted, particularly in the vicinity of the beam entrance tube, which was welded into position. Thus the clamps intended to hold the strap onto the O-ring were unable to perform this function at all places. Moreover, these clamps were not positioned directly over the O-ring, and so caused the strap to warp if tightened too much. At any given position the clamps had to be carefully readjusted while monitoring the pressure in the chamber, slackening them in some places and tightening

them in others until the best vacuum was achieved. Naturally the flexibility of the strap could correct for small deviations from the round, but whenever such a deviation occurred at the rigid coupling to the quadrupole a leak was inevitable. It should be possible to eliminate these problems with a target chamber machined round, with no welds, and with clamps directly over the O-ring itself.

The need for a small target chamber to make double focusing practical with the present lens has been described elsewhere. The resulting small radius of the sliding seal, however, makes the sliding action more difficult, probably causing the stainless steel strap to bow off the O-ring when it is moved. This hypothesis is supported by the fact that the strap must be carefully pushed back onto the O-ring at each new position in order to achieve a seal. The phenomenon of the seal leaking while being moved and at new positions may also be attributed to the O-ring slipping in the groove beneath the seal. An attempt was made to correct this by following the commercial practice of glueing the O-ring into the groove, and lubricating the seal with a mixture of light pump oil and Molycote (powdered Molybdenum disulphide). No great improvement was observed with this or other lubricating mixtures which were tried. It is hoped that a larger chamber will relieve these problems, at the cost of difficulties in focusing.

All of the problems manifested themselves when the target chamber was bench tested. They were still worse with the chamber installed in the system, where any lack of concentricity or of proper alignment

enhanced them. The net result, then, was that a satisfactory vacuum could be achieved only over a range of about 30° on one side of the beam, and the experiments performed were confined to that region.

Moreover, it proved impossible to isolate the target chamber from the rest of the system by placing a valve between the chamber and the quadrupole lens. Even the thinnest available valve, one designed specifically for the purpose by Dr. W. C. Olsen of this laboratory, requires that the lens be moved at least 4 cms. further from the target. The discussion in Appendix A indicates that this makes double focusing a practical impossibility. Thus the entire system had to be let up to atmospheric pressure when changing targets, causing considerable time delay. The solution to this problem is to locate the valve between the quadrupole and the spectromagnet itself, which would require the existing coupling between these two to be completely redesigned.

Most of the possible improvements mentioned in this Appendix have been incorporated into the design of a new target chamber currently under construction. It is hoped that with the installation of this chamber, "vacuum difficulties" will cease to be the principal limitation on the applications of the spectrometer system.

APPENDIX C

Several possible explanations were advanced for the observed displacement between the gold and aluminum calibration curves described in Chapter 4, Section (c). These are discussed individually in the following paragraphs.

(i) The calculated kinematics were in error. The results of the kinematic program were checked for aluminum elastic scattering and other reactions against published data and found to be in complete agreement. Moreover, spot manual checks were made which agreed with the results given by the program. The input masses were carefully verified, and calculations show that even if the target were of the wrong isotope, resulting errors would be negligible.

(ii) The angle determination was in error. Kinematics for other angles reveal that such an error would have to be over 20° to account for the observed discrepancy.

(iii) The detector was not located on the 90° exit ray, so that when it was moved back 3 cms. to the approximate position of the aluminum focus, the angle of the rays would cause an apparent shift. This suggestion was eliminated for several reasons.

First the evidence as described in Chapters 4 and 5 indicates that the detector was indeed very close to the 90° exit ray. Furthermore, a simple calculation reveals that for this effect to explain the

observations, the deflection of the particles in the magnet would have to be 83° , for too great an error to be credible.

Secondly, the experiment was repeated without moving the detector to the aluminum focus. Although this makes the focus somewhat worse, the calibration was easily repeated, and the same difference between the aluminum and gold calibration curves was observed.

Thirdly, if the detector was not located on the 90° exit ray, then a far greater discrepancy in calibration curves would be expected when the calibration was repeated with the detector moved back nearly 10 cms. to the focus location with the quadrupole lens on. No such discrepancy was observed, and the calibration curves from gold scattering both with and without the quadrupole are in complete agreement.

Fourthly, the same discrepancy was observed when the detector was placed at different positions along the focal plane.

(iv) Because of the large aluminum image, and the fact that the high energy side (corresponding to a more forward scattering angle) will have a higher concentration of particles than the low energy side, an error is introduced in balancing the heights of the two side peaks. A simple calculation reveals that this effect can account for a maximum error of about 10 kilocycles, and is probably completely unobservable.

(v) Suitable target thickness corrections were not made. The same discrepancy was observed when one target, aluminum on gold, was used for both experiments, and in any case the targets were never more than 6 - 7 kilovolts thick.

We must conclude that no satisfactory explanation has been found for this discrepancy, although we can say that it appears to be a real kinematic effect of some nature. Further scattering observations on targets of smaller A may suggest some explanation.

APPENDIX D

Several incidental observations were made while performing the experiments described in Chapters 4 and 5, and some of these deserve to be noted, at least briefly and qualitatively, as a guide to parties interested in using the spectrograph-spectrometer system.

(i) Davies (Davies, 1966) has pointed out that with a 0.3" aperture in the energy defining slits, the momentum dispersion of the beam is approximately $\Delta p/p = 3.5 \times 10^{-3}$. These experiments were performed with a slit aperture of 0.25", corresponding to $\Delta p/p \approx 3.0 \times 10^{-3}$. Making use of the expression

$$D = p \frac{dx_3}{dp} = q \sin \alpha$$

from which

$$dx_3 = \frac{dp}{p} \circ q$$

for the 90° ray, this dispersion can be expected to make the image size about 2.1 mm in the spectrometer mode, and about 1.7 mm in the spectrograph mode. The effect of the accelerator momentum dispersion should be just visible in the spectrometer mode, and may account for the fact that even for the best spectrometer focus observed, about 5% of the counts fell into the neighbouring steps of the wedge, i.e. beyond the 2 mm. focusing step. The beam dispersion seen by the target, however,

may be somewhat less than the accelerator dispersion due to the combined effect of the switching magnet and the fine collimation at the target chamber. The collimation selected only a small fraction of the large beam image observed at the first collimating disc.

(ii) Small changes in the position of the image were often observed when changes were made in the accelerator source parameters. This could be explained by the fact that changes in the fields of different elements of the Einzel lens might cause a well-focused beam to enter the analysing magnet at somewhat different angles (within the restriction imposed by slits located a distance $2R$ before the center of the analysing magnet). This would cause the energy defining slits to accept a slightly different energy range. The changes observed were of the order of 2 - 3 kilocycles, which is approximately the observed reproducibility of the energy (frequency) measurements.

A more pronounced effect was the changes in the quality of the focus at different source parameter settings. This may be attributable to the fact that the beam momentum dispersion will be increased if a poorly focused beam is entering the analysing magnet.

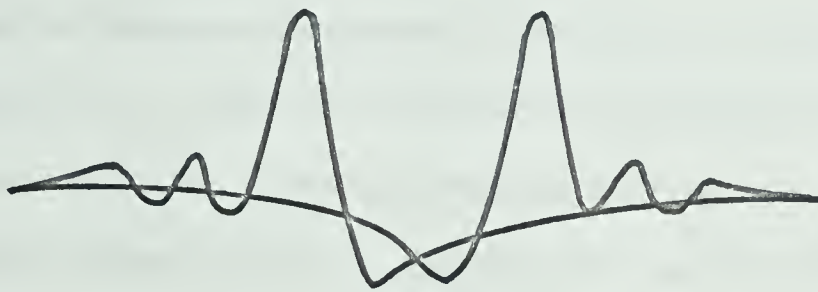
(iii) Both the analysing magnet and the spectromagnet were recycled each time the spectrometer was used. That is, the current in the magnets was raised to a fixed maximum value, then returned to zero, and then raised again to the desired setting. In operation, the magnet currents were always raised. If it became necessary to operate them at a lower value, they were recycled and raised to the value required. Two important effects were observed when this precaution was not taken.

Firstly, there was a change in the image position. This is illustrated in the following table, compiled from observations of the scattering of 3 MeV protons from a gold target, all other parameters remaining constant.

| Operation | Frequency Mc/s |
|----------------------------------------------------------------------------------|----------------|
| Magnet Recycled | 20.408 |
| Magnet Recycled | 20.409 |
| Magnet Recycled | 20.409 |
| Magnet current lowered to zero, then raised without recycling. Repeated 3 times. | 20.413 |
| | 20.413 |
| | 20.413 |
| Magnet Recycled | 20.408 |
| Magnet Recycled | 20.408 |

Once again the effect is of the order of a few kilocycles, but in this case seems to be observably greater than the reproducibility of the measurements. An effect of about the same magnitude was observed when the same test was carried out on the analysing magnet.

The more important observation pertaining to recycling, was the loss of field homogeneity when the magnet was not recycled. This was observed in two ways. Normally, the nuclear magnetic resonance signal displayed on the oscilloscope shows a distinct "ringing" as well as the main resonance dip (Figure D-1a). The amount of this ringing depends



NMR RESONANCE - HOMOGENOUS
FIELD

(a)



NMR RESONANCE - NONHOMOGENOUS
FIELD

(b)

FIGURE D - 1

upon the field homogeneity in the vicinity of the probe. When the magnet current is raised to a high value, and then brought back to its original value without recycling, the ringing disappears, indicating a deterioration in the field homogeneity (Figure D-1b).

The loss of homogeneity caused by failing to recycle the magnet is also reflected in the spectra illustrated in figure D-2a,b. First, a good focus was obtained. Then the magnet current was raised and lowered to the original value without recycling, and spectrum D-2a was observed. 68% of the counts are in the third step. Then the magnet was recycled, and spectrum D-2b observed. Now 78% of the counts are in the third step.

These results suggest that differential hysteresis may be observed in the magnet, and that it would be good practice to recycle the magnets before each use.

(iv) One final observation is worth recording, namely the effect of large fields in the spectromagnet on the current recorded in the target chamber by the current integrator. In figure D-3, the time for a fixed integrated current to be recorded has been plotted against the current in the main magnet, both with and without electron suppression before the Faraday cup. At high fields, the integrator sees far less current. The hypothesis that this is due to the effect of the field on secondary electrons appears to be verified by the fact that the effect is considerably less pronounced when 1000 volts are placed on the electron suppressor, and the basic current is also lower.

The effect of the field only becomes observable for fields considerably higher than were used in the experiments described in this thesis.

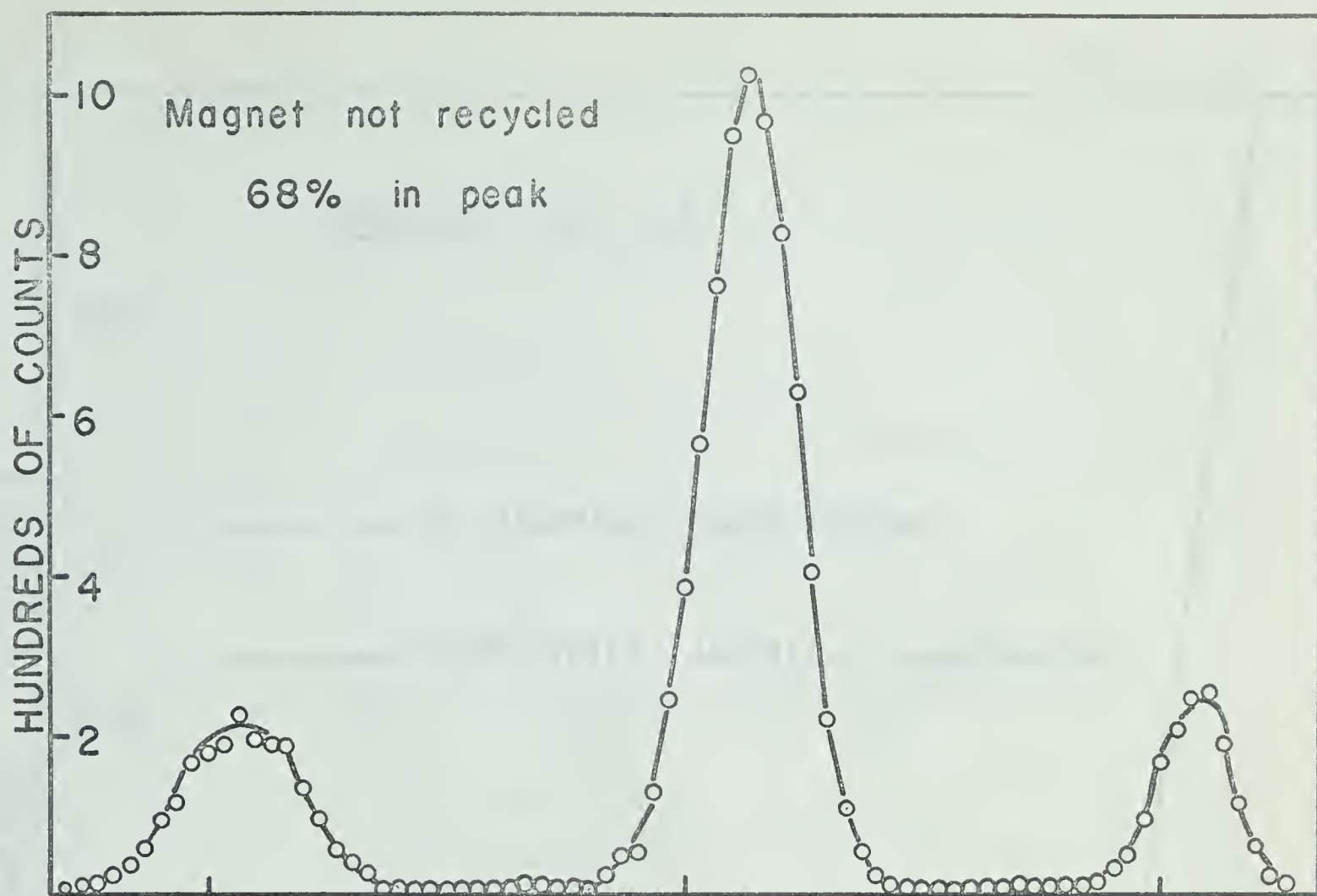


FIGURE D - 2 a

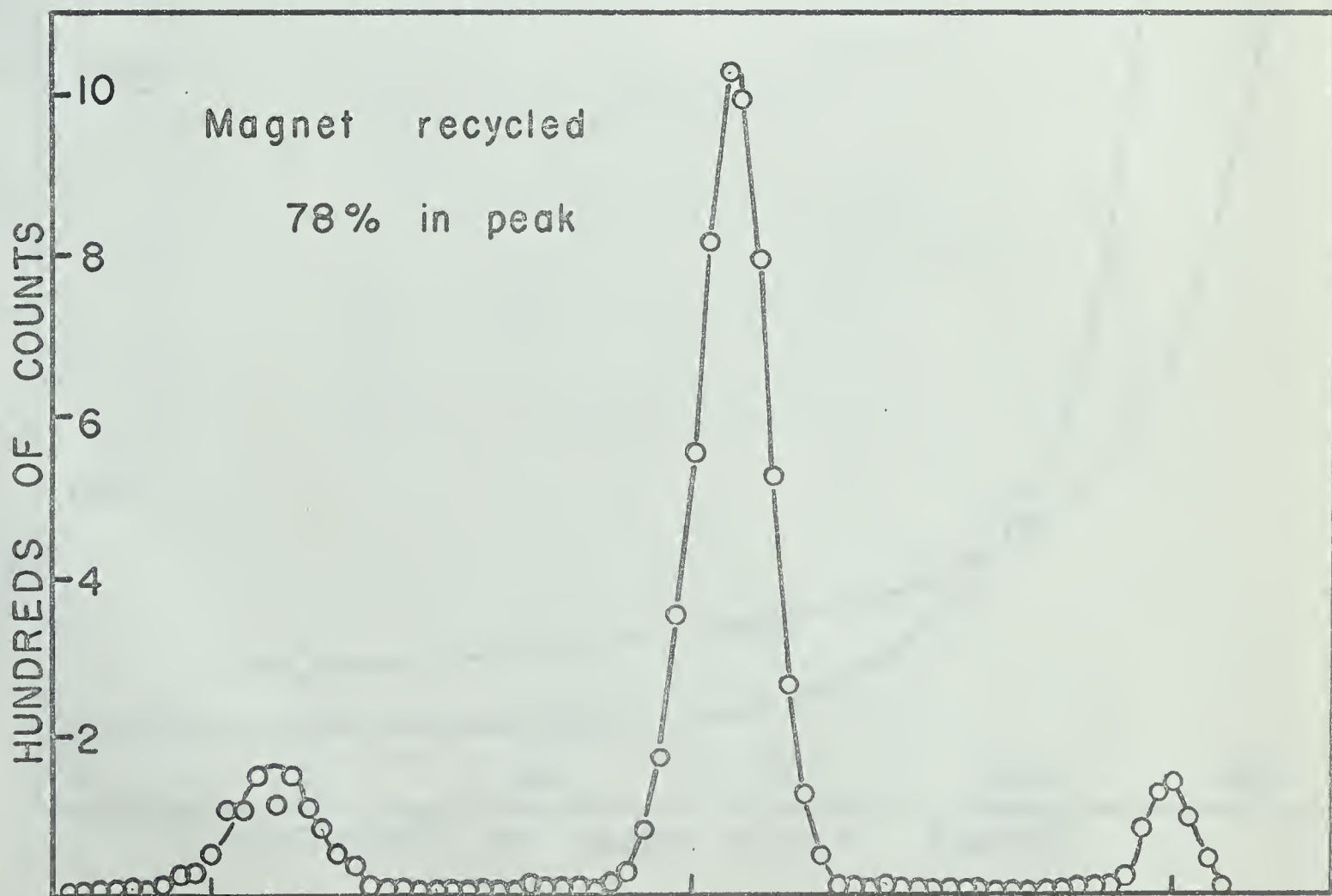
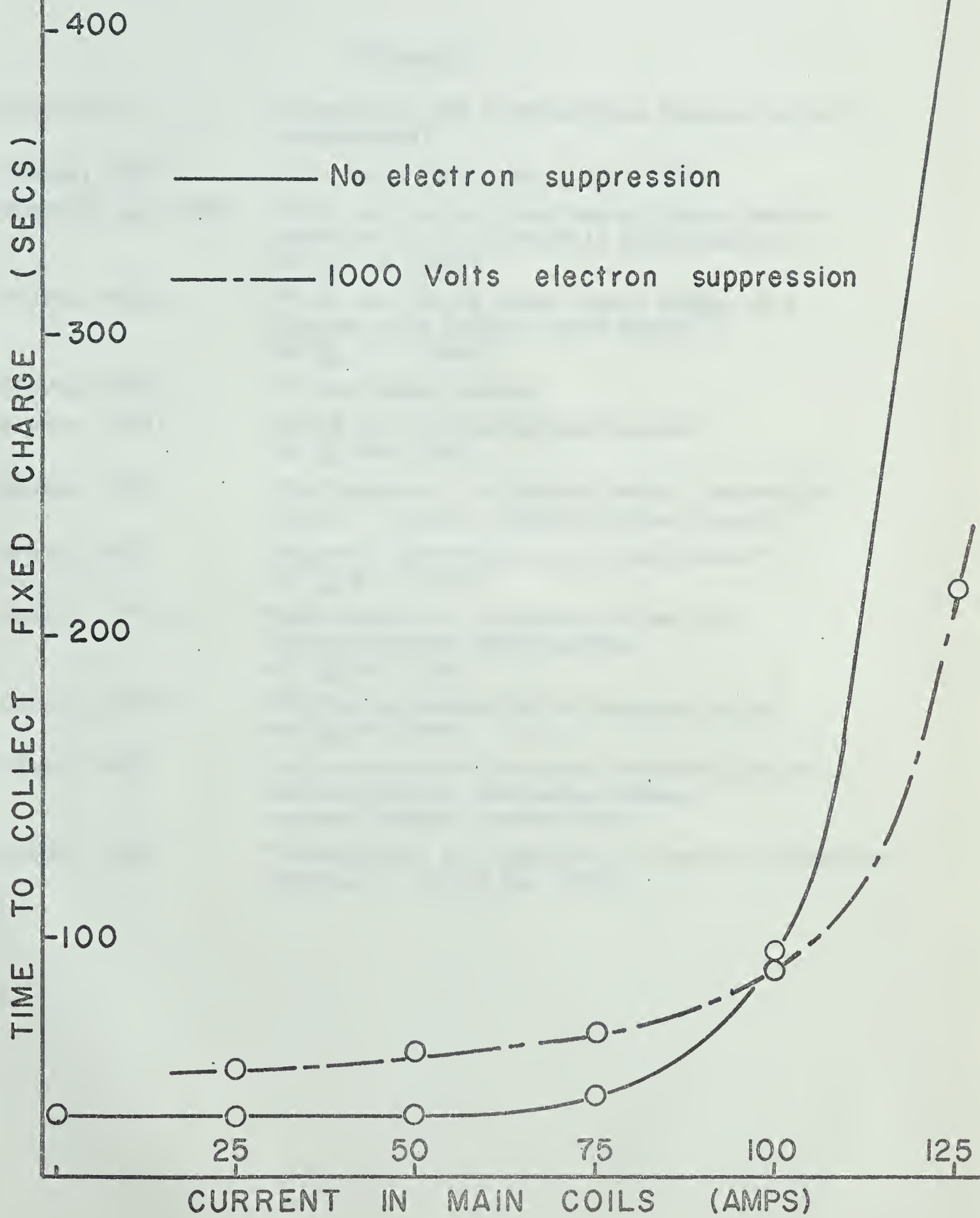


FIGURE D - 2 b

FIGURE D - 3



REFERENCES

- (Alexander) "Electronics for a Solid State Detector Array"
(unpublished)
- (Barber, 1933) Proc. Leeds Phil. Soc. 2 427 (1933)
- (Brown et al, 1964) "First and Second Order Magnet Optics Matrix
Equations for Uniform Field Wedge Magnets."
RSI 35 481 (1964)
- (Brown, 1965a) "First and Second Order Magnet Optics of a
Circular Pole Uniform Field Magnet I"
RSI 36 271 (1965)
- (Brown, 1965b) Private Communication
- (Browne, 1956) "Broad Range Magnetic Spectrograph"
RSI 27 899 (1956)
- (Davies, 1966) "The University of Alberta Mobley Compression
System." Nuclear Research Center Report
- (Enge, 1958) "Magnetic Spectrograph and Spectrometer"
RSI 29 885 (1958)
- (Haddock, 1963) "Application of the Matrix Method to a
Browne-Buechner Spectrograph."
RSI 34 745 (1963)
- (Halbach, 1964) "Matrix Representation of Gaussian Optics"
AJP 32 90 (1964)
- (Olsen, 1962) "A Transistorized Frequency Modulated Proton
Nuclear Magnetic Resonance System."
Nuclear Research Center Report
- (Penner, 1961) "Calculations of Properties of Magnetic Deflection
Systems." RSI 32 150 (1961)

B29845